Università di Pisa

DIPARTIMENTO DI FISICA
Corso di Laurea Magistrale in Fisica

Tesi di laurea

Observation of a rotonic 'stripe phase' in a dipolar Bose-Einstein condensate

Relatori:
Dr. Andrea Fioretti

Candidato:
Francesca Famà
Matricola 507594

Prof. Giovanni Modugno

Internal: Prof. Francesco Fuso

Anno Accademico 2017-2018

Contents

Introduction

The study of new states of matter is one of the most amazing and challenging subjects of physics. Solids, liquids, gases and plasmas are well established entities in our every day life, but since the early 900s also new states with new properties are taking part in our studies and technologies [1,2].

Back to the 1924, the Indian physicist Satyendranath Bose committed an 'error' during a statistical physics lesson. From this error and the collaboration between S. Bose and Albert Einstein the Bose-Einstein quantum statistics was born. Such statistics predicts the existence of a new quantum state of matter at low temperature: the Bose-Einstein condensate (BEC) [3]. Theoretical investigations and experimental realizations of Bose-Einstein condensates are the objectives of the research field of quantum gases.

The peculiarity of a Bose-Einstein condensate is to be a macroscopic system governed by quantum laws. It is a coherent superposition of particles in the same quantum state [4]. In order to reach the first order transition to a condensate an ultra cold, dilute system is necessary. Because of these requirements, it took quite a long time before such a new state of matter was experimentally realized. However with new improvements in laser cooling, trapping techniques and evaporative cooling first alkali BECs were achieved back to the 1995, seventy years later than the theoretical predictions. First condensates were realized with ^{87}Rb atoms, by the group of Eric Cornell and Carl Wiemann at JILA (Boulder, Colorado) [5], and with ^{23}Na atoms, by the group of Wolfgang Ketterle at MIT (Cambridge, Massachusetts) [6]. These works were awarded with the Nobel prize in 2001. Although BECs are very dilute systems their properties were found to be dominated by the interactions between particles. Since BEC exists in an ultracold and dilute regime the most relevant interactions are the isotropic, elastic two-body collisions. Such interactions do not require the exact knowledge of the real inter atomic potential, since they can be modelled as an effective contact force. Such contact force is then characterized by an effective coupling constant a_s, the s-wave scattering length [7].

A very important and interesting property of BEC systems, is the appealing possibility to control and modify their characteristics. First of all contact interactions are highly tunable via the so-called Feshbach resonances [8]. These resonances are controlled by an external magnetic field and allow to have BEC with repulsive, attractive or even null interactions. In second place a BEC of ultra cold atoms is still in the gas phase and therefore needs to be confined by an external trapping potential. This requirement allows to control temperature and density of the system as well as its geometry.

Another remarkable property of condensed systems is that they can show superfluid properties. Superfluidity was first observed in liquid Helium in 1908 by Heike Kamerlingh Onnes [1]. The name 'superfluid' was given to these new quantum state as the liquid He was seen to flow in a thin capillary without viscosity [9]. The absence of viscosity is not the only peculiar feature of such superfluid phase. If a rotation is impressed onto the system, it develops vortices. The development of vortices is thus considered a clear signature of superfluid properties. The Bose-Einstein condensate was observed to exhibit quantum vortices, it thus has a superfluid behaviour [10].

The flexibility of the system and its superfluid properties make the BEC an excellent quantum simulator. Very complex Hamiltonians have been engineered and many-body problems studied. Furthermore superfluid theory can be tested. An example of the goals achieved is the study of the superfluid to Mott insulator transition [11], as well as the studies on spin-orbit coupled systems.

The latter type of system, in particular, was used to achieve a quantum state with supersolid properties [12], i.e. combining superfluid properties with the long range spatial periodicity of a solid.

After the pioneering works of Ketterle and Cornell, and Wieman many experiments have been done exploring the multitude of possibilities offered. Other alkali atoms were condensed, such as Lithium [13] and Potassium [14], as well as other atomic species, such as spin-polarized Hydrogen [15], Chromium [16] and Ytterbium [17]. The realization of such a vast range of BECs has opened an avenue to the study of lots of physical phenomena. For example synthetic dimensions were realized with condensates of Yb atoms [18].

The condensate of Chromium atoms is the first example of a BEC system interacting not only via the contact interaction, but experiencing also a different non negligible inter-particle force. It is the magnetic dipole-dipole interaction (DDI) and is non negligible because of the permanent magnetic moment $\mu = 6\mu_B$ of Chromium atoms. The peculiarity of the DDI is its long-range, anisotropic nature, in contrast with the short-range, isotropic character of the contact interaction [19]. Such characteristics not only translate in an anisotropy of the speed of sound, observed in Cr [20], but also modify the stability of the system; in fact, by tuning the scattering length the Cr BEC was observed to produce a d-symmetric collapse [21].

This wealth of new phenomena related to the DDI has motivated a quest for the condensation of even more dipolar elements. Er ($\mu \sim 7\mu_B$) [22] and Dy ($\mu \sim 10\mu_B$) [23] were successfully condensed. Dipolar systems are characterized by a competition between the repulsive van der Waals forces and the partially attractive DDI [24]. The interplay between interactions and a confining potential leads to a rotonic minimum at a finite momenta in the excitation spectrum, similar to that of liquid He [25]. The onset of a rotonic instability has been observed for the first time in a dipolar BEC of Er atoms [26]. Although the periodic density modulation associated to the roton instability is interesting in view of realizing a dipolar supersolid, it it not clear whether the instability leads to a stable phase or simply to a collapse.

Recently a stabilizing short-range repulsion term has been discovered in quantum gases. It is due to the zero-point energy of quantum fluctuations and in dipolar systems is given by the Pelster and Lima term [27]. This term is relevant in systems with competing interactions. In fact if a weakly attractive regime is realized it can stabilize the system and prevent a collapse. In strong dipolar system, such as Er and Dy, it is also connected to the appearance of a self-bound quantum state, called 'droplet', with liquid properties [28]. These droplets are almost an order of magnitude denser than a standard condensate, and can exist in free space [29]. When trapped, they arrange in one or two dimensional array, with roughly regular spacing, but they lack the necessary coherence to establish a supersolid phase [30, 31].

Although both the roton spectrum and the droplets are due to an interplay of the same contact and dipolar interactions, they appeared, so far, as two apparently disconnected phenomena. With my thesis work I have contributed to an experiment aiming and finding a connection between these two phenomena. The experiment is based on a BEC of Dysprosium atoms, which have the strongest dipole moment among the atomic elements, and therefore the strongest dipolar effects.

The main result of the experiment is the observation of a stable 'stripe phase' induced by a rotonic instability. Like quantum droplets, this phase is stabilized by quantum fluctuations. This new phase is however different from the droplets as it is not self bound and features a much larger coherence than the droplets. These properties are verified by studying both regimes. Indeed we find that both of them can be reached by tuning the interaction strength.

I did my thesis work in the Dysprosium laboratory in the Pisa Section of CNR-Istituto Nazionale di Ottica. This laboratory runs an experiment devoted to the Bose-Einstein condensation of ^{162}Dy, performed in partner ship with LENS in Florence. The experimental apparatus has been completed in 2017 and first signature of condensation were achieved in December 2017. The system has been characterized, in particular by a study on its Feshbach resonances. My work starts from here on.

The thesis is organized as follows:

- Chapter 1 is devoted to a theoretical overview of the studied phenomena, with a final part on related experiments. I present a description of the Bose-Einstein condensate and its interactions within a mean-field theory and beyond. Two-body contact interactions are described and three body processes are briefly introduced. The next section discusses DDI and the appearance of a roton mode in the excitation spectrum. Then I report on the instabilities of a dipolar system and related experiments. Final sections deal with the beyond mean field correction to the mean field theory and quantum droplets. One section describes the quantum fluctuations correction term, while the other the effect of such a term in strong dipolar systems: quantum droplets.

- In Chapter 2 I briefly review atom optics tools necessary to achieve condensation. Scattering and dipole forces are recalled in order to explain the basic idea of the Magneto Optical Trap and of the Optical Dipole Trap. After a theoretical introduction I briefly described the experimental setup. In the end I present an analysis which demonstrates the occurrence of the BEC transition.

- In Chapter 3 the characterization of the system is presented. Trap measurements as well as magnetic field calibration and Feshbach resonances are reported. In the final section I present measurements of the recombination constant K_3.

- Chapter 4 focuses on the observation and investigation of a new modulated phase in an unstable regime. Here I report first images of such a phase, describe models I used for the analysis and finally present results. An additional section is devoted to the analysis of the reversibility of the BEC-modulated phase transition.

  Finally, I give some conclusive remarks and an outlook on future experiments.

  The results presented in this Thesis have been the object of an article, Ref. [32], submitted to Phys. Rev. Lett. in November 2018.

Chapter 1

Theory of dipolar Bose-Einstein condensates

This chapter gives a brief theoretical description of Bose Einstein condensates (BEC). The starting point are quantum statistics considerations as they allow to understand why a Bose Einstein condensate is defined as a macroscopic system with a quantum behaviour. Real BECs are then considered, introducing the effects of a trapping potential and interactions between atoms. The external trapping potential takes into account three important features: non uniformity, finite size and finite temperature. However, the biggest discrepancy from the ideal case is given by the presence of interactions. In the following two-body interactions are mainly considered: an isotropic short-range contact interaction and a long-range anisotropic dipole-dipole interaction (DDI). A tool to tune the contact interaction is presented: Feshbach resonances. Three body recombinations are mentioned. DDI features are reported, in particular the existence of a local minimum in the dispersion curve, called roton, and instability regimes. In the end beyond mean field effects are included. The theory used is mainly taken from textbooks [4, 7] and recent papers [19, 25, 33].

1.1 A consequence of quantum statistics

The quantum statistics of bosons is described by the Bose-Einstein distribution, which controls how bosons occupy the energy levels of a system:

$$f(E) = \frac{1}{e^{\beta(E-\mu)} - 1} \tag{1.1}$$

where $\beta = (k_{\mathrm{B}}T)^{-1}$ and $k_{\mathrm{B}} = 1.38 \times 10^{-23}$ JK^{-1} is the Boltzmann constant, μ is the chemical potential, E is the energy of the state under consideration, and $f(E)$ the occupation number. Using a grancanonical formalism the number of atoms for a bosons system is given by

$$N = \frac{gV}{\lambda_{\mathrm{T}}^3} G_{\frac{3}{2}}(z) \tag{1.2}$$

where V is the volume of the sample, $g = 2s + 1$ is the spin degeneracy, $\lambda_{\mathrm{T}} = \sqrt{2\pi\hbar^2/mk_{\mathrm{B}}T}$ is the De Broglie thermal wavelength and $z = e^{\mu/k_{\mathrm{B}}T}$ is the fugacity of the system. Quantum effects are important in the limit $z \to 1$, where $G_{\frac{3}{2}}(1) \sim 1.3$[1]. In this limit a saturation of the

[1] The function $G_{\frac{3}{2}}(z)$ is defined as

$$G_{\frac{3}{2}}(z) = \frac{2}{\sqrt{\pi}} \int_0^\infty dy \frac{y^{\frac{1}{2}}}{z^{-1}e^y - 1} \tag{1.3}$$

number of particles is observed. Physically it is like a saturation number for the bosons at thermal equilibrium.

If other particles are included they automatically occupy the energetic minimum available, i.e. the ground state. This phenomenon is known as Bose-Einstein condensation[2]. Typically it can be seen as a function of temperature. Keeping V and N fixed, the temperature is decreased. When a critical value is reached the system undergoes a first order phase transition characterized by a macroscopic occupancy of the ground state[3]. The system obtained is extremely coherent as most of the particles are in the same quantum state, and it is said to be a macroscopic system with a quantum behaviour. Isolating the ground state contribution it results:

$$N = \sum_{\mathrm{i}} \frac{1}{e^{\beta(E_{\mathrm{i}}-\mu)}-1} = N_0 + N_{\mathrm{T}} \tag{1.4}$$

where N_0 is the number of bosons in the ground state and N_{T} the number of bosons in the excited states. A condensate is then composed mainly of a condensed part (N_0), but it has also a *thermal depletion* ($N_{\mathrm{T}} = N - N_0$), i.e. a thermal component. For the sake of completeness we report also of the existence of a third component, a *quantum depletion*, due to the correlation between atoms at short distances. However for the theory treated in this section it is negligible.

1.2 Trapping potential

The experimentally created Bose Einstein condensate deviates from the ideal case because of three reasons:

- It is confined by a (usually harmonic) potential V_{ext} characterized by a frequency ω_{ho} and a characteristic length $a_{\mathrm{ho}} = \left(\frac{\hbar}{m\omega_{\mathrm{ho}}}\right)^{\frac{1}{2}}$. It is then non-uniform.
- It has a finite size, so a finite number of atoms N in a finite volume V.
- It has a finite temperature T.

Non-uniformity

A non interacting condensate in an harmonic trap is initially discussed to account for non-uniformity effects. The harmonic potential representing the trap can be written as:

$$V_{\mathrm{ext}} = \frac{m}{2}(\omega_{\mathrm{x}}^2 x^2 + \omega_{\mathrm{y}}^2 y^2 + \omega_{\mathrm{z}}^2 z^2) \tag{1.5}$$

The fundamental eigenstate and eigenvalue of the single particle Hamiltonian are:

$$H = \frac{\hbar^2 q^2}{2m} + V_{\mathrm{ext}} \tag{1.6}$$

$$\varphi_0 = \left(\frac{m\omega_{\mathrm{ho}}}{\pi\hbar}\right)^{\frac{3}{4}} e^{-\frac{m}{2\hbar}(\omega_{\mathrm{x}}x^2+\omega_{\mathrm{y}}y^2+\omega_{\mathrm{z}}z^2)} \tag{1.7}$$

$$E_0 = \frac{1}{2}\hbar(\omega_{\mathrm{x}} + \omega_{\mathrm{y}} + \omega_{\mathrm{z}}) = \frac{3}{2}\hbar\overline{\omega} \tag{1.8}$$

where $\omega_{\mathrm{ho}}^3 = \omega_{\mathrm{x}}\omega_{\mathrm{y}}\omega_{\mathrm{z}}$ and $\overline{\omega} = \frac{1}{3}(\omega_{\mathrm{x}} + \omega_{\mathrm{y}} + \omega_{\mathrm{z}})$. The separation between levels fixes an oscillation

where $y = \epsilon/k_{\mathrm{B}}T$. Such a function is proportional to the derivative of the grancanonical potential of a system of non relativistic bosons.

[2]The Bose-Einstein statistics is named after physicists A.Einstein and S.Bose. During one of his lectures S.Bose states for the first time that the Maxwell-Boltzmann distribution is not correct for microscopic systems. The reason, according to the Indian physicist, has to be attributed to fluctuations due to the Heisenberg's uncertainty principle. He wrote a letter to Einstein for an opinion. In 1924 the first article on the Bose-Einstein condensation was published.

[3]The macroscopic occupancy of a single state is possible thanks to the nature of bosons. Fermions, on the contrary, do not have such possibility. The condensation is thus a bosonic systems peculiarity. Fermion systems have a corresponding phenomenon called 'quantum degeneracy'.

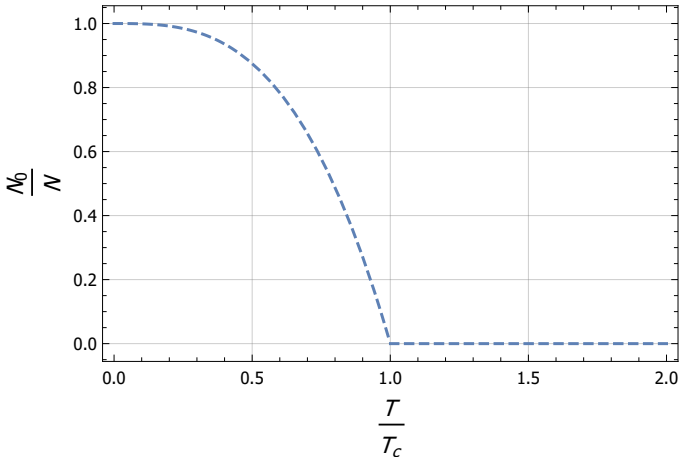

Figure 1.1: Condensate fraction as a function of $\frac{T}{T_c}$ for an ideal Bose gas in an harmonic trap.

temperature:

$$T_0 = \frac{\hbar\overline{\omega}}{k_{\mathrm{B}}} \tag{1.9}$$

The thermal component in an harmonic trap is now evaluated using the expression in Eq. 1.4, where in this case $E_{\mathrm{i}} = (\omega_{\mathrm{x}} n_{\mathrm{i}}^x + \omega_{\mathrm{y}} n_{\mathrm{i}}^y + \omega_{\mathrm{z}} n_{\mathrm{i}}^z)$. In order to do so, the semi-classical approximation is introduced. Such approximation consists in treating the excitations as a continuum, corresponding to a regime of temperature $T \gg T_0$. This is a microscopic condition that must not be confused with the macroscopic $T > T_c$ claim. Experimentally $T_0 \ll T \ll T_c$ is a well defined regime called of *finite temperature*. In this regime the N_{T} component is not null. In the semiclassical approximation the sum in Eq. 1.4 can thus be converted into an integral:

$$\sum \longrightarrow \frac{V}{(2\pi\hbar)^3} \int d^3n \tag{1.10}$$

The thermal component results:

$$N_{\mathrm{T}} = \frac{(k_{\mathrm{B}}T)^3 \zeta(3)}{\hbar^3 \omega_{\mathrm{ho}}^3} \tag{1.11}$$

where $\zeta(s)$ is the Riemann function [34] and $\zeta(3) = 1.202$. Since the condition for the occurrence of BEC is the inequality $N_{\mathrm{T}} \leq N$, the critical temperature T_c is defined by the condition $N_{\mathrm{T}}(\mu \to \epsilon_0) \sim N$, hence

$$T_c = \frac{\hbar\omega_{\mathrm{ho}}}{k_{\mathrm{B}}} \left(\frac{N}{\zeta(3)}\right)^{\frac{1}{3}} \sim 0.94 \frac{\hbar\omega_{\mathrm{ho}}}{k_{\mathrm{B}}} N^{\frac{1}{3}} \qquad . \tag{1.12}$$

The thermal component in Eq. 1.11, can thus be written as $N_{\mathrm{T}} = N\left(\frac{T}{T_c}\right)^3$ and the condensate fraction results

$$\frac{N_0}{N} = 1 - \left(\frac{T}{T_c}\right)^3 \qquad . \tag{1.13}$$

The condensed fraction as a function of $\frac{T}{T_c}$ is shown in Fig. 1.1.

So far, the condensed and thermal fraction have been derived as a function of T_{c} in a semi classical approximation for a non-uniform sample. What are then the differences from a uniform case? To highlight the effects of non-uniformity, N_{T} is written using the density of states $g(E)$ in

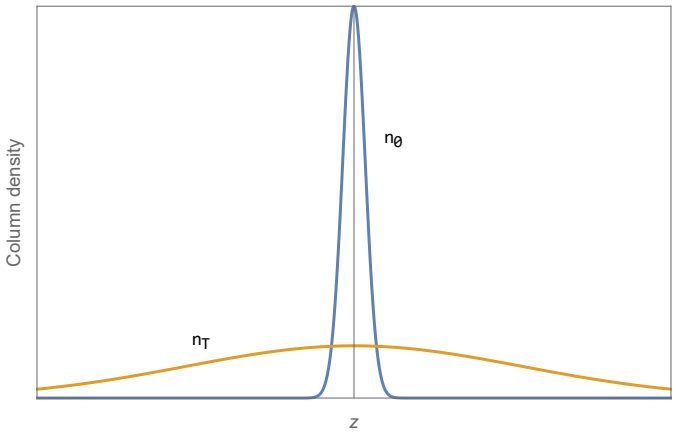

Figure 1.2: Column density for non interacting bosons in a spherical trap. The central peak with density n_0 is the condensed fraction superimposed onto a broader thermal density n_T.

the semi classical approximation:

$$N_{\mathrm{T}} = \int_0^\infty g(E)n(E)dE \tag{1.14}$$

$$g(E) = \int \frac{d^3rd^3q}{(2\pi\hbar)^3}\delta(E - H(q)) \tag{1.15}$$

It follows

- for a uniform gas $H(q) = \frac{\hbar^2q^2}{2m} \rightarrow g(E) \sim E^{\frac{1}{2}} \rightarrow \frac{N_0}{N} \sim 1 - \left(\frac{T}{T_c}\right)^{\frac{3}{2}}$
- for a gas in a harmonic trap $H(q) = \frac{\hbar^2q^2}{2m} + V_{\mathrm{ext}} \rightarrow g(E) \sim E \rightarrow \frac{N_0}{N} \sim 1 - \left(\frac{T}{T_c}\right)^3$

The characteristic trend of the condensed fraction as a function of $\frac{T}{T_c}$ is then modified by the trap.

The non-uniformity of the sample also affects the system dimension D for which the condensation can be achieved. In particular while a 2D uniform sample cannot be Bose condensed, a non uniform one can. It formally follows from the fact that:

- for a uniform gas $g(E) \sim E^{\frac{D}{2}-1}$. If $D = 2$, $g(E)$ is a constant, N_{T} has therefore a logarithmic divergence.
- for a trapped gas $g(E) \sim E^{D-1}$. If $D = 2$, $g(E) \sim E$, condensation can then be achieved.

Experimentally an asymmetric trap such that $\hbar\omega_{2D} \ll k_{\mathrm{B}}T_{2D} < \hbar\omega_{\mathrm{z}}$ is used to create a 2D system. The critical temperature is then $T_{\mathrm{c}}^{2\mathrm{D}} = \frac{\hbar\omega_{2D}}{k_{\mathrm{B}}}\left(\frac{N}{\zeta(2)}\right)^{\frac{1}{2}}$ where $\omega_{2D} = (\omega_{\mathrm{x}}\omega_{\mathrm{y}})^{\frac{1}{2}}$. It is worth noting that in general it is not true that $T_{\mathrm{c}}^{2\mathrm{D}} < T_{\mathrm{c}}^{3\mathrm{D}}$ and $\hbar\omega_{\mathrm{z}} < k_{\mathrm{B}}T_{\mathrm{c}}^{2\mathrm{D}}$. Otherwise two condensations step would take place, but this is not what is experimentally observed.

Another important consequence of the non-uniformity is that the condensate signatures are not only in momentum space, but also in real space. Density matrices in real space and in momentum space are related by a Fourier transform. Single particle eigenfunctions of a uniform gas in the thermodynamic limit are plane waves $\varphi_{\mathrm{i}} = \frac{1}{V}e^{i(\vec{q}_{\mathrm{i}}\cdot\vec{r})}$, with $\hbar\vec{q}$ the momentum. Therefore, while in real coordinates space the distribution is given by a combinations of plane waves, in momentum space it is a Dirac δ function (Fourier transform of a plane wave). A non-uniform gas on the other hand, has a gaussian single particle eigenfunction φ_0. Since the transformation

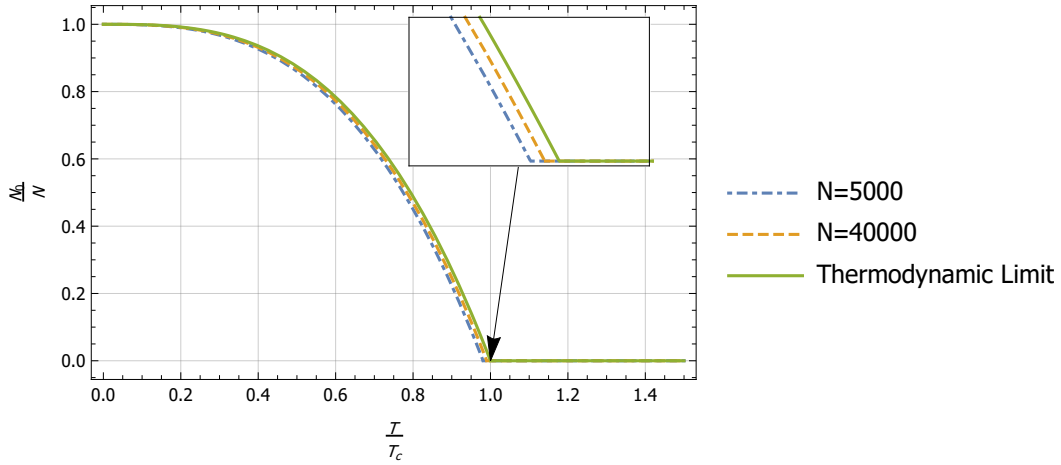

Figure 1.3: Condensate fraction as a function of $\frac{T}{T_c}$ for an ideal Bose gas in an harmonic trap with finite size correction. The blue dashed line represent the curve for $N = 5000$, the dashed brown $N = 40000$ while the green line the thermodynamic limit. Typical numbers for Dy condensed atom number in our experiment are $1 - 50 \times 10^3$.

of a gaussian is still a gaussian ($\tilde{\varphi_0}$ in the momentum space), the two distributions in real and momentum space at $T \leq T_c$ have the same form.

By using the diagonal terms of the one body density matrix[4] $n^{(1)}$, the column density distribution $n(z) = \int n(x, 0, z)dx$ can be obtained for both thermal and condensed fraction, see Fig. 1.2. It results

$$n_0(r) = N_0|\varphi_0(r)|^2 \tag{1.16}$$

$$n_{\rm th}(r) = \lim_{\mu \to \epsilon_0} \int \frac{d^3q}{(2\pi\hbar)^3} \frac{1}{e^{\beta(\epsilon(r,q)-\mu)} - 1} = \frac{1}{\lambda_T^3} g_{\frac{3}{2}} e^{-\beta V_{\rm ext}} \tag{1.17}$$

where $g_{\frac{3}{2}}$ is the Bose function [35]. We note that these two components have different spatial distributions, as can be inferred from the comparison between the two average square radii along the k direction

$$< r_k^2 >_{th} = \int \frac{n_{th}(k)k^2dk}{n_{th}(k)dk} \sim \frac{\zeta(4)}{\zeta(3)} \frac{k_{\rm B}T}{m\omega_k^2} \tag{1.18}$$

$$< r_k^2 >_0 = \int \frac{n_0(k)k^2dk}{n_0(k)dk} \sim \frac{\hbar}{2m\omega_k} \tag{1.19}$$

$$\frac{< r_k^2 >_{th}}{< r_k^2 >_{(0)}} \sim \frac{2k_{\rm B}T}{\hbar\omega_k} \gg 1 \qquad . \tag{1.20}$$

An experimental signature of the condensation is then the appearance of such two spatially separated components visible not only in the momentum space, but also in the coordinates one.

To summarize, for an harmonic trap:

- $\frac{N_0}{N} = 1 - \left(\frac{T}{T_c}\right)^3$ where $T_c = \frac{\hbar\omega_{\rm ho}}{k_{\rm B}} \left(\frac{N}{\zeta(3)}\right)^{\frac{1}{3}}$.
- Condensation is also possible in a 2D configuration.
- Condensation is expected in both momentum and real space.

[4]The one-body density matrix of a system is $n^{(1)} = \left\langle \hat{\psi}^\dagger(r)\hat{\psi}(r') \right\rangle$ where $\hat{\psi}^\dagger(r)$ and $\hat{\psi}(r')$ are the creation and annihilation operator of a particle in r and r'. Diagonal terms are related to the density of the system [7].

Finite size effects

The main consequence is that the finite size does not allow to reach a perfect thermodynamic limit. The second order correction in $\frac{N_0}{N}$ expansion in the $N \gg N_{\mathrm{T}}$ limit has the trend $\sim \left(\frac{T}{T_c}\right)^2 N^{-\frac{1}{3}}$. Also T_c has to be corrected. Its correction δT_{c} depends on the trap symmetry as follows: $\frac{\delta T_{\mathrm{c}}}{T_c} \sim \frac{\bar{\omega}}{\omega_{\mathrm{ho}}} N^{-\frac{1}{3}}$. These are not, however, critical corrections. The condensed fraction is reduced, but stays macroscopic, see Fig. 1.3.

1.3 An interacting BEC: Short Range Interaction

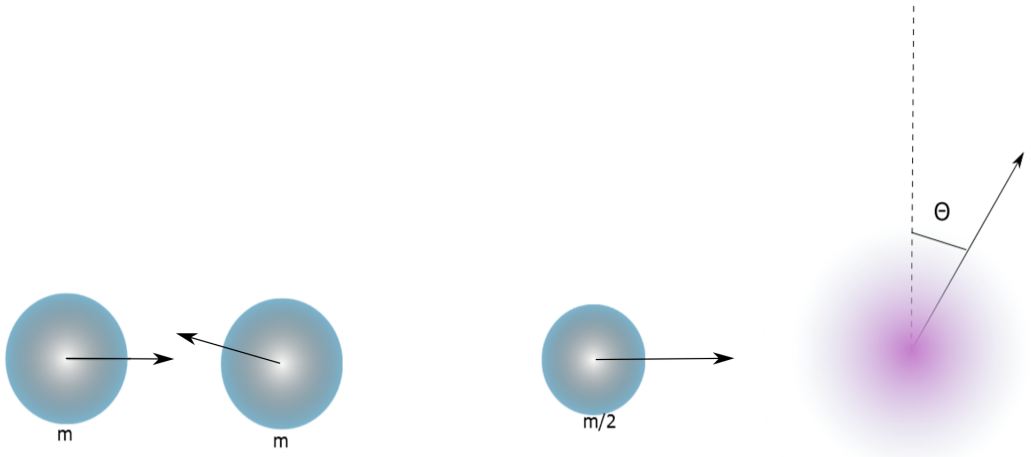

Figure 1.4: On the left an example of a two-body elastic collision is sketched, arrows represent the momenta. On the right the same situation is represented in terms of the centre of mass of the system. It is equal to the diffusion of an effective mass $m^* = \frac{m}{2}$ by a central potential $U_{\mathrm{int}}(d)$. θ is the scattering angle.

Up to now only non-interacting BECs have been considered. However, although quantum gases are very dilute systems (with densities typically ranging from 10^{14} to 10^{15} cm^{-3}, as compared to 10^{19} cm^{-3} in a gas and 10^{23} cm^{-3} in a solid), most of their properties are governed by the interaction between particles. In this section short range interactions are introduced.

A BEC is an example of low density quantum fluid as it meets the *diluteness condition*. Such condition is

$$r_0 \ll n^{-\frac{1}{3}} \tag{1.21}$$

where r_0 is the inter atomic potential range and $n^{-\frac{1}{3}}$ the mean distance between particles. This condition implies that two-body interaction is the relevant inter atomic one. Furthermore the distance between two particles is always large enough to justify the use of the asymptotic expression for the wave function of their relative motion, which is fixed by the scattering amplitude $f(\theta)$. This implies that $f(\theta)$ is the only important parameter and all quantities should be referred to it. Furthermore, interacting low temperature particles meet the additional condition

$$qr_0 \ll 1 \qquad . \tag{1.22}$$

At such momenta the interaction is an elastic low energy scattering, independent from the internal nature of the atoms.

The problem of two scattering atoms can thus be treated as a one particle diffusion by a central potential. A schematic representation in presented in Fig. 1.4. The form of the solution is

$$e^{iqz} + f(\theta)\frac{e^{iqd}}{d} \tag{1.23}$$

where d is the relative distance between atoms. The solution is the sum of an incoming plane wave and a spherical wave at large distances, modulated by the scattering amplitude $f(\theta)$. For a central potential the solution has axial symmetry and can be expanded in spherical harmonics. $f(\theta)$ is then determined by the combination of spherical harmonics with a relative phase δ_l. In the case of low energy and van der Waals interaction, thus $f \sim q^{2l}$ and $U_{\text{int}} \sim \frac{1}{d^6}$, the dominant contribution comes from the $l = 0$ term[5]. So for low momenta the scattering amplitude is independent of energy and is given by the s-wave scattering length a_{s}, which becomes the only important parameter.

From now on another condition than diluteness is considered: weakly interactions. It corresponds to the request

$$|a_{\text{s}}| \ll n^{-\frac{1}{3}} \tag{1.24}$$

or $n|a_{\text{s}}|^3 \ll 1$ where $n|a_{\text{s}}|^3$ is called *gas parameter*. A case where the previous condition is not satisfied is near a Feshbach resonance (see Sec. 1.3.4). In the next sections important tools to deal with weakly interacting diluted gas are introduced, then the expression for $n(r)$ is obtained in the Thomas Fermi approximation.

1.3.1 Bogoliubov approximation and Gross-Pitaevskii equation

The Hamiltonian of the system described above is:

$$\hat{\boldsymbol{H}} = \int d^3r \hat{\boldsymbol{\psi}}^\dagger(r)\Big[-\frac{\hbar^2}{2m}\nabla^2 + V_{\text{ext}}(r)\Big]\hat{\boldsymbol{\psi}}(r) + \frac{1}{2}\int d^3r d^3r' \hat{\boldsymbol{\psi}}^\dagger(r)\hat{\boldsymbol{\psi}}^\dagger(r')U_{\text{int}}(r-r')\hat{\boldsymbol{\psi}}(r')\hat{\boldsymbol{\psi}}(r) \tag{1.25}$$

where $U_{\text{int}}(r - r')$ is the isotropic short range scattering potential previously introduced. In general $\hat{\boldsymbol{\psi}}(r) = \sum_{\text{i}} \varphi_{\text{i}}(r)\hat{\boldsymbol{a}}_{\text{i}}$ where $\hat{\boldsymbol{a}}_{\text{i}}$ and $\hat{\boldsymbol{a}}_{\text{i}}^\dagger$ are the creation and annihilation operators satisfying:

$$\hat{\boldsymbol{a}}_{\text{i}}^\dagger \left|n_0, ..., n_{\text{i}}, ...\right\rangle = \sqrt{n_{\text{i}}+1}\left|n_0, ..., n_{\text{i}+1}, ...\right\rangle \tag{1.26}$$

$$\hat{\boldsymbol{a}}_{\text{i}} \left|n_0, ..., n_{\text{i}}, ...\right\rangle = \sqrt{n_{\text{i}}}\left|n_0, ..., n_{\text{i}-1}, ...\right\rangle \tag{1.27}$$

The so called Bogoliubov approximation consists in writing $\hat{\boldsymbol{\psi}}(r,t) = \hat{\boldsymbol{\psi}}_{\boldsymbol{0}}(r,t) + \delta\psi(r,t)$ where $\hat{\boldsymbol{\psi}}_{\boldsymbol{0}} = \hat{\boldsymbol{a}}_0\varphi_0(r,t)$ is the ground state while $\delta\psi(r,t)$ accounts for quantum fluctuations (see Sec. 1.5.1). The passage above is equivalent to substitute the operator $\hat{\boldsymbol{a}}_{\boldsymbol{0}}$ with the constant $\sqrt{N_0}$, i.e. to forget the non-commutativity of $\hat{\boldsymbol{a}}_{\boldsymbol{0}}$ and $\hat{\boldsymbol{a}}_{\boldsymbol{0}}{}^\dagger$. Such approximation takes the condensate as a thermal bath where $|N\rangle, \hat{\boldsymbol{a}}_{\boldsymbol{0}}{}^\dagger |N\rangle$ and $\hat{\boldsymbol{a}}_{\boldsymbol{0}} |N\rangle$ are the same state. It is then valid only in the $N_0 \gg 1$ limit as it assumes $N_0 \pm 1 \sim N_0$. In this approximation the operator $\hat{\boldsymbol{\psi}}_{\boldsymbol{0}}(r,t)$ is substituted with the analogous classic field ψ_0 with $\psi_0 = \langle\hat{\boldsymbol{\psi}}\rangle$. ψ_0 is a Landau order parameter that characterizes the phase of the system. If written in the form

$$\psi_0 = |\psi_0|e^{iS(t)} \tag{1.28}$$

gives $|\psi_0| = \sqrt{n_0}$ density of the condensate, and $S(t)$ the phase. Starting from Bogoliubov approximation

$$\hat{\boldsymbol{a}}_{\boldsymbol{0}} \sim \sqrt{N_0} \tag{1.29}$$

the low temperature limit $T \to 0$ is studied. It corresponds to

$$\psi_0 \gg \delta\psi \tag{1.30}$$

[5] This comes from the general result stating that, for a central potential falling off at large distances like $\frac{1}{d^n}$, and low momenta ($\hbar q \to 0$), the scattering phase shift $\delta_l(q)$ scales like: q^{2l+1} if $l < (n-3)/2$, q^{n-2} otherwise [36].

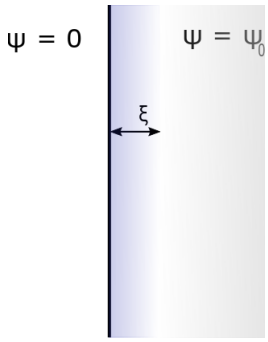

Figure 1.5: Representation of the edge of a BEC as a barrier. Outside the barrier the density is 0, inside a typical length scale is necessary to recover the Thomas-Fermi solution, i.e. the healing length.

The time evolution equation of ψ_0 is obtained using Heisenberg equation $i\hbar\frac{\partial}{\partial t}\hat{\boldsymbol{\psi}}(r,t) = [\hat{\boldsymbol{\psi}}, \hat{\boldsymbol{H}}]$. As for cold, slow atoms the condition $|U_{\rm int}| \ll \frac{\hbar^2}{2ma_{\rm s}^2}$ is not obviously satisfied, a pseudo potential is introduced to allow a perturbative theory approach to Heisenberg equation. The idea is to model the effects through an ad hoc flat potential that asymptotically reproduces the real effect, thus the radial waveform obtained considering the pseudo potential for $r > r_c$ matches the real one. This pseudo potential allows to use the perturbative theory. The short range forces having van der Waals trend $\sim \frac{1}{r^6}$ are well represented by an effective zero-range contact potential. The *ad hoc* potential has then the following form

$$U_{\rm int}(r - r') = g\delta(r - r') \tag{1.31}$$

$$g = \frac{4\pi\hbar^2 a_{\rm s}}{m} \tag{1.32}$$

in the coordinates space, while it is a constant in the velocity space, $\tilde{U}_{\rm int} = g$. The evolution equation is represented by the Gross-Pitaevskii time dependent equation

$$i\hbar\frac{\partial}{\partial t}\psi_0(r,t) = \Big(-\frac{\hbar^2}{2m}\nabla^2 + V_{\rm ext} + g|\psi_0|^2\Big)\psi_0(r,t) \qquad . \tag{1.33}$$

Because the interaction energy in Eq. 1.33 is a non linear Schroedinger equation, it has a non trivial solution. In the following we report the stationary solution in the Thomas Fermi approximation.

1.3.2 Thomas Fermi Approximation and Solution of G-P stationary equation

The energy functional is

$$E(\psi_0) = \int d^3r\Big(\frac{\hbar^2}{2m}|\nabla\psi_0|^2 + V_{\rm ext}|\psi_0|^2 + \frac{g}{2}|\psi_0|^4\Big) = E(n) \tag{1.34}$$

where the first term is the kinetic energy of the system, the second takes into account an external potential $V_{\rm ext}$ and the third the contact interparticle interactions. The Thomas Fermi limit is the limit in which one can ignore the kinetic energy term in the equation. Let's study the range of validity.

The competition between interaction energy and kinetic energy fixes a characteristic length. It is a correlation length and is called *healing length* ξ. To make its significance clear, the critical region where the Bogoliubov approximation is no longer valid is considered. Such a region is the sample surface, here in fact $|\nabla\psi_0|^2$ is all but negligible. This edge can be thought as an infinite barrier, as sketched in Fig. 1.5. Which is the typical length scale for ψ to recover the solution

ψ_0? Since far away from the edge ψ is determined by the competition between $U_{\rm int}$ and kinetic energy, the sought scale is given by

$$ng \sim \frac{\hbar^2}{2m\xi^2} \tag{1.35}$$

$$\xi^2 = \frac{1}{8\pi n a_{\rm s}} \sim \frac{r_{\rm s}^3}{a_{\rm s}} \tag{1.36}$$

where $r_{\rm s}$ is the average radius occupied by a particle. The healing length is then the distance after which ψ is exactly the Thomas Fermi solution ψ_0.

Finally, let's comment the healing length in relation to the Bogoliubov excitation spectrum. These is formally derived linearising the G-P equation in Eq.1.33, it results

$$E(q)^2 = \Big(\frac{\hbar^2 q^2}{2m}\Big)\Big(\frac{\hbar^2 q^2}{2m} + 2gn\Big) \tag{1.37}$$

see Fig. 1.6. The healing length ξ is the length scale for the free-particle spectrum to be recovered. Introducing the Thomas Fermi limit the Gross-Pitaevskii stationary equation is now solved. Substituting in Eq. 1.38 the expression in Eq. 1.39 the time independent Gross-Pitaevskii is obtained in Eq. 1.40.

$$\Big(-\tfrac{\hbar^2}{2m}\nabla^2 + V_{\rm ext} + g|\psi_0|^2\Big)\psi_0(r,t) = 0 \tag{1.38}$$

$$\psi_0(r,t) = \psi_0(r)e^{-i\mu\frac{t}{\hbar}} \tag{1.39}$$

$$-\tfrac{\hbar^2}{2m}\nabla^2\psi_0(r) + V_{\rm ext}(r)\psi_0(r) + g|\psi_0|^2\psi_0(r) = \mu\psi_0(r) \tag{1.40}$$

If the Thomas Fermi limit is used, i.e. kinetic effect are neglected, the Eq. 1.40 becomes

$$[V_{\rm ext}(r) + g|\psi_0|^2]\psi_0(r) = \mu\psi_0(r) \tag{1.41}$$

whose solution is an inverted parabola

$$n(r) = |\psi_0(r)|^2 = \begin{cases} \frac{\mu - V_{\rm ext}(r)}{g}, & \text{for } \mu > V_{\rm ext} \\ 0 & \text{elsewhere} \end{cases} .$$

μ is obtained from the equation for the normalization for ψ_0:

$$N = \int_0^{R^*} n(r)d^3r = \int_0^{R^*} \frac{\mu - V_{\rm ext}(r)}{g} d^3r = \frac{8\pi}{15}\Big(\frac{2\mu}{m\omega_{\rm ho}^2}\Big)^{\frac{3}{2}}\frac{\mu}{g} \tag{1.42}$$

where N is the atom number and R^* represents the extension of the sample. It follows

$$\mu = \Big(\frac{15N|a_{\rm s}|}{a_{\rm ho}}\Big)^{\frac{2}{5}}\frac{\hbar\omega_{\rm ho}}{2} \tag{1.43}$$

In the end, R^* is obtained imposing the edge condition $\mu = V_{\rm ext}(R^*)$ and considering that for each oscillator $\mu = \frac{1}{2}m\omega_k^2 R_k^{*2}$, for the k direction. It results

$$R_k^* = \sqrt{\frac{2\mu}{m\omega_k^2}} = a_{\rm ho}\Big(\frac{15Na_{\rm s}}{a_{\rm ho}}\Big)^{\frac{1}{5}}\frac{\omega_{\rm ho}}{\omega_k} \gg a_{\rm ho} \quad . \tag{1.44}$$

In particular, while without interaction the condensate dimension is N-independent (see Eq. 1.58), by adding an interaction potential it scales with $N^{\frac{1}{5}}$. The important parameter introduced is

$$\frac{Na_{\rm s}}{a_{\rm ho}} \tag{1.45}$$

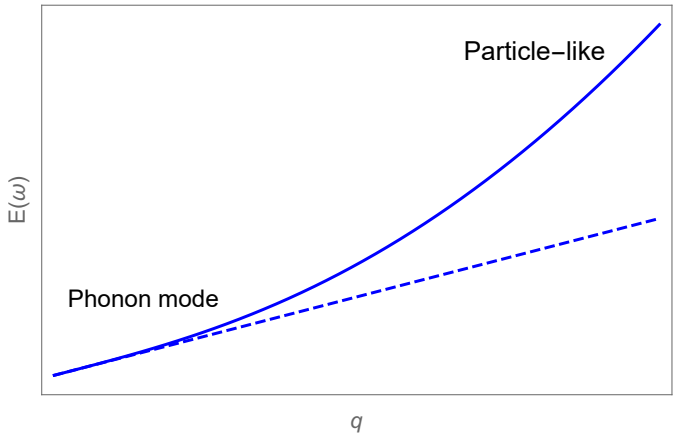

Figure 1.6: Bogoliubov excitation spectrum (solid line) obtained from Eq. 1.37. Low momenta show a phonon like dispersion (dashed line), i.e. a linear behaviour. A parabolic curve is then recovered on a scale of the order of the inverse of the healing length ξ. The parabolic feature corresponds to the free particle spectrum.

the atoms are as pushed away as it grows. Therefore in respect to the non-interacting case, R^* increases while the maximum density is lowered.

This feature is expressed in the formulas below, where Eq. 1.7 is used for φ_0

$$n_{TF}(0) = \frac{\mu}{g} \tag{1.46}$$

$$n_{non-int}(0) = N_0|\varphi_0(0)|^2 = \frac{N}{\pi^{\frac{3}{2}} a_{\rm ho}^3} \tag{1.47}$$

$$\frac{n_{TF}(0)}{n_{non-int}(0)} = \frac{15^{\frac{2}{5}}\pi^{\frac{1}{2}}}{8}\left(\frac{N a_{\rm s}}{a_{\rm ho}}\right)^{-\frac{3}{5}} \ll 1 \tag{1.48}$$

The significance of the parameter in Eq. 1.45 is discussed in the Sec. 1.3.5. In the end the energy per particle in T-F regime is recovered. By integrating $\mu = \frac{\partial E}{\partial N}$, it results $\frac{E_{TF}}{N} = \frac{5}{7}\mu_{TF}$.

Two-body interactions determine the properties of the BEC. However some phenomena are characterized by a loss feature related to three body processes. Because of this, three body recombinations are now briefly discussed.

1.3.3 Three Body recombination

In the previous section two-body contact interactions were discussed. In particular, the effective length scale of the interaction, i.e. the scattering length $a_{\rm s}$, was introduced. Another key interaction constant is the three body recombination constant K_3 [37].

Three-body recombination is an inelastic scattering process consisting in the interaction among three atoms, whose final state is a free atom and a molecule. Two atoms cannot combine directly because it is impossible to get rid of the binding energy of the molecule. The most effective way of satisfying the conservation laws for energy and momentum under typical experimental conditions is for a third atom to participate in the reaction (see Fig. 1.7).

The released binding energy of the molecule is converted into kinetic energy. In a trapped gas the molecule and the atom are then no longer trapped and get lost. This phenomenon is called three body loss. For thermal samples the rate of the recombination process is

$$\frac{{\rm d}n}{{\rm d}t} = -K_3 n^3 \tag{1.49}$$

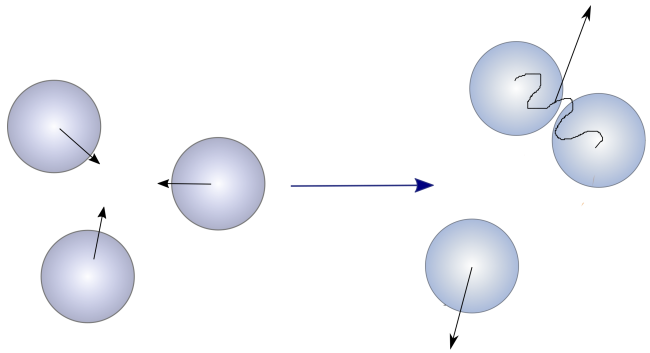

Figure 1.7: Three body recombination: three atoms collide and form a diatomic molecule and a free atom, with an excess kinetic energy resulting from the molecular binding energy.

where K_3 is the three body recombination coefficient for a thermal gas. The rate is proportional to n^3 where n is the atomic density.

Such dependence on n is easy to understand in the case of alkali atoms, i.e. with only contact interactions, since the process is related to the probability for the 3 atoms to be in a volume r_0^3, where r_0 is the characteristic length of the interaction. Such a probability is proportional to nr_0^3, thus for three atoms involved a rate $\propto n^3$ is expected. Because of its important dependence on the density, three-body recombination prevents the presence of high densities in the trap, limiting the peak density of the atomic cloud.

For alkali/lanthanide atoms K_3 is typically of the order of 10^{-29} cm^6/s [4]. The loss rate is obtained integrating Eq. 1.49. It results

$$\frac{1}{N}\frac{\mathrm{d}N}{\mathrm{d}t} = -K_3 < n^2 > \tag{1.50}$$

the coefficient K_3 is therefore related to the decay time of the number of atoms in the trap τ_{loss} by the relation $\tau_{loss} = 1/(K_3\langle n^2\rangle)$ [28]. In the case of a condensate, since atoms are all in the same state, the collisional properties change and a factor 1/6 is need [38]. The previous equation then becomes

$$\frac{1}{N}\frac{\mathrm{d}N}{\mathrm{d}t} = -\frac{K_3}{6} < n^2 > \quad . \tag{1.51}$$

Another important effect of three-body recombination is the heating of the sample. Three-body losses in fact are enhanced in the higher density regions, i.e. the centre of the cloud. Colder atoms escape from the trap and the sample thermalizes at higher temperature [37]. Furthermore the sample is heating if the energy released is not enough to make the atom and molecule leave the trap [39]. The probability of three-body recombinations increases near a Feshbach resonance. Such resonances are an important tool for the tuning of contact inter-particle interactions and are thus presented in the next section.

1.3.4 A tunable interaction: Feshbach resonances

A Feshbach resonance arises when, in the collision of two atoms, an 'open' channel and a 'closed' channel are resonantly coupled. Feshbach resonances formalism consists in treating the phenomenon as the coupling between two potentials: V_{bg} and V_{c} (see Fig. 1.8). Along the V_{bg} potential atoms enter and leave the scattering region elastically (it corresponds to the open channel). Along the V_{c} potential the internal state of atoms can instead get changed (it corresponds to the closed channel). Atoms may become trapped in a bound molecular state. These two potentials are thus respectively accounting for an open channel (V_{bg}) and a closed channel (V_c). In ultra cold gases Feshbach resonances are particularly relevant as they introduce the possibility of an in situ modification of the atoms interaction. This is equivalent to state

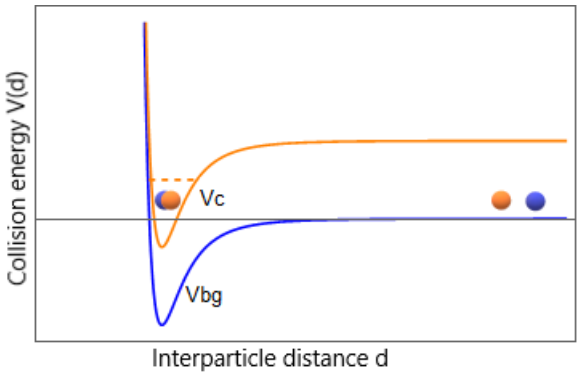

Figure 1.8: Open and closed channel of an interaction. The open channel correspond to an elastic scattering where the particles are asymptotically free, while the closed channel supports the formation of a molecule. Dashed line represents the bound state tunable by an external field, it gives rise to the resonance when it reaches the zero axis.

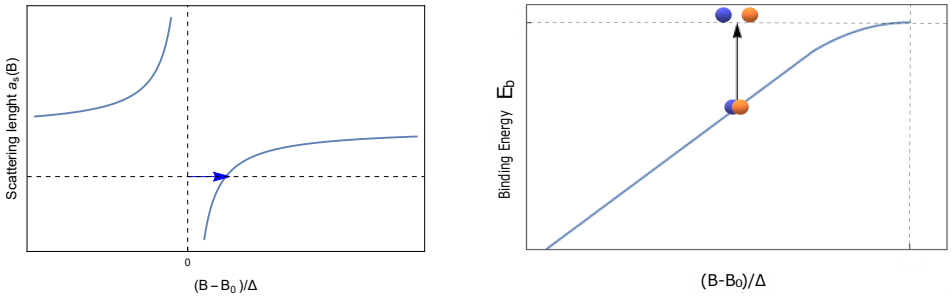

(a) (b)

Figure 1.9: **a**. Scattering length vs magnetic field. On one side of the resonance the scattering length has a zero. **b**. Binding Energy of the molecular state: it has a linear trend far from the resonance, while near to it becomes quadratic.

that Feshbach resonances allow to control the scattering length a_s. Such control has a magnetic nature if the two channels have different magnetic moments $\mu_{bg} - \mu_c = \delta\mu \neq 0$, thus they are differently affected by an external magnetic field. Zeeman splitting is used to control the closed channel potential and to realize the resonance condition.

Here the main features and typical trends of related processes are reported (for a more general discussion see Ref. [8]). The background scattering length a_{bg} is the value associated with V_{bg}, thus out of resonance. In the proximity of a Feshbach resonance, the scattering length is modified as a function of an external magnetic field, according to

$$a_s(B) = a_{bg}(1 - \frac{\Delta}{B - B_0}) \tag{1.52}$$

where Δ is the resonance width and B_0 the centre of the resonance, i.e. the field value for a divergent scattering length $a_s \to \pm\infty$. The curve is represented in Fig. 1.9a.

Another interesting trend is the one of the bound energy E_b of the molecular state (see Fig. 1.9b). Out of resonance E_b is linearly dependent on B with an angular coefficient $\delta\mu$ (difference between two Zeeman splitted levels). As the resonance is approached, $E_b \to 0$ quadratically, since the coupling bends the molecular state. For $a_s \gg 1$ a *detuning dressed*

molecular state exists (see Ref. [8]) with a binding energy

$$E_b = \frac{\hbar^2}{2a_s^2\mu} \propto (B - B_0)^2 \tag{1.53}$$

The corresponding curve is shown in Fig. 1.9b. The wave function of this bound state is said to be a *quantum halo*. It extends for a length $a_{\text{eff}} \sim$ scattering length of the effective potential.

The last important feature of Feshbach resonances is the relation to three body recombination. Thanks to the large extension of the quantum halo, three body interactions are enhanced, $K_3 \propto |a_s|^4$ [14], near a Feshbach resonance. The binding energy released by the system is converted into kinetic energy. Therefore, the molecule and the free atom involved in the process escape from the trap. Feshbach resonances are then characterized by a loss feature.

1.3.5 A competition among energies

A weakly interacting regime has been considered so far. In order to asses in which regime the BEC operates, the contact interaction energy U_{int} has to be compared with the kinetic energy in the trap, E_{kin}. For the ground state in a 3D harmonic trap

$$U_{\text{int}} \sim gN\bar{n} \quad \text{where} \quad \bar{n} \sim \frac{N}{a_{\text{ho}}^3} \quad \text{so} \quad U_{\text{int}} \sim N^2\frac{|a_s|}{a_{\text{ho}}^3} \tag{1.54}$$

$$E_{\text{kin}} = N\hbar\omega_0 \sim Na_{\text{ho}}^{-2} \tag{1.55}$$

$$\frac{U_{\text{int}}}{E_{\text{kin}}} \sim \frac{N|a_s|}{a_{\text{ho}}} \quad . \tag{1.56}$$

The parameter expressed in Eq. 1.45 characterizes the interaction forces. It is also clear by writing a rescaled Gross-Pitaevskii equation by using a_{ho} as the length scale, a_{ho}^{-3} density scale and $\hbar\omega_{\text{ho}}$ energy scale

$$\Big[-\tilde{\nabla}^2 + \tilde{r}^2 + 8\pi\Big(\frac{Na}{a_{\text{ho}}}\Big)\tilde{\Phi}^2(\tilde{r})\Big]\tilde{\Phi}(\tilde{r}) = 2\tilde{\mu}\tilde{\Phi}(\tilde{r}) \tag{1.57}$$

where $\tilde{\nabla}$, $\tilde{r}$, $\tilde{\Phi}$ and $\tilde{\mu}$ are the rescaled quantity. The interaction order is characterized by the parameter in Eq. 1.45, furthermore the interaction depends on the sign of the scattering length a_s. For a large number of atomic species, the magnitude and even the sign of the scattering length can be tuned by means of an external magnetic field. A qualitative analysis is then proposed for: repulsive forces ($a_s > 0$), attractive forces($a_s < 0$), no interaction ($a_s = 0$).

No interaction, $a_s = 0$

If no interactions are present then the potential energy per particle U is given only by the trap, $U \sim m\omega_0^2\frac{r^2}{2}$ where r is the radius of the sample, and $E_{\text{kin}} \sim \frac{\hbar^2}{2m}\frac{1}{r^2}$. At short r kinetic effects dominate, while at long r trapping effects are the important ones. The equilibrium radius is

$$R^* \sim a_{\text{ho}} \tag{1.58}$$

as it is shown in Fig. 1.10.

Repulsive force, $a_s > 0$

The net effect is an increase of the equilibrium radius R^* in Eq. 1.44. The repulsive potential is $U_{\text{int}} \sim ng \sim +\frac{1}{r^3}$. The trends of competing terms ratios are: $\frac{U_{\text{int}}}{E_{\text{kin}}} \sim \frac{1}{r}$ and $\frac{V_{\text{ext}}}{E_{\text{kin}}} \sim r^4$. Therefore U_{int} is the dominant potential for small R values. For large extension, however, trapping effects are the relevant ones. The single particle potential as a function of R is shown in Fig. 1.11a.

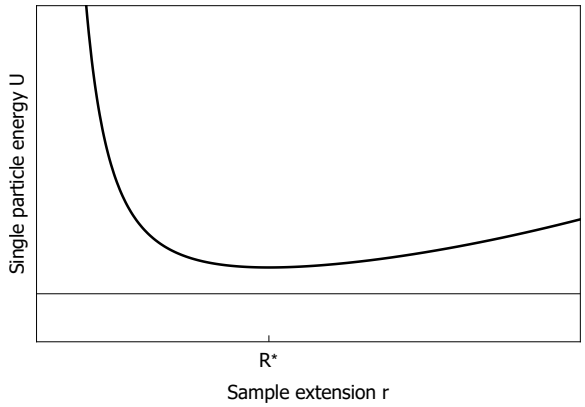

Figure 1.10: Qualitative representation of the single particle energy as a function of the sample extension for a non interacting sample. The equilibrium size is $R^* = a_{\rm ho}$.

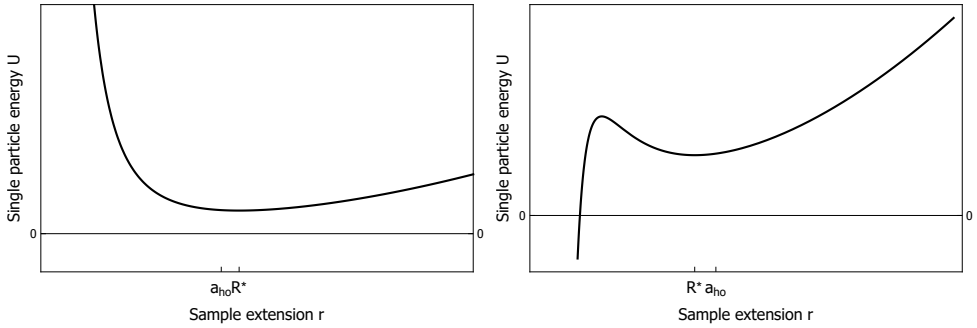

(a) (b)

Figure 1.11: Qualitative representation of the single particle energy as a function of the sample extension for an interacting sample. **a**. Representation of the case of a repulsive interaction between atoms. In this case $R^* > a_{\rm ho}$. **b**. Representation of the single particle potential accounting for an attractive interaction. In this case $R^* < a_{\rm ho}$.

Attractive force, $a_{\rm s} < 0$

The equilibrium extension R^* in this very peculiar case is N dependent. If the atom number is small enough a local minimum is realized. It is a metastable state, that is reached at $R^* < a_{\rm ho}$ as shown in Fig. 1.11b. Increasing N, the minimum becomes flatter and flatter until, reached $N = N_{\rm c}$, once it disappears (see Fig. 1.12). $N_{\rm c}$ is the one realizing the condition $V_{\rm ext}(r \sim a_{\rm ho}) \sim U_{\rm int}(r \sim a_{\rm ho})$, so it follows $N_{\rm c} \sim \frac{a_{\rm ho}}{|a_{\rm s}|}$. In the presence of attractive force the gas tendency is to increase the central density $n(0)$, to minimize the energy. A collapse is then expected for $N > N_{\rm c}$ and the G-P equation has no longer solution. However, this trend can be contrasted by beyond mean field effects. This aspects will be more specifically investigated in Sec.s 1.4.3 and 1.5.1.

1.4 An interacting BEC: Long range and anisotropic interaction

So far only short-range van der Waals interactions ($\sim 1/d^6$, d interparticle distance) have been considered. Now also dipole-dipole interactions are considered. Dipole-dipole interaction (DDI) acts between particles having an electric or magnetic permanent dipole moment and should lead to a novel kind of degenerate quantum gases, already in the weakly interacting limit. The importance of DDI comes from their long range ($\sim 1/d^3$) and anisotropic character. The anisotropic nature

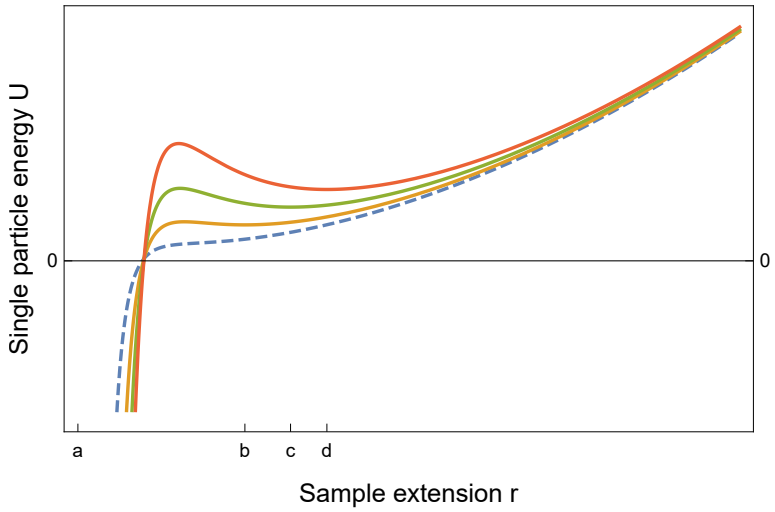

Figure 1.12: Qualitative representation of the single particle energy as a function of the sample extension, for different atom number N. Continuous lines correspond to $N > N_c$, in this case a finite size equilibrium exists. Dashed line corresponds to $N \sim N_c$, the finite-size local minimum disappears. a, b, c, d are the equilibrium radii (d is the one relative to the higher energy curve. While a is the one relative to the dashed line).

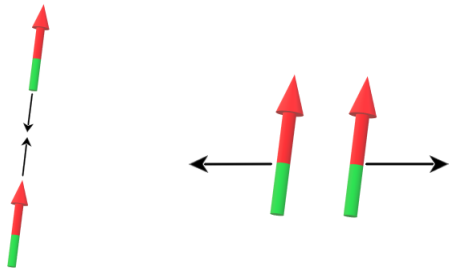

Figure 1.13: Dipole-dipole configurations. **a**. Representation of a head-to-tail configuration. This leads to an attractive DDI. **b**. Sketch of dipoles sitting side-by-side. They repel each other thus corresponding to a repulsive interaction configuration.

of this interaction implies that it could be either repulsive or attractive depending on the relative orientation of the two dipoles. Side by side particles interact with repulsive DDI, see Fig. 1.13b, while a 'head-to-tail' configuration correspond to an attractive one, see Fig. 1.13a. For the special value $\theta_m = \arccos\left(\frac{1}{\sqrt{3}}\right) \sim 54.7°$, the so-called 'magic-angle' used in high resolution solid-state nuclear magnetic resonance [40] , the dipole-dipole interaction vanishes.

This anisotropic interaction leads to a series of interesting phenomena even in classical physics, a fascinating example is the Rosensweig instability (see Sec. 1.5.2). For dipolar quantum gases the DDI is related to the observation of a maxon-roton spectrum and to the stability property of the system. In the mean field approximation developed in this chapter the maxon-roton spectrum theory is discussed as well as the stability and collapse of the BEC. Experimental observations are also briefly reported.

1.4.1 DDI: Dipole-Dipole Interactions

The dipole dipole interaction is represented in Fig. 1.14a for a non polarized sample. If an external magnetic field is introduced, dipoles are aligned all in the same direction as shown in Fig 1.14b. The expression for a polarized sample is:

$$U_{dd} = \frac{C_{dd}}{4\pi} \frac{1 - 3\cos^2\theta}{d^3} \tag{1.59}$$

where d is the distance between the dipoles, θ is the angle between the polarization axis and dipole relative distance, and C_{dd} is a constant that depends on the interaction realization. If magnetic dipoles are involved then $C_{dd} = \mu_0 \mu_{\mathrm{m}}^2$, while for electric dipoles $C_{dd} = \frac{\epsilon_{\mathrm{m}}^2}{\epsilon_0}$; ϵ_{m} and μ_{m} are the electric or magnetic moment of the particle while $\epsilon_0 \sim 8.85 \times 10^{-12}$ [F/m] and $\mu_0 = 4\pi \times 10^{-7}$ [H/m] are the vacuum permeability and permettivity.

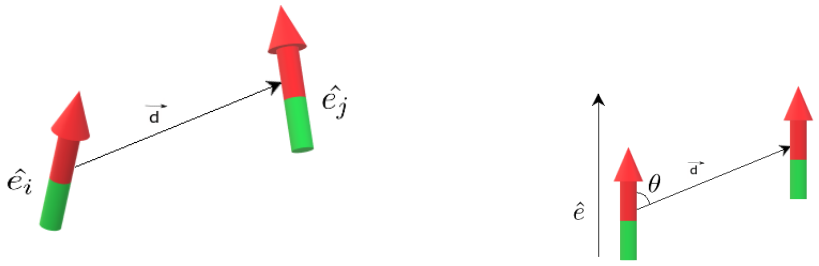

(a) (b)

Figure 1.14: Dipole-dipole interaction. r is the relative distance between dipoles. **a**. Interaction for a non polarized sample. Versors $\hat{e}_{\mathrm{i}}$ and $\hat{e}_{\mathrm{j}}$ indicate the dipoles orientation. **b**. DDI for a polarized sample. The versor $\hat{e}$ indicates the external magnetic field direction, along which dipoles align. θ is the angle between $\hat{e}$ and $\vec{d}$.

Magnetic dipolar interaction was experimentally realized with a condensate of atoms with a permanent magnetic moment. Historically the first dipolar condensate was realized with Chromium atoms [16], with $\mu_m \sim 6\mu_B$, where $\mu_B = \frac{e\hbar}{2m_e}$ is the Bohr magneton. Nowadays also Erbium condensates have been obtained with $\mu_m \sim 7\mu_B$, as well as Dysprosium, which has a permanent magnetic moment $\mu_m \sim 10\mu_B$. The electric DDI is also possible and is implemented by several systems: polar molecules, Rydberg atoms and light-induced dipoles.

Formally, to account for dipole-dipole interactions, the s-wave contribution to the scattering amplitude is not sufficient. The slow decay as $\frac{1}{d^3}$ at large distances implies that all partial waves contribute to the scattering at low momentum, since $\delta_l \approx q$ for all partial waves [41]. Moreover, because of the anisotropic character of the interaction, partial waves with different angular momenta couple with each other. This coupling can be neglected in a first-order Born approximation [42]. In this approximation the total interaction potential, accounting also for contact interactions, is described by a pseudo potential.

$$V = g(a_s)\delta(d) + \frac{\mu_0\mu_m^2}{4\pi}\frac{1-3\cos^2\theta}{d^3} \equiv g(a_s)\delta(d) + \frac{4\pi\hbar^2 a_{dd}}{m}\frac{1-3\cos^2\theta}{d^3} \quad . \tag{1.60}$$

Here, a characteristic length has been introduced, $a_{dd} = \frac{m\mu_0\mu_m^2}{12\pi\hbar^2}$, denoted as 'dipolar length'. It is defined as the length for which an homogeneous 3D condensate becomes unstable in the Thomas Fermi limit. A dipole strength is also introduced $g_{dd} = \frac{\mu_0\mu_m^2}{3}$ and a relative strength $\epsilon_{dd} = \frac{g_{dd}}{g} = \frac{a_{dd}}{a}$. For a BEC to be dominated by dipolar effects, the dipolar interaction needs to be at least as strong as the contact interaction giving $\epsilon_{dd} \geq 1$. From the angular dependence in Eq. 1.60 it is clear the anisotropic nature of DDI. The long range interaction character is instead given by the $\sim 1/d^3$ trend according to the long-range character definition[6] (see Ref. [41]). In the next section a very important consequence of the anisotropy of DDI is presented.

1.4.2 Roton mode

In superfluid systems a roton mode is expected in the strong interaction regime between particles (see Fig.1.15). In Landau's theory the thermodynamics of a superfluid is explained by including two quasi-particles at low energy: phonons (small momentum) and rotons (larger momentum) (see Ref. [43]). In ^{4}He the roton formation mechanism is the competition between attractive van der Waals forces and repulsive Coulomb force, the roton momentum q_{rot} is then of the order of $\bar{d} = (\langle n \rangle)^{-1/3}$ and it scales as the inverse of the interatomic distance. A BEC instead is a dilute system as it satisfies the diluteness condition ($r_0 \ll n^{-1/3}$). In a normal BEC the dispersion law is that of Bogoliubov so no roton mode is present (see Fig. 1.6). Anyway this result changes for dipolar quantum gases because of the partially attractive character of DDI. The roton mode is then due to the competition between an attractive and a repulsive force that leads to a local minimum at finite momentum. Therefore, contrary to liquid He the roton mode in dipolar BEC is expected in the weak interaction regime. However, just like the He, it is due to the genuine interaction between atoms.

Other examples of systems where a roton excitation spectrum is expected are somewhat 'artificial' system as the roton is driven by external manipulations. Such systems are for example BECs with spin-orbit coupling, BECs in shaken optical lattices and BECs irradiated by off resonant laser light [44] . In the first two examples the idea is to control the single particle excitation spectrum inducing a 'double well' structure. The degeneracy of the two wells is then externally controlled and eventually lifted resulting in a maxon-roton excitation spectrum, see Fig. 1.16. In the last example, the attractive force is due to a DDI as well as in dipolar BECs, the typical q_{rot} scale is fixed by the inverse of the wavelength λ_{laser} irradiating the system. The

[6] In a system of particles interacting via short-range interactions, the energy is extensive in the thermodynamic limit. On the contrary, in systems with long-range interactions, the energy per particle does not depend only on the density, but also on the total number of particles. It is easy to see that a necessary condition for obtaining an extensive energy is that the integral of the interaction potential $V_{int}(d)$

$$\int_{r_0}^{\infty} V_{int}(d) d^D d \tag{1.61}$$

where D is the dimensionality of the system and r_0 some short-distance cut off, converges at large distances. For interactions decaying at large distances as $1/d^n$, this implies that one needs to have D $< n$ in order to consider the interaction to be short-range. Therefore, the dipole-dipole interaction ($n = 3$) is marginally long-range in three dimensions, and short range in one and two dimensions.

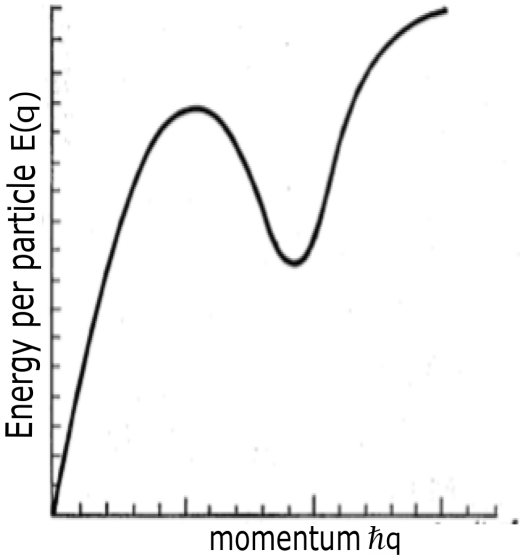

Figure 1.15: Figure adapted from [43]. Dispersion law $E(q)$ of elementary excitations of superfluid He. After the initially linear growth, the function reaches a maximum. Then it decreases and for a specific value of the momentum it has a minimum.

basic idea in dipolar gases is to start from a system where the trap constrains the dimensionality of the system to be 2D (pancake-like) or 1D (sigar-shape) where the confined dimension is the one parallel to the polarizing external field $\vec{B}$. The dipoles are then constrained in a side-by-side repulsive configuration, see Fig. 1.24. Such a system corresponds to a phononic spectrum for low $q_{\mathrm{x}}, q_{\mathrm{y}}$, where x and y are the direction perpendicular to $\vec{B}$.

The contact interaction can then be tuned by using a Feshbach resonance. When a_s reaches a critical value the dipoles become sensitive to each other for distances smaller than σ_z, the vertical confinement. It is like an effective 3D dimension has been recovered and head-to-tail configuration is again allowed. This attractive term leads to a new minimum of the system, namely 'roton' in analogy with ^{4}He, with a finite momentum of the order of $q_{\mathrm{rot}} \sim 1/\sigma_z$ [25]. The spectrum is reported in Fig. 1.16. These excitations in the momentum space correspond to a density modulation in the real space of period $\frac{2\pi}{q_{\mathrm{y}}} \sim 2\pi\sigma_z$. Also a phonon wave is a density modulation, the difference between the two is shown in Fig. 1.16. q_{rot} and the excitation energy at the roton minimum, typically indicated as the 'roton-gap' $\Delta = E(q_{\mathrm{rot}})$, are now determined according to Ref. [25].

The starting point is the G-P equation accounting also for DDI (see Eq. 1.70). As the ground state $\psi_0(r,t)$ is independent of r, the coordinate in the plane perpendicular to the polarization axes, it can be written as $\psi_0 = \phi_0(z)e^{-i\mu t/\hbar}$ and the equation can be integrated over r' in the DDI term

$$\Big(-\frac{\hbar^2\nabla^2}{2m} + \frac{m}{2}\omega_z^2 z^2 + (g+g_{dd})\phi_0^2(z)\Big)\phi_0(z) = \mu\phi_0(z) \qquad . \tag{1.62}$$

Eq. 1.62 is equivalent of a stationary G-P equation with an effective short-range interaction. The equation is solved in the TF limit

$$\phi_0^2(z) = n_0\Big(1 - \frac{z^2}{R_{\mathrm{z}}^2}\Big) \tag{1.63}$$

with $n_0 = \mu/(g+g_{dd})$ peak density, $R_{\mathrm{z}} = (2\mu/(m\omega_z^2))^{\frac{1}{2}}$ the z direction TF radius and μ the chemical potential of the system. The spectrum of the elementary excitations is then given linearising Eq. 1.62 around the solution 1.63. Two cases are distinguished:

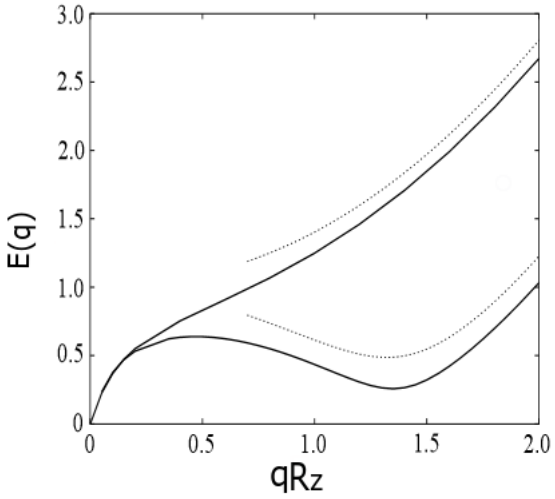

Figure 1.16: Figure taken from [25]. Dispersion law ϵ for different values of the parameter $\epsilon_{\rm dd}$ and $\mu/\hbar\omega$. The upper curve corresponds to $\epsilon_{\rm dd} \sim 1.9$ and $\mu/\hbar\omega = 46$. The lower curve is relative to the values $\epsilon_{\rm dd} \sim 2.13$ and $\mu/\hbar\omega = 54$. Solid lines are obtained by numerical simulations while dotted curves using Eq. 1.64. $R_{\rm z}$ is the Thomas-Fermi radius along the polarization direction.

- $q_\perp R_{\rm z} \ll 1$. The excitation spectrum is analogous of that of a trapped condensate with an effective short-range constant coupling $(g + g_{dd}) > 0$. It is phonon-like for small momenta and then parabolic.
- $q_\perp R_{\rm z} \gg 1$. The effective short-range constant coupling is lowered by the negative contribution of DDI, $(2g - g_{dd}) = g(2 - \epsilon_{dd})$. For $\epsilon_{dd} = 1$ the effective constant coupling vanishes, the dispersion law is characterized by a plateau. For $\epsilon_{dd} \neq 1$ the assumption that the coupling term does not significantly modify the eigenfunction is done: $\frac{\mu E_{q_\perp}|1/\epsilon_{dd}-1|}{1+1/2\epsilon_{dd}} \ll \hbar^2\omega_z^2$ with $E_{q_\perp} = \frac{\hbar^2 q_\perp^2}{2m}$, i.e. the Thomas-Fermi expression is still valid. The lowest branch is then

$$E^2(q) = E_{q\perp}^2 + \frac{(1/\epsilon_{dd} - 1)(5 + 1/\epsilon_{dd})}{3(1 + 1/2\epsilon_{dd})(2 + 1/2\epsilon_{dd})}\mu E_{q_\perp} \tag{1.64}$$

For DDI dominant regime $\epsilon_{dd} > 1$, in particular for $\epsilon_{dd} \sim 1$, roton momentum and energy can then be obtained as

$$q_{\rm rot} = \Big(\frac{16\mu(1 - 1/\epsilon_{dd})}{30\hbar\omega_z}\Big)^{\frac{1}{2}} \frac{1}{L_z} \tag{1.65}$$

$$\Delta = \Big[\hbar^2\omega_z^2 - \Big(\frac{8\mu(1 - 1/\epsilon_{dd})}{30}\Big)^2\Big]^{\frac{1}{2}} \tag{1.66}$$

The first observation of a roton mode in a dipolar quantum gas is described at the end of the Chapter. In the next section roton-mode softening, as well as phonon-mode softening is discussed; in other words the instability regime of a dipolar system is studied.

1.4.3 Instabilities.

As seen in the previous Sec. 1.3.5 the presence of an attractive potential introduces a local minimum (see Fig. 1.12) and a stability critical parameter. Stability of a trapped dipolar quantum gas is studied in this section, following this scheme:

1. 3D homogeneous dipolar gases are considered. Instabilities are studied analysing the dispersion curve.
2. 2D homogeneous dipolar gases are presented. In particular a *quasi-2D* regime and an *effective-3D* regime are distinguished.
3. Trapped dipolar gases are discussed in a T-F regime. First the G-P equation solution in a cylindrical trap is reported. Then the stability of the system is studied in terms of excitation modes.

The subject is here summarized with very simple formalism. Further information can be found in Refs. [41, 45, 46].

3D homogeneous dipolar gases

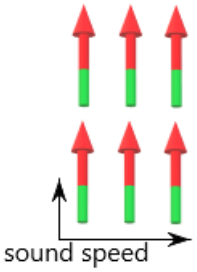

Figure 1.17: Representation of the sound speed with $\theta = 0$ and $\theta = \pi/2$.

Starting from the Gross-Pitaevkii equation, taking into account the dipolar term, a continuity equation for ψ can be written. The wave function can then be substituted by the expression in Eq 1.28 and the system is equal to a hydrodynamic system of equations that, linearised with small density perturbation gives the dispersion curve [4]. The same result is obtained by using a second quantization formalism starting from Bogoliubov approximation (see Sec. 1.3.1). The resulting excitation dispersion curve is:

$$E(q) = \hbar\omega(q) = \sqrt{\left(\frac{\hbar^2 q^2}{2m}\right)^2 + \frac{\hbar^2 q^2}{2m} 2n_0 \Big(g - g_{dd}(1 - 3\cos^2(\theta))\Big)} \tag{1.67}$$

which means linear, i.e. phononic, for small momenta and parabolic, i.e. free particle, for larger ones. Phonons are quasi-particles describing the normal oscillation modes of a system, so strictly connected to the sound speed. Their dispersion law is $E_{\mathrm{ph}} = qc_{\mathrm{s}}$ where

$$c_{\mathrm{s}} = \lim_{q\to 0} \frac{E(q)}{q} = \sqrt{\frac{n_0 g}{m}} \sqrt{1 - \epsilon_{dd}(1 - 3\cos^2(\theta))} \tag{1.68}$$

The presence of DDI induces an anisotropy in the sound speed, which has a maximum for $\theta = 0$ and a minimum for $\theta = \pi/2$ (see Fig. 1.17). This anisotropy has been experimentally measured for Chromium atoms [20]. c_{s} is defined by Newton-Laplace equation $c_{\mathrm{s}} = \sqrt{\frac{k_s}{\rho}}$ where k_s is a stiffness coefficient, describing the resistance of a system to compression. A large c_{s} value corresponds to a very stable system against compression, while a small c_{s} value corresponds to a softening of the phonon mode that leads to an instability for $g < g_{dd}$. This instability corresponds to a head-to-tail configuration, $\theta = \pi/2$ with the dipoles lying on the high density planes created by the density wave, see Fig. 1.18b.

Pure dipolar 3D systems ($g = 0$) are then unstable as the number of dipoles increases because they tend to configure in a head-to-tail configuration and, for a sufficiently large N, they lead to a macroscopic collapse.

(a) (b)

Figure 1.18: Density planes created by the density wave due to roton interaction. In figure (a) repulsive interactions lead to high density plane perpendicular to dipoles. The system is stable. In figure (b) attractive interactions leads to dipoles lying on high density plane. The system is unstable.

2D homogeneous dipolar gases

In the previous section a phononic instability due to a non balanced head-to-tail configuration has been shown. It is then natural to study the case of a system confined along the z axis and homogeneous in the perpendicular plane, formally $\mu = n_0(g + g_{dd}) \ll \hbar\omega_z$. In such a 2D configuration the z wave function is given by the ground state of an harmonic oscillator and the density takes the form $n(r) = n(\rho)\frac{1}{\sigma_z\sqrt{\pi}}e^{-\frac{z^2}{2\sigma_z^2}}$ where $\sqrt{2}\sigma_z = l_z$ is the z trap dimension. The dispersion curve is thus obtained as the 3D case integrating over the z direction. It results

$$E(q_\perp) = \hbar\omega(q_\perp) = \sqrt{\left(\frac{\hbar^2 q_\perp^2}{2m}\right)^2 + \frac{\hbar^2 q_\perp^2}{2m} 2n_0\left(g + g_{dd}H_{2D}(\frac{q_\perp\sigma_z}{\sqrt{2}})\right)} \tag{1.69}$$

where $H_{2D}(x) = 1 - \frac{3\sqrt{\pi}}{2}|x|\mathrm{erfc}(x)e^{x^2}$, $\mathrm{erfc}(x)$ being the complementary error function. The trend of H_{2D} is reported in Fig. 1.19. The fundamental difference between the 3D and 2D case is that the dipolar dependence of the dispersion curve is no longer a $\cos^2(\theta)$, but it is related on the absolute value of the quasi-momentum $q_\perp$. In particular from Fig. 1.19 a turning point is recognizable for $q_\perp l_z = 1$. For smaller values the contribution is repulsive, afterwords attractive.

The phonon stability condition in this regime is $g + 2g_{dd} > 0$, but also a new kind of instability arises because of the suddenly attractive nature of DDI. This change of sign induces in the dispersion curve a new minimum, called *roton* in analogy with the superfluid He case. When the roton energy falls to zero a *rotonic instability* is realized. Such instability is, however, formally obtained in an *effective 3D* system. The *quasi-2D* system, considered in this section, is stable for pure dipolar gases even for $\epsilon_{\mathrm{dd}} \gg 1$ as the condition $\mu \ll \hbar\omega_z$ prevents softening of phonon modes propagating along the dipole direction. For the sake of completeness also the attractive contact case is mentioned. In this latter case even in quasi-2D configuration a non zero momentum minimum can occur, called 'roton' for analogy, because of the DDI momentum dependent balancing of the attractive contact force.

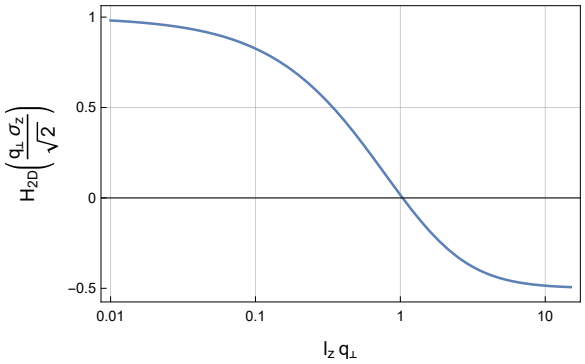

Figure 1.19: H_{2D}. Function characterizing the dipolar contribution in the dispersion law. The important feature is that it is momentum dependent and for a critical value is has a zero value, changing the sign of the contribution from repulsive to attractive.

Trapped dipolar gases in Thomas-Fermi regime

The time dependent Gross-Pitaevskii equation for dipolar gases is obtained by the Eq. 1.33 plus the dipole term in Eq. 1.59. It results

$$i\hbar\partial_t\psi(r,t) = (-\frac{\hbar^2\nabla^2}{2m} + V_{ext} + U_{int}(r))\psi(r,t) \tag{1.70}$$

where $U_{int} = \Phi_{cont}(r) + \Phi_{dip}(r) = gn(r) + \int |\psi(r',t)|^2 U_{dd}(r-r')d^3r'$. It is a non-local G-P equation (NLGPE) because of the DDI term. The stationary equation is the

$$\mu\psi(r) = (-\frac{\hbar^2\nabla^2}{2m} + V_{ext} + gn(r) + \Phi_{dip}(r))\psi(r) \tag{1.71}$$

This has been exactly resolved for a cylindrical trap [3]

$$V_{ext}(\rho,z) = \frac{m}{2}(\omega_\rho\rho^2 + \omega_z z^2) \tag{1.72}$$

where $\rho^2 = x^2 + y^2$. Here the trap aspect ratio is also defined as $\gamma = \omega_z/\omega_\rho$ as well as the condensate aspect ratio $\kappa = R_\rho/R_z$, where R_ρ and R_z are the Thomas-Fermi radii in the horizontal plane and polarization axis respectively. The main features, all coupled with each other, are here presented:

- the density profile is still an inverted parabola $n(r) = n_0\left(1 - \frac{\rho^2}{R_x^2} - \frac{z^2}{R_z^2}\right)$ with $n(r) \geq 0$, where $n_0 = \frac{15N}{R_x^2 R_z 8\pi}$. The aspect ratio however is no longer equal to that of the trap like in the case of contact interactions.

- the chemical potential is $\mu = gn_0(1 - \epsilon_{dd}f_{dip}(\kappa))$ where $f_{dip}(\kappa)$ is a geometrical factor. If all other things are equal the effect of the DDI is to lower(raise) μ (which is proportional to the mean-field energy per particle) of a prolate, $\kappa < 1$ (oblate, $(\kappa > 1)$) condensate. A dipolar condensate tends to elongate along the polarization axes, see Fig. 1.20. Such an elongation is called *magnetostriction*.

- the Thomas-Fermi radii are $R_x = R_y = \left[\frac{15gN\kappa}{4\pi m\omega_x^2}\left\{1 + \epsilon_{dd}\left(\frac{3\kappa^2 f_{dip}(\kappa)}{2(1-\kappa^2)} - 1\right)\right\}\right]^{\frac{1}{5}}$. In particular while the contact T-F radii in the three directions were independent, because the contact interaction depends only on local properties, the dipolar T-F radii are coupled with each other because of the nature of the interaction.

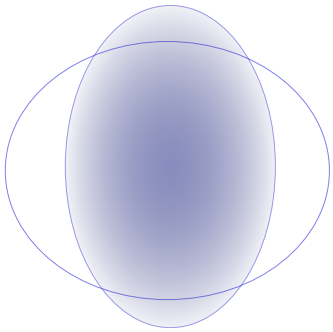

Figure 1.20: Representation of the magnetostiction. The dipolar condensate is the full oval while the empty oval is an equipotential line of the trap. The polarization direction is vertical in the figure.

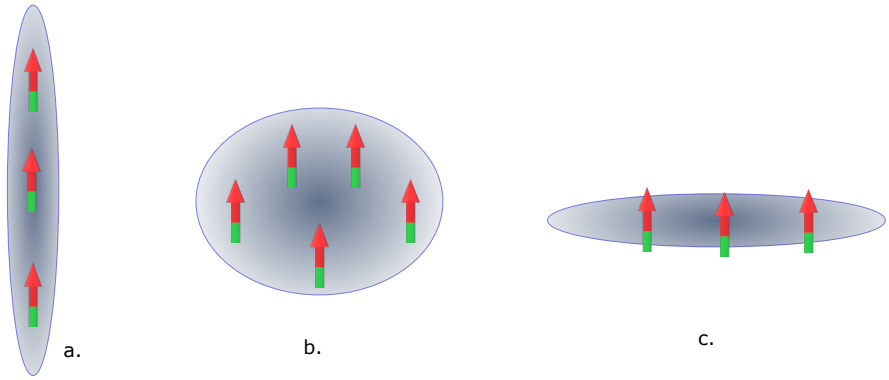

Figure 1.21: In panel **a**. a prolate trap is represented. In panel **b**. a trap with $\gamma \sim 1$. In panel **c**. an oblate trap.

- The aspect ratio κ is determined by solving a trascendental equation

$$3\kappa^2\epsilon_{dd}\left[\left(\frac{\gamma^2}{2}+1\right)\frac{f_{dip}(\kappa)}{1-\kappa^2}-1\right]+(\epsilon_{dd}-1)(\kappa^2-\gamma^2)=0 \tag{1.73}$$

  which leads to a stability diagram. For $\epsilon_{dd}<1$ the condensate is always stable, for $\epsilon_{dd}>1$ (DDI dominant regime) a stability threshold is identified. Below this threshold the gas is unstable. The minimum in the presence of attractive forces is said to be metastable, in the sense that this corresponds to a local minimum subject to a critical existence value.

The unstable nature of a dipolar gas depends critically on the interplay between these factor: γ, ϵ_{dd}, U_{dd} and N, atom number. Since a trapped condensate is now considered, instead of phonon and roton the instability is studied in terms of trap modes. The main modes in a traps are 3: a *breathing* mode (frequency $\omega_{\rm bm}$) and two quadrupole ones, all represented in Fig. 1.22. The phononic collapse of a contact condensate is due to $\omega_{\rm bm}\to 0$. In the case of a dipolar gas the instability is essentially determined by the trap. A summary is here proposed

- $\gamma \ll 1$, prolate trap (see Fig. 1.21a.).
  DDI are meanly attractive, $U_{dd}<0$. It is a metastable condensate for $N<N_c$, then it collapses because of the breathing mode, as in the contact case.

- $\gamma \leq 1$, slightly prolate/symmetric trap (see fig. 1.21b.).
  DDI are repulsive in the plane perpendicular to the polarization axes, but still have the possibility of the head-to-tail configuration along that axes. The zero frequency mode

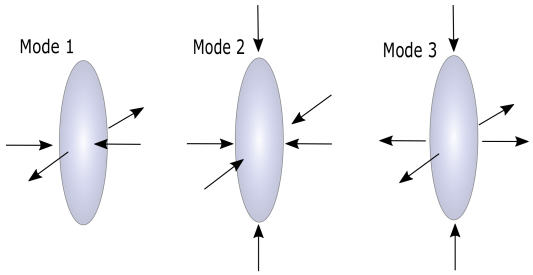

Figure 1.22: Modes in a trap. First and third mode are quadrupole modes while the second one is called 'breathing mode'.

leading to instability is a superposition of a breathing mode and a quadrupole one, evolving to quadrupole mode as $\gamma = 1$ is approached.

- $\gamma > 1$, oblate trap (see fig. 1.21c.). A further splitting into soft pancake traps and hard pancake traps is done. Soft pancakes aspect ratio tends to the trap aspect ratio as the instability threshold N_c is reached. The collapse is due to a quadrupole mode softening. In that case the excitation consists of a radial nodal pattern, thus the instability is due to a modulation of the condensate density in the radial direction. It is analogous to the roton instability studied for an infinite-pancake [25] and is called "radial roton" instability. Hard pancake traps lead to a particularly interesting physics. Besides the 'normal' solution of an inverted parabola also a new stable configuration has been found consisting in a biconcave shape [19]. The maximum density in this configuration is not in the centre of the trap. Increasing the number of particles a collapse is observed due to the modulation in the angular coordinate, cylindrical symmetry is spontaneously broken. The instability may be described as a buckling along the high density ring. It is referred to as a 'angular roton'. Two possible roton instabilities are thus possible in an hard pancake configuration: a 'radial' roton and an 'angular' roton.

In conclusion, for each finite value of γ, the condensate decays if a sufficiently large number of dipoles are added. In general, however, the more pancake like the trap is ($\gamma \gg 1$), the more dipoles are required to make the condensate unstable.

1.4.4 Experimental observation

Here we give a brief review of recent experiments related to the theory presented in previous sections. We report on the observation of a roton mode in a BEC of Er atoms (see Ref. [26]) and on the d-wave symmetry collapse of a BEC of Cr atoms (see Ref. [21]).

Observation of a roton mode

The first observation of a roton mode is shown in Fig. 1.23. The experiment consists in a dipolar condensate of Er atoms trapped in a cigar-shaped trap, see Fig.1.24 The idea of the experiment is to use the roton gap dependence on n, density of the system, contained in the chemical potential μ and ϵ_{dd}, interaction strength shown in Eq. 1.66. The roton minimum gets deeper as ϵ_{dd} is increased, thus the scattering length is lowered. When $\Delta = 0$ the population with $q_y = 0$ exponentially transfers to $\pm q_{\rm rot}$ and the mode becomes visible in the momentum space. The growth rate Γ is related to the roton energy gap by the relation

$$\Gamma \propto Im[\Delta]/\hbar \tag{1.74}$$

Thus measuring the growth rate an estimation of the roton gap can be made. In the experiment a roton mode growing in ~ 1 ms was observed in the momentum space, see Fig. 1.23. The geometric

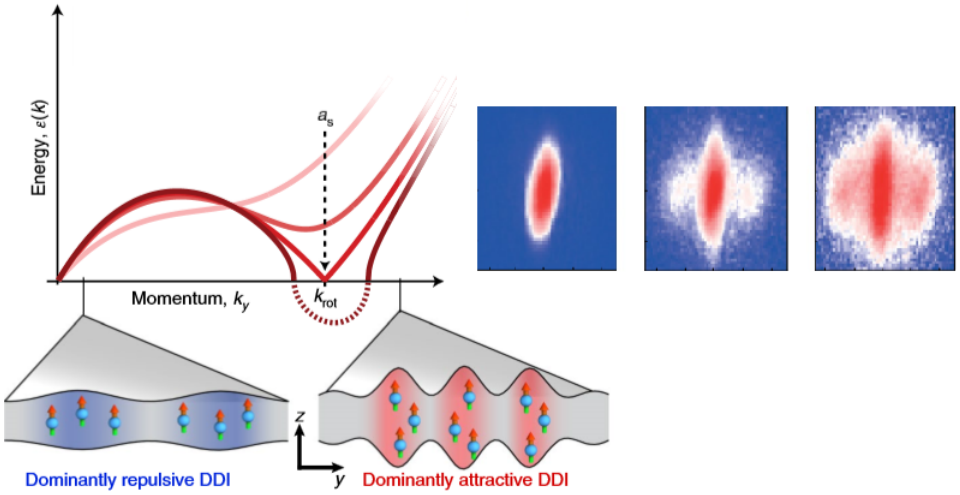

Figure 1.23: Adapted from [26]. Excitation spectrum of a dipolar ultra cold gas. Different dipole configurations lead to the phonon (low momenta) and roton (finite momentum) density modulation. Observation of the system for different value of a_s are then reported to give an idea of the appearance of a roton, as side bands in the momentum space (shown in the top sight panel). The experimental observation of a roton mode is reported on the right.

scaling of $q_{\rm rot}$ according to Eq. 1.66 was confirmed. The population growth was obtained by a three gaussian fit measuring the relative hight of central (A_0) and side (A_1) peaks. After ~ 1 ms the population saturates at about $A_1/A_0 = 0.3$ and lasts for about 3 ms. The results of that experiment are however limited by the short life-time of the system. Because of the magnetic moment of Er being relatively weak $\mu \sim 7\mu_B$ the DDI dominant regime is reached going to high density, meaning heavy three-body losses.

d-wave collapse

The collapse dynamics of a dipolar BEC has been experimentally studied by a group of Stuttgart [21]. The experiment employs Cr atoms which have a magnetic moment $\mu \sim 6\mu_B$. First stage of collapse is a compression of the system. Because of the attractive interactions the atomic density increases and a high density region is realized in the centre of the trap. This region suffers heavy three-body losses. Because of these losses the centripetal force diminishes and the quantum pressure due to the indetermination principle pushes the atoms far from each other. An expansion with a 'burst' of atoms then happens. Unlike the contact case this expansion is not isotropic. It reminds the d-symmetry of the dipolar interaction.

Such collapse dynamics was studied also for Dy atoms. In this latter case however, experimental observations varied from the behaviour described above. Self bound structures were observed, leading to a new kind of quantum state, namely a 'Quantum Droplet'. This new physics and further implications are discussed in the next section.

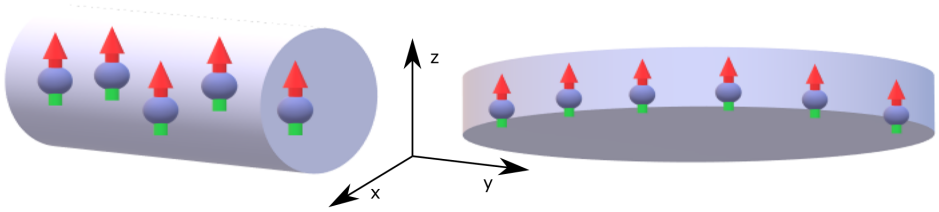

Figure 1.24: On the left a cigar-shape like trap is reported. It is a 1D system because dipoles can interact with each other only in the y direction. On the right a pancake-like trap is sketched. Here the dipoles feel each other in all the $x-y$ plane; it can then be considered as a 2D system.

1.5 Beyond Mean-field effects

Beyond mean field (BMF) effects have been widely studied in theoretical terms for a very long time. Such effects arise from the inclusion of the main contribution, excluded in the mean-field treatment, of quantum fluctuations. This phenomenon is briefly discussed then, in the next section an example of a new quantum state stabilized by the presence of BMF term is given.

1.5.1 Quantum fluctuations

Quantum fluctuations are the energy fluctuations of vacuum arising from the Heisenberg uncertainty principle. These fluctuations translate into a spatial uncertainty, i.e. the particles can't be thought as a classical spot, but more as a cloud. Such a 'quantum extension' is equivalent to a quantum pressure that prevent the particles to overlap. It is as important as the equilibrium relative distance between atoms becomes smaller due to other forces in the system. So it can be considered as an effective short-range repulsive interaction [27].

In Sec. 1.3.1 the Bogoliubov approximation was introduced. It consists in writing $\psi = \psi_0 + \delta\psi$, where $\delta\psi$ accounts for quantum fluctuations. The perturbative term $\delta\psi$ can be written in terms of boson creation and annihilation operators $\delta\psi = \sum_i U\hat{b}_i + V\hat{b}_i^\dagger$, where U and V are the Bogoliubov amplitudes. Assuming the mean-field ground state as the effective ground state, a perturbative excited condensate can be treated as a quasi-particle gas were the energy is given by the energy of each excitation plus a vacuum energy intended as the one where no excitations are present [35]

$$\hat{H} = \sum_p \epsilon_p \hat{b}_p \hat{b}_p^\dagger + E_0 \qquad . \tag{1.75}$$

The energy has the property that for a given value of the chemical potential μ is stationary for $\psi = \psi_0$. Linear terms in $\delta\psi$ then vanish and the lowest excitation energy term is quadratic in $\delta\psi$. This quadratic dependence together with the commutation rule $[\hat{b}_i, \hat{b}_j^\dagger] = \delta_{ij}$ implies a contribution to the vacuum state of a constant term accounting for quantum correlation [7]. In this formalism the BMF correction is then due to the zero-point motion of the collective modes of the condensate.

A pioneering work on this subject is the one of Lee, Huang and Yang, which dates back to 1957 [47]. There calculation of the correction term to the ground state energy arising from quantum fluctuations was done in the case of a gas with purely contact interactions. An extension to dipolar quantum gases was obtained by Lima and Pelster [27] within the local-density approximation for

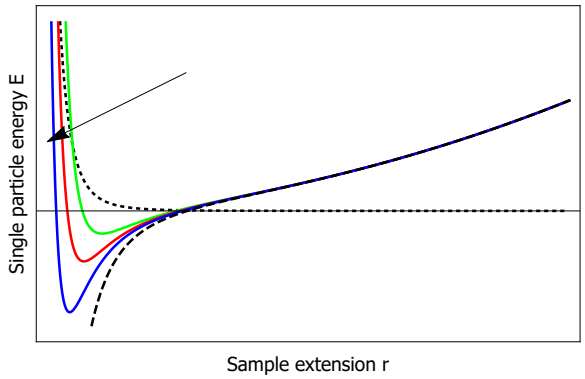

Figure 1.25: Beyond mean field correction of the energy due to quantum fluctuations. Mean field energy is reported in dashed line, dotted line represents the quantum fluctuation contribution for the same a_s. The sum is shown tuning a_s to lower value following the arrow in figure. If a_s is close enough to a_c a confining potential arises. Energy grows at large r because of trapping.

a trapped inhomogeneous gas in the Thomas-Fermi regime. The correction term due to quantum fluctuations is $g_{qf} = \frac{32ga_s^{\frac{3}{2}}}{3\sqrt{\pi}}\left(1 + \frac{3a_{dd}^2}{2a_s^2}\right)$ and the extended GPE (eGPE) is:

$$i\hbar\frac{\partial}{\partial t}\psi_0(r,t) = \Big(-\frac{\hbar^2}{2m}\nabla^2 + V_{ext} + g|\psi_0|^2 + \Phi_{dip}(r) + g_{qf}|\psi|^3\Big)\psi_0(r,t) \tag{1.76}$$

The correction to the ground state energy obtained is

$$\frac{E_{BMF}(r)}{V} = \frac{2\pi\hbar^2 a_s n^2}{M}\frac{128}{15}F_5(\epsilon_{dd})\sqrt{\frac{n(r)a_s^3}{\pi}} \propto n^{5/2} \tag{1.77}$$

with the auxiliary function $F_5(\epsilon_{dd})$ describing the dipolar enhancement of the correction[7]. It varies from $F_5(0) = 1$ up to $F_5(1) \sim 2.60$ so that the effect of the quantum fluctuations is more significant for strongly dipolar system. By differentiating the energy correction with respect to the particle number the BMF equation of state is obtained

$$\mu = \frac{n4\pi\hbar^2 a_s}{M}[1 + \epsilon_{dd}(3cos^2(\theta) - 1)] + \frac{32gn}{3}\sqrt{\frac{a_s^3 n}{\pi}}F_5(\epsilon_{dd}) \tag{1.78}$$

Quantum fluctuations represent a short range stabilizing repulsive term as shown in Fig. 1.25. The BMF term due to quantum fluctuations for a particular value of a_s is represented as a dotted line, while the mean-field energy per particle as a dashed line. The sum of the two contributions is reported for different values of a_s.

As a_s diminishes, the sum takes the form of a confining potential. If a_s is small enough then a self-bound state exists which survives also without the trapping potential, that is the quadratic dominant term for high values of r.

1.5.2 Quantum droplets

In the previous section quantum fluctuations were introduced. They can play a stabilization role as they represent a short-range repulsive interaction. In this section a quantum fluctuations stabilized phenomenon is discussed: the quantum droplet. A quantum droplet is a high density case of quantum gas. The bridge between quantum droplet and BEC is here given following Ref. [49].

[7]The function $F_5(\epsilon_{dd})$ is a complex function. In the interesting limit $\epsilon \lesssim 1$ the imaginary part can be neglected. Furthermore, in this limit, $F_5(\epsilon_{dd})$ can be approximated with its lowest order $\sim 1 + 3\epsilon_{\rm dd}^2/2$ [48].

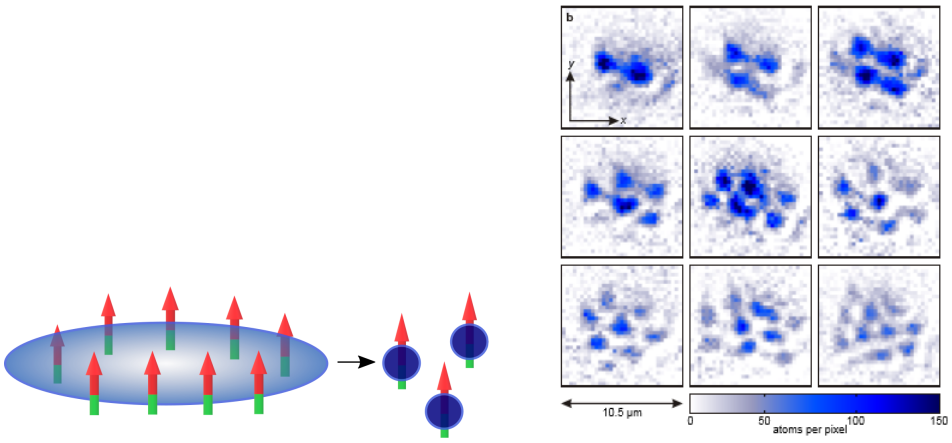

(a) (b)

Figure 1.26: **a**. Example of droplets formation starting from an oblate trap. **b**. Single-shot in situ images of droplet patterns. Image taken from [29].

We already stated that by adding the quantum fluctuations term in the G-P equation is analogous to introduce another repulsive term. Studying the instability of the system, it is found to depend on the value γ of the trap ratio. In particular two different behaviours are shown for γ below or above a critical value γ_c. For $\gamma > \gamma_c$ a bistability region appears where condensate and quantum droplets coexist. Here the transition from one phase to another is a first order transition according to the Ehrenfest classification[8]. This mechanism can lead to the formation of several droplets. For $\gamma < \gamma_c$ the bistability region disappears and the first order transition becomes a continuous crossover very similar to the transition between gas and liquid. This mechanism results in a unique macroscopic droplet.

This dependence on the trap ratio is because the quantum droplets are characterized by two different trends. On the one hand they have liquid-like behaviour so they have low compressibility while preserving the peak density. On the other hand the binding mechanism is very different from the one of a classical droplet since it relies on the attractive nature of the DDI, thus on an anisotropic density distribution. When compressing, the interplay between these two phenomena determine the ground state. For a sufficiently elongated trap along the polarization axis the ground state is a single droplet, however when the system is strongly confined the ground state becomes an array of droplets [30].

The observation of quantum droplets for $\gamma > \gamma_c$ is described in [28, 29] and is here briefly recalled. The experiment is done with ^{164}Dy. A condensate dominated by dipolar interactions is obtained by tuning the scattering length close to the critical value of the scattering length a_{crit}. An angular roton instability leading to a periodic perturbation of the atomic density distribution was expected. A finite-wavelength instability was instead observed. It triggers a transition to ordered states consisting in multiple tiny droplets arranged in a triangular pattern, see Fig. 1.26b. It is very similar to a Rosensweig instability happening in a classical ferrofluid. Because of the similarity between quantum droplets and Rosensweig instability this last phenomenon is briefly recalled from [46], in the end of the section. The main difference between the classical and quantum phenomena is that quantum ferrofluids are fully spin polarized so the dipolar interaction is independent of the B strength[9].

[8] Writing for example the pressure as a function of the fugacity $z = e^{\mu/(k_B T)}$ if its derivative is discontinuous for $z = z_c$ then the transition is of the first species. If the first derivative is continuous in z_c while the second is discontinuous, then the transition is of second species. And so on.

[9] Quantum ferrofluids are in the ultracold regime. Since the magnetic constituents are fully spin polarized for Zeeman energy $\mu_B B \geq k_B T$ thermal energy, ultra-cold systems are always fully spin polarized.

We now discuss the key properties of the quantum droplets:

1. *Stabilization mechanism.* Quantum droplets are stabilized by quantum fluctuations [28]. Experimental demonstrations consist of measurements of the central peak density n_0 value and the decay time τ. Apart from quantum fluctuations, another stabilization mechanism was proposed. It is due to the real part of three-body interactions, where such a term describes a three body scattering [50]. The expression for the density peak n_0 is reported in the two cases, accounting for quantum fluctuations or three-body interactions. The mechanical condition for equilibrium is $\frac{\partial \mu}{\partial n} \geq 0$. If μ is the one in Eq. 1.78, thus accounting for quantum fluctuations, then

$$n_0 = \frac{\pi}{a_s^3}\Big(\frac{\epsilon_{dd} f_{dip}(\kappa) - 1}{16(1 + 3\epsilon_{dd}^2/2)}\Big)^2 \sim 10^{20}\mathrm{m}^{-3} \tag{1.79}$$

   It depends only on a_s and κ, therefore it is independent of atom number. This is characteristic of a liquid-like state. If a three-body contribution is considered, instead of quantum fluctuations, it results $n_0 \sim 17 \times 10^{20} m^{-3}$. Experimentally a density $n_0^{exp} \sim 5 \times 20^{20} m^{-3}$ was found, in agreement with a quantum fluctuations stabilization mechanism [28]. Further proof is the scaling behaviour of τ with a_s, in accordance to the one expected considering quantum fluctuations [28].
   In Fig. 1.25 it was shown the appearance of a confining potential due to quantum fluctuations. Such potential leads to a self-bound state surviving even in the absence of the trap. Such a system consists, then, of quantum droplets.

2. *Relative distances and expansion.* The expansion of quantum droplets has been studied in a wave guide perpendicular to the dipole direction [48]. The experiment purpose was to verify that quantum droplets are effectively self bound and that the confinement is not due to a repulsion between them. The droplets were observed to move away from each other, but keeping their size. A several hundred of ms lifetime was observed. This experiment demonstrates that the mechanism ensuring droplet stability takes place locally, within individual droplets. The stability of droplets, then, is not due to any long-range effect between them.
   Such long-range effect, however, combined with the trap potential, determines the relative distance between droplets. Droplets, in fact, repeal each other with the DDI (see Fig. 1.26a), but are constrained by the trap. The competition between these two terms fixes the typical distance between droplets. Using a point-like model for a droplet, a typical distance of ~ 4.5 μm was found. However, an experimentally typical distance of $d = 2.5(5)$ μm was measured [28]. By a gaussian model for the droplet density, it is found that the droplet is elongated along the dipole axis. Such elongation decreases the effective magnetic moment of the droplets. Distances in accordance with experimental data were found [28].

3. *Coherence.* The coherence of an array of droplets was studied in Ref. [30]. In the experiment tilted dipoles are used to tune the DDI for different geometries. The control on the droplet number is achieved, using these tilted dipoles. Droplets are recognized as a long-lived density-modulated metastable state separated from the ground state by an energy barrier. Furthermore, through the use of absorption imaging, the droplet interference pattern is studied. Such a pattern shows a random phase distribution. Quantum droplets are, thus, incoherent.

The study on the ground state of a quantum fluctuation stabilized BEC as well as on the coherence properties of an array of droplets are of particular interest as they are related to a new state of matter: supersolidity [31]. A supersolid is a self-organized density-modulated state, very similar to a a crystal lattice, that however maintains superfluid properties. Quantum systems showing supersolid properties have been observed in double cavities with superimposed optical lattice or in systems with spin-orbit coupled [12, 51]. This supersolid-like phase is somewhat 'artificial' as

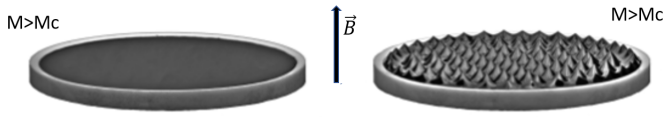

Figure 1.27: adapted from [53]. On the left a ferrofluid in its stable phase, on the right a ferrofluid undergoing a normal-field instability.

the density modulation is imprinted by an external light field. Dipolar Bose gases on the contrary own a natural length scale for self organization of the system given by the roton minimum. By numerical simulations of the eGPE a 'striped phase' featuring multiple droplets is found to be the ground state of the system [30]. The experimental observation, however, of an incoherent metastable state makes a supersolid state still elusive to observation in dipolar systems.

Rosensweig instability

Fluids under the influence of gravity tend to have a plane surface. If an external magnetic field is introduced it can destabilize the interface between the magnetic fluid and the non-magnetic medium [52]. Surface waves are induced by B_{ext} and modify the magnetic field at the interface, inside and outside the fluid. In particular B_{int} is focused at the wave crests. If B_{ext} exceeds a critical value a static ordered pattern forms spontaneously. This phenomenon is called normal-field or Rosensweig instability. The dispersion relation of a surface wave in ferrofluids is here reported for completeness:

$$\rho\omega^2 = \rho g q + \sigma_{\text{s}} q^3 - \frac{q^2 \mu_0 \mu_{\text{r}} M^2}{1 + \mu_{\text{r}}} \tag{1.80}$$

where ρ is the fluid density, g the gravity acceleration, σ_{s} the surface density, M the magnetization associated to B_{ext} and μ_{r} the permettivity of the medium. The first term on the right represents gravitation-induced waves and is dominant for small q. The second term represents *capillary* waves that are characterized by a surface tension dominated dynamics, these are important for big q. The third term is important for intermediate q when a magnetic field is present and describes the concentration of B at the peaks of a surface disturbance. The critical field B_{c} corresponds to the critical magnetization M_{c} for which ω becomes imaginary, i.e. the internal dipolar interaction exceeds all other fluid forces. This instability is characterized by the transition from a flat surface to surface spikes [53] (see Fig. 1.27).

The magnetic response of a ferrofluid also includes a deformation of its surface. In the absence of any external force the surface energy is minimized by the smallest surface area, a spherical magnetic fluid drop is then the optimal configuration. A spherical drop on a superhydrophobic substrate is considered. If any uniform and homogeneous external field is applied the magnetic forces counteract the surface tension deforming the drop into a prolate spheroid. If a magnetic gradient is included after the elongation the drop splits into drop patterns showing a static self-assembly of ferrofluid drops into ordered structures with mainly triangular symmetry [54]. This droplet pattern is irreversible because of a repulsion between drops and the superhydrophobic nature of the substrate ensuring that the drops are not physically connected.

Chapter 2

Obtaining a dipolar Bose Einstein condensate

In this chapter the ingredients of our experiment are presented. The first section is dedicated to Dysprosium. A survey of light-matter interaction theory and experimental methods are then briefly presented. The experimental apparatus and imaging system are then described. Finally I give the proof that a Bose-Einstein condensate of Dy has been obtained.

2.1 Dysprosium

The element Dysprosium (see Fig. 2.2) belongs to the group of the lanthanides, see the periodic table of elements in Fig. 2.1.

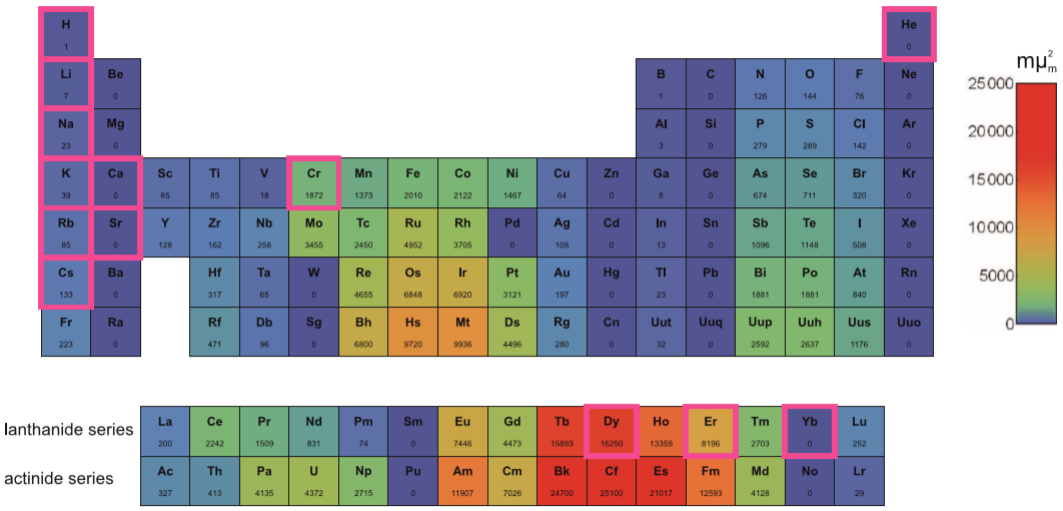

Figure 2.1: **Periodic table of elements**: pink borders highlight the elements that have been condensed; the element colours vary on a scale where blue represents the elements whit the lowest dipolar character, and red the elements with the highest one. Image taken from [55].

Dy was first discovered in 1878 by the Swiss chemist Marc Delafontaine and called "Philippia", however it was then thought to be a mixture of Tb and Yb. It was the French chemist Paul-Emile

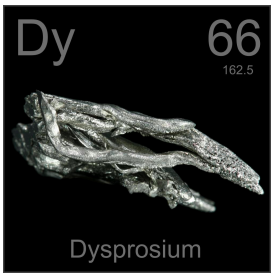

Figure 2.2: Appearance of the element Dysprosium at room temperature. The atomic number of the element is 66, while the atomic weight 162.5u. Image taken from http://periodictable.com/Items/066.2/index.html.

Isotope	**mass [a.u.]**	**abundance[%]**	**Statistics**
^{156}Dy	155.92	0.06	boson
^{157}Dy	157.92	0.1	fermion
^{160}Dy	159.93	2.33	boson
^{161}Dy	160.93	18.9	fermion
^{162}Dy	161.93	25.45	boson
^{163}Dy	162.93	24.9	fermion
^{164}Dy	163.93	28.26	boson

Table 2.1: Natural abundance and statistics of Dy isotopes [56].

Lecoq de Boisbaudron who in 1886 found it in a holmium sample and recognised it as a new element. He called it "Dysprosium" from the Greek expression "Dysprositos", which meaning "hard to get at", reflecting the difficulty to isolate it from holmium [56, 57]. Dy was efficiently separated in pure form in the 1950s with the development of ion-exchange chromatography, by Frank Spedding [58].

Chemical properties

The atomic number of Dysprosium is 66, the melting point 1412°C and boiling point 2560°C. It has seven stable isotopes, whose abundances are listed in Table 2.1. This work deals with the bosonic isotopes, above all ^{162}Dy used in our experiments, but also ^{164}Dy that is used in other laboratories. Quantum degeneracy, however, has been reached also for the fermionic isotopes allowing the study of a dipolar Fermi gas [59]. The Dy electronic configuration is:

$$(1s^2 2s^2 2p^6 3s^2 3p^6 3d^{10} 4s^2 4p^6 4d^{10} 5s^2 5p^6) 4f^{10} 6s^2 = [Xe] 4f^{10} 6s^2 \tag{2.1}$$

which is a submerged-shell configuration. In fact, while the $6s$ orbital is completely filled, the lower energy $4f$ is not. As a result of this configuration, excited states can be reached in many different ways, with electron transitions starting from both the f and the s shell. Therefore, the atomic energy level structure is quite complex. A partial scheme is reported in Fig. 2.3 highlighting the useful transitions for laser cooling and trapping. The broad blue transition at 421 nm with linewidth $\Gamma_{421} = 2\pi \times 32.2$ MHz is used to first slow down the atoms coming out of the oven. Because of the high melting point, in fact, Dysprosium atoms spread out of the oven with a high thermal speed, of the order of ~ 400 m/s, so a Zeeman Slower (ZS) and a Transverse Cooling (TC) are necessary before trapping the atoms in a Magneto Optical Trap (MOT). The use of a broad resonance allows the fast scattering of photons, so this transition is suitable not only to slow atoms, but also for an imaging system. The narrower red transition with linewidth $\Gamma_{626} = 2\pi \times 136$ kHz is instead used for the MOT.

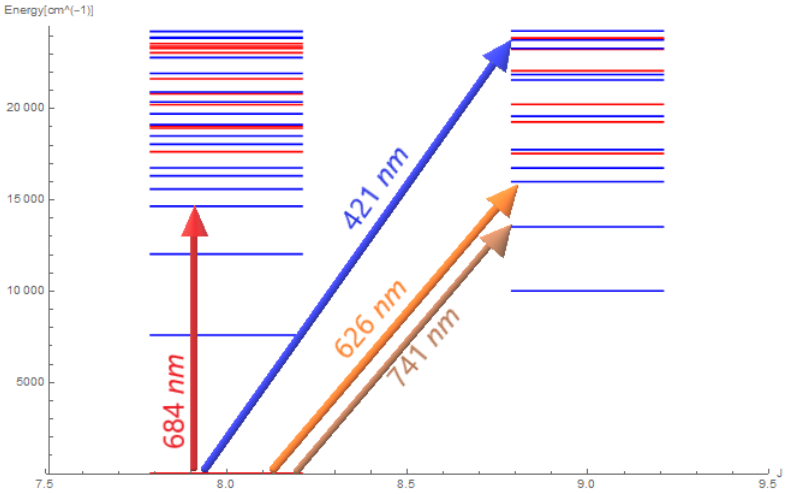

Figure 2.3: Part of the level scheme of Dy, drawn using the data in Ref. [60]. Red lines indicate states with even parity, blue lines the odd ones.

m_l	-3	-2	-1	0	1	2	3	
Dy $4f^{10}$	↑↓	↑↓	↑↓	↑	↑	↑	↑	S= 4×1/2 = 2

Table 2.2: **Maximum spin state**. The equivalent electrons of the 4f shell, have seven substates available (m_J= -3,...,+3). Substates have to be filled in order to have the maximum spin state. This results in three states fully occupied, and four with only one electron.

Starting from the electron configuration in Eq. 2.1, using Hund's rules the Dy ground state can be constructed, as shown in Table 2.2.

- The ground-state quantum numbers are only determined by *equivalent electrons*, the ones belonging to an open shell. So only the 4f-electrons have to be considered.
- The ground-state is the maximum spin state, it has the maximum spin symmetry so the maximum orbital-antisymmetry. This configuration minimizes Coulomb repulsion and so the atom energy.
- The ground-state is the one for which the angular momentum **L** is maximized. So the unpaired spins shown in Table 2.2 occupy the states $m_l = 0, +1, +2, +3$, L = 6.
- The ground-state, for a more (less-equal) than a half filled outermost sub-shell, is the one that maximizes (minimizes) the spin-orbit coupling number **J** = **L**+**S**, J = 8.

The resulting Dy ground state is: $^5I_8$. The bosonic isotopes have null nuclear spin **I**, i.e. I=0, so they show no hyperfine structure. On the contrary the fermionic ones have I = 5/2. Isotopes shift in Dy has been measured by laser spectroscopy, shown in Fig. 2.4, the hyperfine structure is also visible.

Why Dysprosium

This peculiar element was chosen for the experiment because it is the element with the strongest permanent magnetic moment $\mu = 9.93\mu_B$. The effects of the simultaneous presence of two competing inter-particle interactions, were reported. We employ Dysprosium in order to enhance such effects, thanks to its strong dipolar nature. Furthermore, because of its electronic configuration, Dy has a dense distribution of Feshbach resonances. This characteristic make the inter-particle

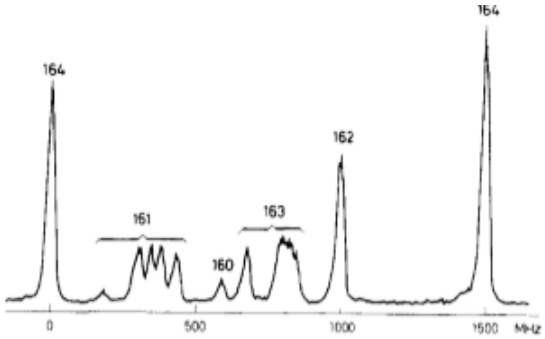

Figure 2.4: Spectroscopy of the Dy transition using a pulsed dye laser: the different isotopes and hyperfine structure are evident. Figure taken from Ref. [61]

interactions highly tunable, allowing the study of different interaction regime. Moreover the Dy has a reach variety of isotopes, both bosonic and fermionic. It opens the possibility of mixtures. New phenomena in dipolar many body-body system have been studied, but still new and interesting physics is possible with the rare-earth Dy.

2.2 Theoretical background and experimental methods

2.2.1 Light-Matter Interaction

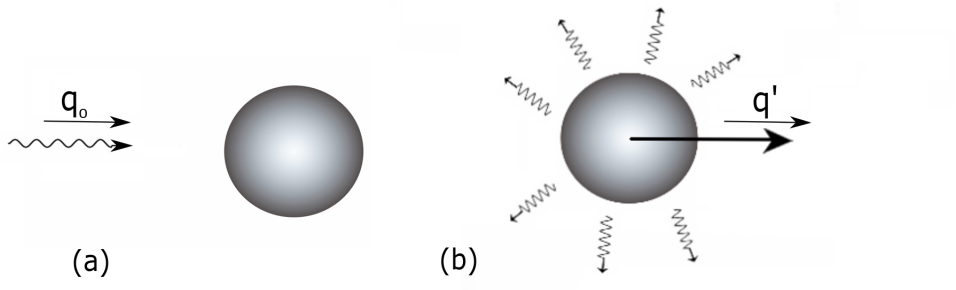

Figure 2.5: Cartoon of the absorption (**a**) and radiation pressure (**b**). When a lot of photons impinges on an atom, they are absorbed and then spontaneously emitted. The average effect of this emission is a momentum, acquired by the atom, in the direction of the incoming photons. It is equivalent to a pressure.

Here the light-matter interaction theory it is briefly considered, following Ref. [62, 63]. The system we describe is sketched in Fig. 2.5. A *two level approximation* is used, i.e. the atom is described as a two-level system where only closed cycle transitions are possible: each photon absorption is always followed by spontaneous decay to the initial state. In this framework, the light-matter interaction summarizes in two forces acting on the atom: the scattering force and the dipole force. Intuitively these forces correspond to phenomena of absorption/spontaneous emission and refracting of light.

Scattering force

The scattering force equals the rate at which an object gains momentum as it absorbs radiation. It arises in case of resonant radiation, i.e. the energy of incident photons $\hbar\omega_0$ is equal to the gap between the two levels $\hbar\omega_{01}$: $\omega_0 = \omega_{01}$. The process is sketched in Fig. 2.6.

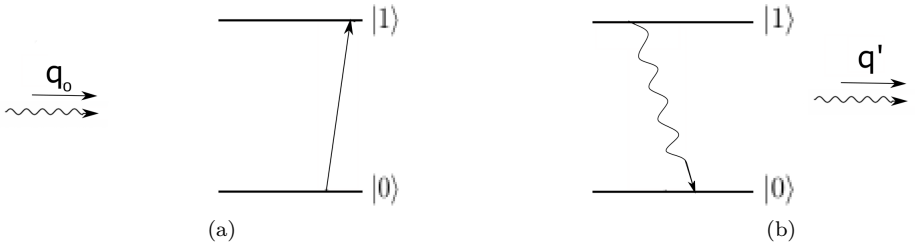

Figure 2.6: Two level scheme of the atom. Absorption is represented in panel (**a**) while spontaneous emission in panel (**b**).

This process preserves the energy E and momentum $p = \hbar q$ of the system, so that if the photon is spontaneously emitted with an angle $\theta \neq 0$, the atom has to get a velocity v' to preserve the momentum along the direction of light propagation. If a lots of photons, with momentum $\hbar q_0$, impinge on the atom, as the spontaneous emission is isotropic, the net effect is that the atom acquires a momentum $\hbar q' = \hbar q_0$ in the direction of the incoming beam. This phenomenon is called Radiation Pressure and is sketched in Fig. 2.5(b). This quantum effect can be described as a scattering force between the beam and the atom:

$$F = \frac{\Delta p}{\Delta t} = \hbar q_0 R_{scatt} \tag{2.2}$$

where R_{scatt} is the scattering rate, i.e. number of photons absorbed per unit time. In a closed channel:

$$R_{scatt} = \sum_j P_{j\leftarrow i}(f(i) - f(j)) \tag{2.3}$$

where $i(j)$ is the initial (final) state, $f(l)$ the occupation probability of the l^{th} level and $P_{j\leftarrow i}$ the probability to have the transition from state i to j, given by the Fermi golden rule:

$$P_{j\leftarrow i} = \frac{2\pi}{\hbar} |\langle j| H_{int} |i\rangle|^2 \delta(E_j - E_i)\rho_j \tag{2.4}$$

where ρ_j is the density of final states and $H_{\rm int}$ describes the interaction. For a laser with intensity I, frequency ω_0, detuning $\delta = \omega_0 - \omega_{01}$ and an atomic transition with life time $\tau = \frac{1}{\Gamma}$ (Γ the natural linewidth), the scattering rate is:

$$R_{scatt} = \frac{\Gamma}{2} \frac{\frac{I}{I_{sat}}}{1 + \frac{I}{I_{sat}} + 4\frac{\delta^2}{\Gamma^2}} \tag{2.5}$$

where $I_{sat} = \frac{2\pi^2\hbar c\Gamma}{3\lambda^3}$ is the saturation intensity of the transition. Eq. 2.5 is obtained by solving the *Optical Bloch equations*. The characteristic trend of the scattering force is

$$F_{scatt} \sim \frac{\Gamma I q_0}{\delta^2} \tag{2.6}$$

so one obtains:

- It is proportional to the inverse of the detuning square δ^{-2}. Therefore decrease fast with the detuning δ.

- It is linear in q_0 and Γ. The force is more intense for short wavelengths λ and strongly allowed transitions.
- The force is maximum for $\delta = 0$ and $I \gg I_{sat}$, $F_{scatt}|_{MAX} \sim \frac{\hbar q_0 \Gamma}{2}$. It is equivalent to say that the atom has acquired a momentum $\Delta p = \hbar q_0$ in the time necessary to absorb and emit a photon, $t = 2\tau$.

This scattering force is related to the imaginary part of the complex refractive index of a material $\eta(\omega_0) = n + i\kappa$, i.e. the absorption coefficient κ. The real part, the refractive index, is instead related to the dipole force.

Dipole force

Differently from the scattering force, the dipole force is not related to the absorption of light, but to its deflection by a dispersive medium and therefore to the real refractive index of the target n_t and $\boldsymbol{\nabla} I$, the light intensity gradient. An example is proposed to explain the previous statements, from Ref. [63]. A sphere in a non-uniform intensity laser beam is considered. The difference in the intensity of the light refracted on opposite sides of the sphere leads to a force. If a narrow uniform beam is considered, the experienced force is $F = \left(\frac{IA}{c}\right) 2\sin(\theta)$ where $\frac{IA}{c}$ corresponds to the rate at which radiation with intensity I carries momentum through a cross-sectional area A, perpendicular to the direction of propagation. The non-uniform intensity radiation can than be thought as a set of uniform beams each leading to a different force. The force dependence on intensity gradient is then obvious. Furthermore single-beam forces depend on θ, but this angle is set by the ratio between the sphere target refractive index n_t and the external medium refractive index n_ext: $\theta = \frac{n_t}{n_{ext}}$. Then the dependence of the dipole force from the refractive index n_t is also recovered. In particular if $n_t > n_{ext}$ the sphere feels a force in the direction of increasing intensity, i.e. the sphere is confined at the focus of the radiation. This is the principle used in optical dipole traps.

Formally, using quantum mechanics the force expression is:

$$F_{dip} = -\frac{1}{2I_{sat}} \frac{\boldsymbol{\nabla} I \hbar \delta}{1 + \left(\frac{2\delta}{\Gamma}\right)^2 + \frac{I}{I_{sat}}} \tag{2.7}$$

Main properties are recovered: it is proportional to the gradient of the intensity, vanishes for resonant light $\delta = 0$ and decreases slowly with detuning $(1/\delta)$. Eq. 2.7 is of particular interest in the limit $\delta \gg \Gamma$, i.e. for very intense and far detuned beams. In fact dipole force is employed to trap atoms in optical dipole traps, there heating sources for the system have to be avoided. Because of its dependence on the photon scattering rate, the scattering force might lead to an unwanted heating of the system, this is why, keeping in mind that $F_{scatt} \sim \frac{1}{\delta^2}$ asymptotically, very intense and far detuned beams are then used in optical dipole traps. In the limit $\delta \gg \Gamma$ the Eq. 2.7 results

$$F_\mathrm{dip} \sim -\frac{\hbar}{8\delta} \Gamma^2 \boldsymbol{\nabla} \left(\frac{I}{I_{sat}}\right) \quad . \tag{2.8}$$

F_dip is attractive towards an intensity maximum for $\delta < 0$ ($\omega_0 < \omega_{01}$, red detuning) while repulsive from it in the case of blue detuning $\delta > 0$. Therefore the scattering force is effective with a resonant and collimated beam while dipole force for a detuned and focalized laser. In a real atom there are in general many transitions that can be red or blue detuned with respect of the radiation, so F_{dip} in general has to take into account all of them:

$$F_{dip} = -\sum_i \frac{\hbar}{8\delta_i} {\Gamma_i}^2 \vec{\Delta}\left(\frac{I}{I_{sat}}\right) \equiv -\frac{\alpha(\omega_0)}{2} \vec{\Delta}\left(\frac{I}{I_{sat}}\right) \quad . \tag{2.9}$$

where $\alpha(\omega_0)$ is the polarizability, which describes the polarization induced by the radiation in the medium. In order to employ the dipolar force to act on an atomic system is then necessary the knowledge of its polarizability.

Polarizability

Polarizability characterizes the linear response of a neutral particle to an external field $\vec{E}$. It is defined as the ratio between the induced dipole moment and the field acting on the atom. If the field is static, i.e. $\omega_0 = 0$, then the polarizability is a real number, called *static polarizability*. If the field is oscillating, i.e. $\omega_0 \neq 0$, then the polarizability is a complex, frequency-dependent quantity, the *dynamic polarizability*: $\alpha(\omega_0) = \alpha_{real} + i\alpha_{im}$. The imaginary part is related to the absorption and scattering of photons while the real part gives rise to Stark shifts of the energy levels. The wavelength that induces an equal shift on the two relevant atomic states, for trapping, is called *magic wavelength*.

The presence of light fields $\vec{E} = E_0 e^{-i\omega_0 t}\hat{\epsilon} + c.c$ shifts then the energy levels of the atom because of Stark effect. For a non-degenerate level, using a perturbative theory, this shift is quadratic with respect to the electric field amplitude E_0:

$$E_{unperturbed} - E_{perturbed} \sim \delta E^{(2)} = (eE_0)^2 \sum_j \frac{|<j|x|i>|^2}{E_i - E_j} \equiv -\frac{1}{2}\alpha E_0^2 \quad , \tag{2.10}$$

where the first order is zero for symmetry and α is the polarizability of the medium. The previous formula is no longer valid for degenerate levels, because level mixing can occur. A particular case is, however, the one of an homogeneous field. In that case in fact, for symmetry reasons, no mixing between states is possible. The non-degenerate formula can, therefore, be used.

In general the light field has a non zero degree of ellipticity of polarization, so the calculation of the first non-vanishing term of the Stark effect requires a diagonalization, through the solution of the secular equation $||\delta E \delta_{MM'} - T_{mm'}|| = 0$. Using the dipole approximation for the interaction hamiltonian, the explicit form of $T_{MM'}$ is:

$$T_{MM'} = \frac{1}{4}E_0^2 \sum_{\substack{p=0,1,2 \\ \lambda=-p\ldots p}} C^{JM'}_{JMp\lambda}\alpha_p(\omega_0)\{\epsilon \bigotimes \epsilon^*\}_{p\lambda} \tag{2.11}$$

$\alpha_p(\omega_0)$ and $\{\epsilon \bigotimes \epsilon^*\}_{p\lambda}$ depending only on the radiation frequency and polarization. The parameter α_p for p = 0,1,2 is the amplitude of the scalar, vector (asymmetric) and tensor (symmetric) Rayleigh scattering. It is convenient to introduce the corresponding parameters [64]:

$$\alpha^s_{nJ} = \frac{1}{\sqrt[n]{3}}\alpha_0 \tag{2.12}$$

$$\alpha^a_{nJ} = -\alpha_1 \sqrt[2]{\frac{2J}{J+1}} \tag{2.13}$$

$$\alpha^T_{nJ} = \Big(\frac{2J(2J-1)}{3(J+1)(2J+3)}\Big)^{\frac{1}{2}}\alpha_2 \tag{2.14}$$

$$\tag{2.15}$$

The Stark effect of an atomic level in an electric field is then completely determined by these three components of the polarizability, with weights depending on the angular momentum quantum numbers and trapping laser polarization. The electron configuration of Dy, thus the complex energy spectrum, makes theoretical evaluation of the dynamic polarizability very challenging [65, 66].

On the other hand, accurate experimental measurements of both scalar and tersor components of the polarizability have been experimentally determined for both the ground [67] and one excited state [68], for a trapping wavelength of 1064 nm. The method for the determination of the ground state polarizability is briefly described in the following. The stark shift corresponds to the optical trapping potential:

$$U(r, \omega_0) = -\frac{2\pi a_o^3}{c} I(r)\alpha(\omega_0) \tag{2.16}$$

where a_o is the Bohr radius, c the sound velocity and $I(r)$ the laser intensity. Approximating the laser as a gaussian beam the potential in the center of the trap is harmonic and the trap frequency is

$$\omega_{\text{trap}} = \sqrt{\frac{4U_{min}}{m\bar{\omega_0}^2}} = \sqrt{\frac{16a_o^3}{c}\frac{P\alpha(\bar{\omega_0})}{m\bar{\omega_0}^4}} \tag{2.17}$$

where P is the power of the laser, m the Dy mass and $\bar{\omega_0}$ the effective frequency in the centre of the trap. The key idea of the experiment in Ref. [67] is to introduce on the same setup another atomic system, in this case K, with well known polarizability at 1064 nm to get rid of the normally poorly known laser parameters P and $\bar{\omega_0}$, introducing the ratio $\frac{\omega_{\text{trap}}^{Dy}}{\omega_{\text{trap}}^{K}}$. The polarizability is then calculated using Eq. 2.18, needing only the ratio $\frac{\omega_{\text{trap}}^{Dy}}{\omega_{\text{trap}}^{K}}$ of the two frequency measurements:

$$\alpha^{Dy} = \alpha^{K}\frac{m^{Dy}}{m^{K}}\left(\frac{\omega^{Dy}}{\omega^{K}}\right)^2 \quad . \tag{2.18}$$

The obtained polarizabilities are $\alpha^s_{66,-8} = 184.4(2.4)\ \alpha_0$ and $\alpha^T_{66,-8} = 1.7(6)\ \alpha_0$, for the ground state $|J=-8, m_J=-8>$. In Ref. [68] the polarizability of the excited state $|J'=-9, m_{J'}=-9>$ is found using the theoretical value of the background polarizability. It results $\alpha^s_{66,-9} = 179(5)\ \alpha_0$ and $\alpha^T_{66,-9} = 35(2)\ \alpha_0$, where α_0 is the atomic unit for the electric polarizability. Note that α^a, the vector component, is zero. It is because a linearly polarized light is used.

Optical Absorption Cross Section

To introduce the cross section let us consider the example of a beam incident on to a target with n atoms per unit volume and thickness Δz. The fraction of absorbed particles if $n\Upsilon\Delta z$, also representing the probability that the photon hits an atom of the target. The cross section parameter Υ therefore characterizes the absorption probability. Considering that the absorbed fraction is equal to the loss intensity, Beer's law is recovered:

$$I(\omega_0, z) = I(\omega_0)e^{-N\sigma(\Upsilon)z} \tag{2.19}$$

It works well for low-intensity light.

2.2.2 Experimental methods

MOT Magneto-Optical Trap(MOT)

A Magneto-Optical Trap is an experimental tool used to simultaneously trap and cool atoms. It is achieved with the combination of a magnetic quadrupole field and three pairs of counter propagating laser beams. The MOT idea is considered in two steps. First the Optical Molasses concept is introduced, where no quadrupole magnetic field is present. Then, the introduction of a magnetic field is considered.

The idea of the Optical Molasses, is to introduce a viscous force $\vec{F} = -\gamma\vec{v}$ that slow the atom, as a bullet in a budding. In order to do so, it is used the radiation pressure principle: the net effect of each absorption-emission cycles is to change the atom's momentum. Let's consider a moving atom with velocity v. A counter propagating photon with frequency ω_0 is blue Doppler shifted for the atom. The photon frequency seen by the atom is then $\omega' = \omega_0 - \vec{q}\cdot\vec{v}$. In order to have resonant light, a red detuned laser has to be used. The momentum kick given to the atom is then $\vec{q} = -\frac{\vec{v}m}{\hbar}$, where m is the atom mass. A pair of counter propagating beams is usually used to slow atoms in both directions. The presence of the second beam, however, does not change the previous derivation. In fact, while the counter propagating photon is resonant with the atom, the other is red-detuned by the double, and thus not interacting efficiently with the atom.

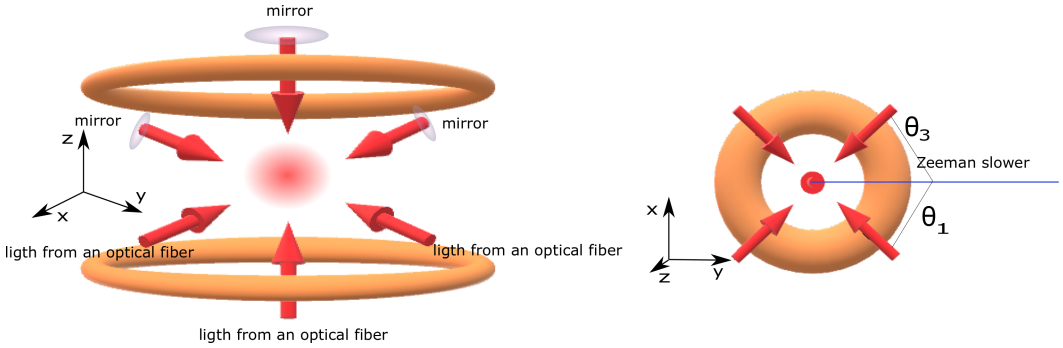

Figure 2.7: Scheme of the MOT. The left image is a 3D representation. Each beam comes out from an optical fiber and is then reflected by a mirror. The right image is a vertical view. The angles θ_1, θ_2 are $\sim 45°$ respect to the Zeeman slower axis.

Formally, from Eq.s 2.2 and 2.5, the scattering force is

$$\vec{F_{\text{scatt}}} = \hbar\vec{q}\frac{\Gamma}{2}\frac{\frac{I}{I_{\text{sat}}}}{1+\frac{I}{I_{\text{sat}}}+4\frac{(\delta_0-\vec{q}\cdot\vec{v})^2}{\Gamma^2}} \tag{2.20}$$

where $\delta = \omega' - \omega_{01} = \omega_0 - \vec{q}\cdot\vec{v} - \omega_{01} \equiv \delta_0 - \vec{q}\cdot\vec{v}$, δ_0 is the detuning in the reference system of an atom at rest. Considering a pair of counter propagating beams, the scattering force becomes

$$\vec{F_{\text{tot}}} = \hbar\vec{q}\frac{\Gamma}{2}\frac{I}{I_{\text{sat}}}\left[\frac{1}{1+\frac{I}{I_{\text{sat}}}+4\frac{(\delta_0+\vec{q}\cdot\vec{v})^2}{\Gamma^2}} - \frac{1}{1+\frac{I}{I_{\text{sat}}}+4\frac{(\delta_0-\vec{q}\cdot\vec{v})^2}{\Gamma^2}}\right] \quad . \tag{2.21}$$

If a low laser intensity is considered ($I \ll I_{\text{sat}}$) as well as small atom velocities ($\vec{q}\cdot\vec{v} \ll \Gamma$, thus $\delta \sim \delta_0$), Eq. 2.20 takes the form $\vec{F} \sim \vec{F_0} \pm \gamma\vec{v}$ and $\vec{F_{\text{tot}}} = 2\gamma\vec{v}$ with γ:

$$\gamma = \delta_0\frac{4\hbar q^2}{\Gamma}\frac{I}{I_{\text{sat}}}\left[\frac{1}{1+\left(\frac{2\delta_0}{\Gamma}\right)^2}\right]^2 \tag{2.22}$$

negative for red detuned light.

The minimum temperature achievable with the molasses is the Doppler temperature:

$$T_{\text{D}} = \frac{\hbar\Gamma}{2k_{\text{B}}} \tag{2.23}$$

which depends only on the natural linewidth Γ of the transition used. This limit temperature is the consequence of the atom recoil following the spontaneous emission, $v_{\text{rec}} = \frac{\hbar q}{m}$. In stationary conditions:

$$\frac{d}{dt}(E_{\text{cin}}) = 0 = E_{\text{visc}} + E_{\text{therm}} = -\gamma\langle v^2\rangle + \frac{1}{2}m\frac{d\langle v_{\text{rec}}^2\rangle}{dt} \tag{2.24}$$

$$\langle v_{\text{rec}}^2\rangle = \frac{1}{3}v_{\text{rec}}^2 R_{\text{scatt}}t \tag{2.25}$$

$$\langle v_{\text{rec}}^2\rangle^{3D} = 4v_{\text{rec}^2}R_{\text{scatt}}t \tag{2.26}$$

where $\langle\rangle^{3D}$ accounts for the effect from the uncertainty in the number of absorbed photons and three pairs of beams has been considered. Using Eq. 2.5 in the limit $I \ll I_{\text{sat}}$ and $\vec{q}\cdot\vec{v} \ll \Gamma$, the expression for T_{D} is recovered.

Scattering force and Doppler effect are used to cool atoms but not to trap them. Because of random walk and scattering atoms are quite localized but the local density is still very low.

The combination of a spatially dependent magnetic field, polarized laser beams and excited state magnetic degeneracy, gives the scattering force a spatial dependence.

A schematic representation of the MOT is on the left side of Fig. 2.7. Let us focus on how the trapping effect is achieved. As a magnetic field gradient is created by two coils, then position dependent Zeeman splitting of atomic energy levels occurs. An advantage of it is taken by using polarized beams, chosen to be resonant with the lowest Zeeman state. The detuning becomes position dependent:

$$\delta = \delta_0 - \vec{q}\cdot\vec{v} - \frac{g\mu_{\mathrm{B}}}{\hbar}\frac{\partial\vec{B}}{\partial z}\cdot\vec{z} \tag{2.27}$$

Then $F \sim -\gamma v - \frac{\gamma\beta}{q}z$ is an elastic force proportional to the displacement from the centre of the field. In the end, a capture velocity v_{cap} estimation can be given. In the regime of $I \ll I_{\mathrm{sat}}$ and $\delta \sim 0$, the maximum force is $F^{Max}_{\mathrm{scatt}} \sim \hbar q\frac{\Gamma}{2}$. The best condition would be the one where all the molasses experience F^{Max}_{scatt}. If D is the molasses diameter then to stop an atom $\Delta E_{\mathrm{kin}} = \frac{1}{2}mv^2_{\mathrm{cap}} \sim F^{scatt}_{\mathrm{Max}}D$ hence an overestimation of v_{cap} is $v_{\mathrm{cap}} \sim \sqrt{\frac{\hbar q\Gamma D}{m}}$.

Doppler broadening and saturated absorption spectroscopy

In order to control the stability of a laser frequency, a lock signal is needed. Saturated absorption spectroscopy allows to have a Doppler-free reference signal. Doppler broadening is briefly recorded, then saturated absorption spectroscopy technique is presented.

Atoms of a gas have a Maxwell-Boltzmann velocity distribution, the fraction of atoms with velocity in the range v, $v + dv$ is:

$$f(v)dv = \frac{1}{\langle v\rangle\sqrt[2]{\pi}}e^{-\frac{v^2}{\langle v\rangle^2}}dv \tag{2.28}$$

$\langle v\rangle$ being the mean value of the distribution, but also the most probable speed for atoms. Each atom with a velocity v is resonant with a radiation $\omega' = \omega_{01} + \vec{q}\cdot\vec{v}$, thus the absorption has the gaussian line shape:

$$g_{\mathrm{Doppler}} = \frac{c}{\langle v\rangle\sqrt[2]{\pi}\omega_{01}}e^{-\frac{c^2}{\langle v\rangle^2}\left(\frac{(\omega-\omega_{01})}{\omega_{01}}\right)^2} \tag{2.29}$$

The Doppler broadening is an inhomogeneous broadening defined as the FWHM of the gaussian distribution $\frac{\Delta\omega_{\mathrm{Doppler}}}{\omega_{01}} = 2\sqrt{ln2}\frac{\langle v\rangle}{c} \sim \sqrt{T}$. A qualitative description of the saturated absorption spectroscopy is now given. For further documentation see Ref. [62, 69]. A scheme is shown in Fig. 2.8a. Atoms are irradiated with a laser source whose frequency is swept around the atomic resonance, *Probe*. The signal on the photodiode is flat off resonance and minimum when the resonance frequency is reached, Fig. 2.8b. Because of the Doppler broadening however is difficult to resolve the transition. A counter-propagating *Pump* beam is then introduced as to saturate the atoms at rest on the excited state. The probe does not affect those atoms pumped and a narrow transmission dip, with natural broadening, is observed at the center of the Doppler feature, see Fig. 2.8c. Such a signal can be used as a Doppler-free reference signal.

Zeeman Slower

The zeeman slower (ZL) is an experimental method to cool down very hot atoms. The basic idea is to use a variable magnetic field B and exploit the induced Zeeman splitting to keep atoms resonant with a slowing radiation while they are decelerated. The Zeeman splitting has the form:

$$\Delta E = \mu_{\mathrm{B}}B(g_{\mathrm{f}}m_{\mathrm{J_f}} - g_{\mathrm{i}}m_{\mathrm{J_i}}) \qquad . \tag{2.30}$$

If $J_{\mathrm{i}} = 0, J_{\mathrm{f}} = 1$, then the detuning becomes $\delta = \delta_0 + \delta_{\mathrm{Doppler}} + \delta_{\mathrm{B}} = \delta_0 + \vec{q}\cdot\vec{v} \mp g\frac{\mu_{\mathrm{B}}B}{\hbar}m_{\mathrm{J}}$ where the $\mp$ sign depends on the light polarization: $\sigma^-(\sigma^+)$ corresponds to $\delta_{\mathrm{B}} = g\frac{\mu_{\mathrm{B}}B}{\hbar}m_{\mathrm{J}}$ ($\delta_{\mathrm{B}} = -g\frac{\mu_{\mathrm{B}}}{\hbar}m_{\mathrm{J}}$) which means a blue (red) detuned resonant light.

A Zeeman slower can have three standard configurations:

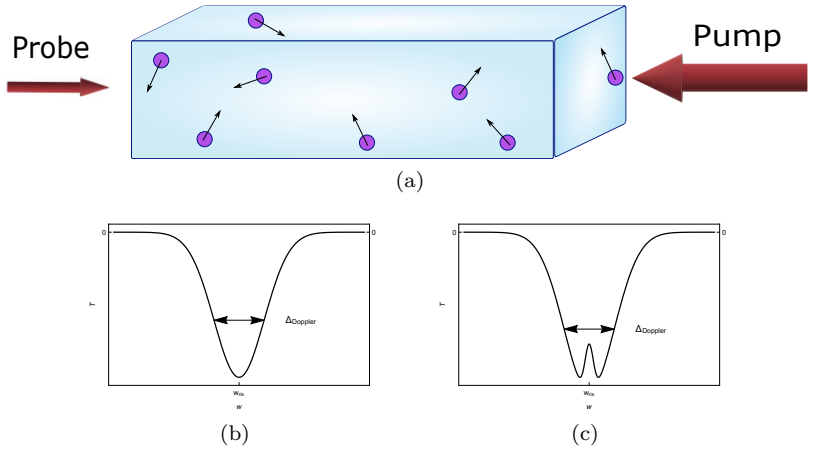

Figure 2.8: Panel **a**. Saturated absorption scheme. A vapor cell is injected with probe and pump beams. Panel **b**. Transmission signal on a photodiode versus $\omega - 0$ probe. Panel **c**. Transmission signal on a photodiode in the presence of a pump.

- $\boldsymbol{\sigma^+}$: The radiation employed is resonant with the transition ω_{01}, thus with a still atom. Zeeman effect is used to balance the Doppler shift. At the end of the process this configuration entails a radiation resonant with slow atoms, this is a disadvantage for a subsequent MOT.

- $\boldsymbol{\sigma^-}$: It employs light resonant with the Doppler shifted level at the beginning of the ZS. The ZS keeps atoms resonant while they are slowed down, but laser becomes completely detuned as atoms exit the ZS. This advantage is balanced by the problem that very strong magnetic fields are required.

- **Spin flip**: This slower is designed so that the atoms are first slowed in a σ^- configuration and then sent to a σ^+. The light is resonant with atoms with a mean velocity, while the external magnetic field has an inversion near the middle of the ZS apparatus. It has the double advantage of using not too much detuned light without being resonant with slow atoms.

ODT Optical Dipole Trap

As the DDI does not conserve the magnetic quantum number m_j, dipolar relaxation processes are allowed. To prevent such processes, atoms have to be prepared in the lowest magnetic sub-state. These state can be trapped in ODTs. The Optical Dipole Trap exploits the dipole force, in Eq. 2.8 in the case of intense far off resonant light. Dipole force is conservative thus can be thought as the gradient of a dipole potential $U_\mathrm{dip} = \frac{\hbar}{8\delta}\Gamma^2\frac{I}{I_\mathrm{sat}}$, where the atoms move. If the frequency is red detuned $\delta < 0$ the potential is attractive. Atoms in a tightly-focused laser beam are attracted towards the region of high intensity, both in the radial direction and along the axis of the beam. The dipole force then confines atoms at the focus of a focused laser beam. In our case $I(r,z)$ has a gaussian profile:

$$I(r,z) = \frac{2W}{\pi w_0^2}\frac{1}{1+(\frac{z}{z_\mathrm{R}})^2}e^{-\frac{2r^2}{w^2(z)}} \tag{2.31}$$

where z is the propagation direction, r the distance from the z axis, w the beam waist in a generic z position, z_R the Rayleigh distance and w_0 the beam waist at the focus position. These

quantities are related to each other by the formulas:

$$z_{\mathrm{R}} = \frac{\pi w_0^2}{\lambda} \tag{2.32}$$

$$w(z) = w_0 \sqrt[2]{1+\left(\frac{z}{z_{\mathrm{R}}}\right)^2} \tag{2.33}$$

$$\tag{2.34}$$

The dipole potential form is then:

$$U_{\mathrm{dip}}(r,z) = \frac{\hbar}{8\delta}\frac{\Gamma^2}{I_{\mathrm{sat}}}\frac{2W}{\pi w(z)^2}e^{-\frac{2r^2}{w^2(z)}} \equiv -V^D\frac{w_0^2}{w(z)^2}e^{-\frac{2r^2}{w^2(z)}} \tag{2.35}$$

In the limit of low temperature ($k_{\mathrm{B}}T < U_{\mathrm{dip}}(0,0)$), using $r \ll w_0$ and consequently $z \ll z_{\mathrm{R}}$, the potential becomes

$$U_{\mathrm{dip}}^{lowTemp} = -V^D\Big(1-\frac{2r^2}{w_0^2}-\frac{z^2}{z_{\mathrm{R}}^2}\Big) \qquad . \tag{2.36}$$

If red-detuned laser light is employed ($\delta < 0$), V^D is positive, $(r=0, z=0)$ is a minimum and V^D represents the trap depth. It leads to a spatial distribution of atoms in the trap:

$$n(x,y,z) = n_0 e^{-\left(\frac{x^2}{2\sigma_{\mathrm{x}}^2}+\frac{y^2}{2\sigma_{\mathrm{y}}^2}+\frac{z^2}{2\sigma_{\mathrm{z}}^2}\right)} \tag{2.37}$$

$$n_0 = \frac{N}{(2\pi)^{\frac{3}{2}}}\frac{1}{\sigma_{\mathrm{x}}\sigma_{\mathrm{y}}\sigma_{\mathrm{z}}} \tag{2.38}$$

$$\sigma_{\mathrm{x,y,z}}^2 = \frac{k_{\mathrm{B}}T_{\mathrm{x,y,z}}}{M\omega_{\mathrm{x,y,z}}^2} \tag{2.39}$$

$$\omega_{\mathrm{x,y}}^2 = \frac{4V^D}{Mw_0^2} \qquad \omega_{\mathrm{z}}^2 = \frac{2V^D}{Mz_{\mathrm{R}}^2} \tag{2.40}$$

An ODT is then realized with high power, red detuned and focused laser beam. It does not lead to a cooling effect so it is often combined with evaporative cooling. Evaporative cooling, which is not treated in detail here but an extensive study for the dipole trap case can be found in Ref [70], consists in slightly reducing the laser intensity so that hotter atoms evaporate, it is a velocity distribution tail-cut [71]. Evaporative cooling in a far detuned trap is very powerful also because no spontaneous absorption is present as it works with detuned light, and the thermal effect that in the MOT leads to a temperature limit is here absent. Temperature of the order of nK can be reached with this technique.

2.3 Experimental setup

This section is devoted to a short description of the setup used to condense dysprosium atoms. Since I did not take part in the apparatus realization I only report on the different components and refer to Ref.s [62, 72] for details. However, in the end of the section, I present an observation of the Bose-Einstein condensate achieved with its relative analysis. A scheme of the apparatus is sketched in Fig. 2.9. Experimental sequence starts from an oven chamber heated up to 1200 °C, containing ^{162}Dy atoms. Because of the high vapour pressure the atoms spread out in all direction with a mean velocity ~ 480 m/s. The atomic cloud is then transversely cooled and reduced to an atomic beam. Such a beam enters a differential vacuum stage which embodies the Zeeman Slower, whose ending point is the science cell with a 10^{-10}Torr pressure. After passing through the ZS, the atomic beam reaches the science cell with a mean velocity ~ 10 m/s. The atoms are then trapped and cooled by a MOT employing 626 nm light. Because of the recoil energy of the scattered particles the temperature reachable in the MOT is of the order of 10 μK, while few

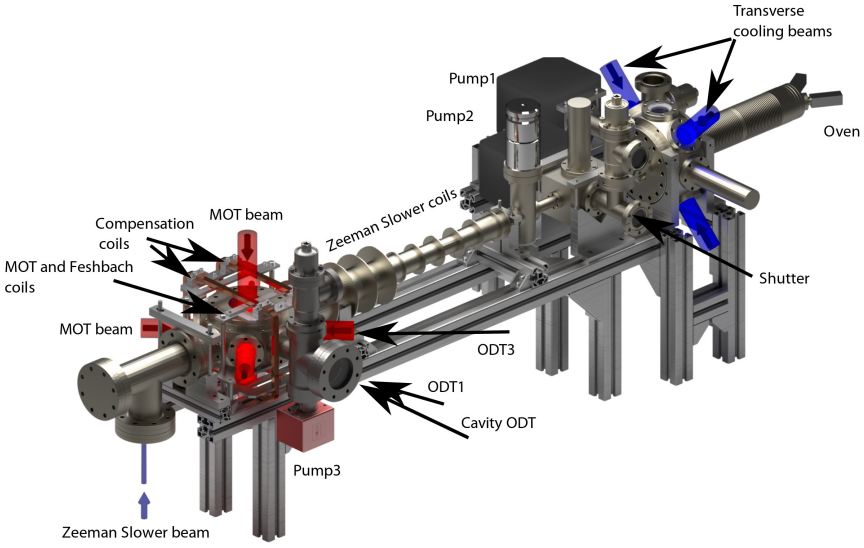

Figure 2.9: Scheme of the Apparatus.

nK are necessary for condensation. The thermal cloud is then further cooled down by a forced evaporative cooling step performed in a single beam ODT and in the high-intensity standing-wave pattern produced by and optical resonator. When the cloud is cold enough the resonator is substituted by another ODT. Two ODTs are used to trap the cold gas in 3 dimensions, for historical reasons the two traps are called ODT1 and ODT3. A cold dilute gas is achieved, further evaporated and in the end it experiences the first order transition to a Bose-Einstein condensate.

The experimental apparatus is mounted on two optical benches. Laser sources are provided on one bench and then transported to the other one through single mode polarization-maintaining optical fibers. The other bench consists of the setup of Fig. 2.9.

Laser systems

Blue (421 nm) laser system. The light is obtained by a multi-step process. First a Ti:sapphire crystal inside a ring cavity is pumped with 10 W of green light at a wavelength $\lambda = 532$ nm generated by a diode-pumped solid state commercial laser. Up to 2.4 W of $\lambda = 842$ nm light are obtained at the output of the Ti:sapphire system. Such a light is further frequency doubled using an LBO crystal inside a ring cavity, second harmonic generation (SHG) cavity. Finally up to 1 W of blue light is obtained.

Blue light is splitted in three main branches: spectroscopy and frequency lock, transverse cooling and imaging, Zeeman slower. To be able to shift the frequency of the laser over a large range, double and single passages trough 350 MHz Acusto-Optical Modulators are used. The lock of the SHG cavity is done using a piezo controlled by the Hansch-Couillad locking technique [73]. The blue light is instead locked to the atomic line by the Pound-Drever-Hall [74] technique performed on the Dy atomic beam itself. A saturated absorption spectroscopy scheme, see Sec. 2.2.2, is used in order to have a Doppler-free reference.

Red (626 nm) laser system. The light at this wavelength is obtained by a commercial compact device by Toptica. An external cavity laser diode generates a low intensity radiation at 1252 nm that is amplified by a Master-Oscillator Power-Amplifier (MOPA) and then frequency doubled in a bow-tie cavity in order to obtain nearly 1W of radiation at the desired wavelength. This light is used for the three retro reflected beams of the MOT. Reference signal for the lock is provided by saturated absorption of a Iodine (I_2) transition. The frequency gap to the required atomic transition is bridged by AOMs.

Infrared (1064 nm) laser system. Infrared laser is provided by two commercial Mephisto lasers, Nd:Yag crystals are used to produce up to 10W of radiation. The light is employed in the first confining step after the MOT, i.e. for all ODTs. Since these processes involve dipole forces no resonant light is required, so no lock should be necessary. However the first cited confining step employs a standing wave, formed by a resonant cavity, so one of the lasers frequency is locked to the built-in cavity with a Pound-Drever-Hall scheme.

Vacuum system

Inelastic collisions cause the system to loose atoms. An inelastic collisional channel consists in the scattering between the atomic sample of cold atoms and the background hot gas in the vacuum cell. To prevent it from happening the condensate has to be realized in ultra high vacuum conditions. The vacuum system is divided in two parts. The first one is the effusive oven with a pressure $< 10^{-7}$ Torr. The second one is the ultra high vacuum science cell where up to $< 10^{-10}$ Torr is obtained. These two sections are connected by a differential vacuum stage. First the atoms flux passes in a bottleneck combined with two ion pumps, next it goes through the Zeeman slower. At the end of the ZS there's a third small ion pump with a getter cartridge. A pneumatic shutter is put at the beginning of the ZS so that when the slowed atomic sample is loaded into the MOT, the atom flux from the oven is interrupted.

Cooling and trapping systems

The first cooling step consists in a transverse cooling. The atomic beam spreads out of the oven in all directions. Transverse cooling is a 2D optical molasses slowing atoms in the (x, z) plane orthogonal to the Zeeman Slower axis y. It is intended to increase the density of atoms propagating at small angles and thus entering the Zeeman slower. For this scope the power used is ~ 75 mW and the detuning $\delta = -3\ \Gamma_{421}$ corresponding to $2\pi \times 10^2$ MHz. The collimated atomic beam enters then the ZS. The Zeeman slower is in a spin flip configuration. It uses ~ 150 mW of 421 nm blue light detuned by $\delta = -32.8\ \Gamma_{421}$ corresponding to $2\pi \times 10^3$ MHz. The propagating beam is elliptically shaped and focused at the oven position in such a way to mimic the divergence of the atomic beam with the distance. The viscous force along to the propagation direction slows atoms from ~ 480 m/s to ~ 10 m/s. At the end of the ZS two rectangular coils in quasi-Helmholtz configuration with the axis in common with the ZS are used to compensate for the disperse magnetic field emerging from the ZS itself. The field produced by such rectangular coils is called *compensation field*.

Atoms are then loaded into the MOT. It consists in three retro reflected laser beams of 626 nm light and two circular coils with vertical axis placed in anti-Helmholtz configuration that generates a linear magnetic field gradient, see Fig. 2.7 and Fig. 2.10a. The frequency and amplitude of laser beams are controlled using AOMs. $\lambda/4$ waveplates are instead utilized to circularly polarize beams. Relative intensity is adjusted by $\lambda/2$ waveplates and polarizing beamsplitters. Each retro reflected beam has a total power of ~ 150 mW. The MOT is employed in two subsequent stages. In the loading stage, AOM are frequency modulated in order to increase the MOT capture velocity. In the compression stage, modulation is switched off and δ and I are reduced in order to maintain a sufficient confining force. Because of the heavy Dy mass also the effect of the gravity has to be taken into account. The system has a preferential direction, the equilibrium position is thus not exactly in the centre of the trap, but it is lower. The combination of radiation pressure and gravitational forces leads then to a spontaneous polarization of the electronic spin. The ground Zeeman state $J = -8$ is spontaneously populated [75]. This is very convenient because, otherwise, the use of an additional repumping frequency would have been necessary to bring the system in the correct magnetic state. Images of the atoms trapped in the MOT are shown in Figs. 2.10b and 2.10c, in the horizontal and vertical plane respectively.

During the MOT compression, the system is loaded into the standing-wave pattern due to an optical resonator at 1064 nm. The use of an optical resonator allows to diminish the power

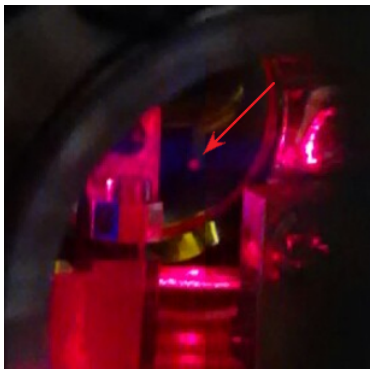

(a)

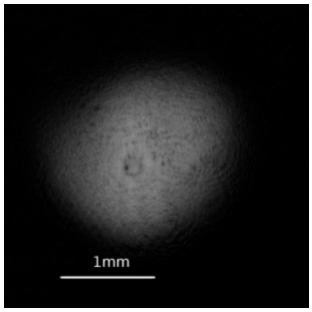

(b)

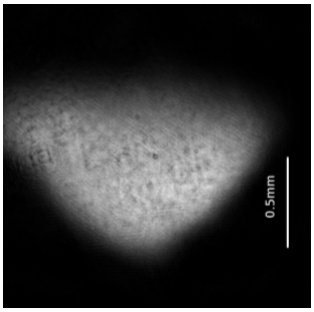

(c)

Figure 2.10: **a.** Photo of the first MOT achieved. The trapped atoms are the small red dot at the centre, pointed by the red arrow. **b.** MOT absorption image in the x, y plane, thus in the horizontal direction. The circular shape reveals the symmetry of the confining potentials with respect of the z axis. **c.** MOT absorption image in the z, y plane, thus in the vertical direction. The image has been rotated so to have the z axis in the vertical direction. The shape of the sample is due to gravity influence. The different scales of images are due to different magnification factors.

needed to confine an atomic cloud of 20 μK. A 1 W power is in fact sufficient to form a potential of the order of 100 μK employing a 300 μm waist resonator. Because of the periodicity of the structure formed by a light trapped in an optical cavity, in this trapping stage a periodic lattice is superimposed on the atomic system. Since the resonator employs light with λ =1064 nm the periodicity of such a lattice is $\lambda/2 = 532$ nm. The evaporative cooling stage starts by lowering the resonator at the end of the loading phase. Time sequence of the lasers powers during evaporating cooling ramps is shown in Fig. 2.11.

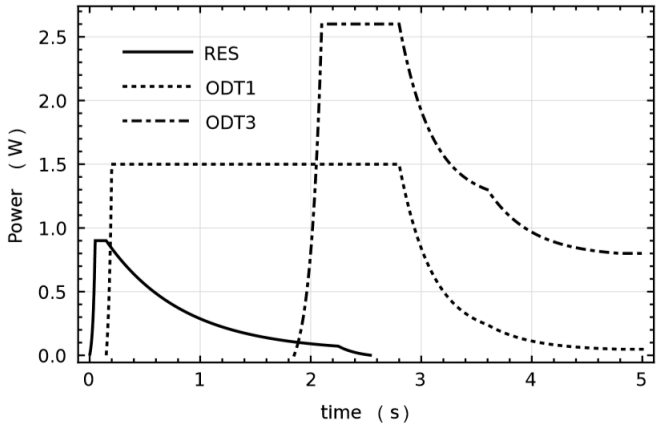

Figure 2.11: Typical time sequence of the lasers powers during evaporating cooling ramps. The ramp starts at the end of the MOT phase. Note that the resonator power is the power of the incoming beam and not the one in the cavity.

Together with the resonator also the ODT1 is switched on with 1.5 W power, see Fig. 2.13, and kept constant while the resonator power is exponentially decreased in 2 s. In this stage the system is optically trapped by the ODT1 in the plane perpendicular to the propagation direction of the ODT1 itself, and along such axis by the presence of the resonator, see Fig. 2.12. When the resonator power is reduced almost to zero, ODT3 power is ramped up to confine the sample in the x direction. Finally the system is trapped with two crossing single beam optical dipole traps with final power of $P_{ODT1} \sim 500\ mW$ and $P_{ODT3} \sim 800\ mW$ in the example.

ODT1 and ODT3 are constructed to have the strongest confinement in the polarization axis because of the dipolar nature of Dy atoms (see Sec. 1.4.3). ODT1 is then circular while ODT3 is elliptic. The waist of the ODT1 is ~ 40 μm, while ODT3 waist are ~ 35 μm and ~ 100 μm. All beams are power stabilized using an AOM, a photodiode and a PID. Power stabilization

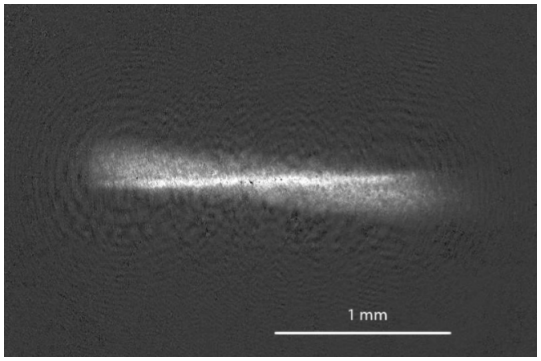

Figure 2.12: Absorption image of the transfer from the resonator to the ODT1.

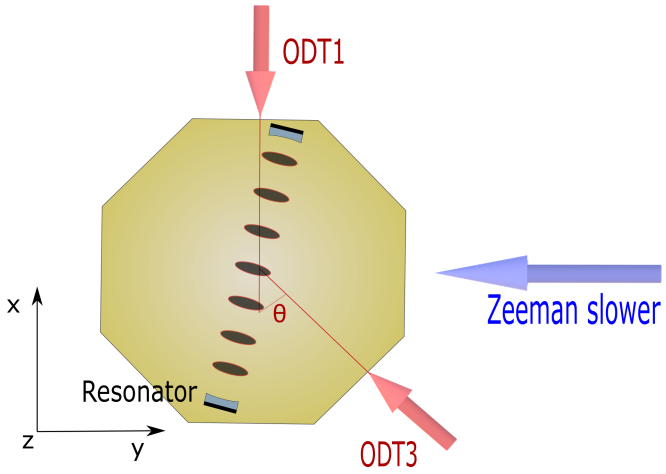

Figure 2.13: Scheme of the single beam ODTs plus the resonator. The angle θ is 40° C while the resonator is slightly misaligned respect to the x axis to allow the passage of the ODT1 beam.

is necessary as it is related to the potential depth and can lead to atom losses. After further evaporation condensation is achieved.

2.3.1 Imaging setup

All informations and measurements from the atoms are obtained by absorption imaging. This is done with a blue short flash sent to the atoms. The pulse, given along the z axis, impinges on the atomic sample and the absorption image is then recorded by a digital camera. Two different camera are available, one imaging the horizontal plane x, y (vertical camera) and the other the plane z, y (horizontal camera). This imaging process results in the destruction of the sample.

Taking a single image, the sample structure would be blurred because of the presence of background light. Such a light comes from both the lasers and the room. In order to eliminate this background, three consecutive images are taken. The first one is taken in the presence of both atoms and background light (Img_1). The second is an image of the laser light without atoms (Img_2). The third is taken switching off lasers, in order to isolate the room contribution to the background light (Img_3). The resulting image is thus a reconstruction of these three images. The background component is isolated by writing an image as $Img = \mathrm{A}I + \mathrm{B}$, where B is an offset counting for lasers and room light, I is the intensity of the imaging light and A the gain. Using such expression the final image results in

$$Img = -ln\Big(\frac{Img_1 - Img_3}{Img_2 - Img_3}\Big) \quad . \tag{2.41}$$

The system can be image both *in situ* or after a free expansion, i.e. the trap is released and the sample is imaged after a certain free expansion time called 'time of flight' (TOF). We now demonstrate that from such images the cloud size, velocity distribution and atomic temperature can be inferred. Moving along z direction the light intensity satisfies

$$\frac{\partial I(z)}{\partial z} = -(N_0(t) - N_1(t))\Upsilon(\omega)I(z) \tag{2.42}$$

with N_0 population in the ground state, N_1 population in the excited state and $\Upsilon(\omega)$ the absorption cross section. For resonant light $\Upsilon(\omega) = \Upsilon(\omega_{01}) = \Upsilon$ and for the atoms in the ground state $N_1 = 0$, the equation becomes

$$\frac{\partial I(z)}{\partial z} = -n(x, y, z)\Upsilon I \tag{2.43}$$

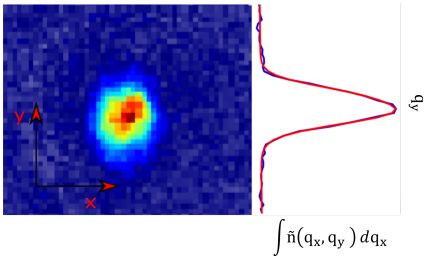

Figure 2.14: Image of a BEC in false colours and integrated 1D profile along the horizontal direction (x axis) $\int \tilde{n}(q_x, q_y)dq_x$.

Comparing the relation in Eq. 2.41 and the solution of Eq. 2.43, it results:

$$-Img = -\int_0^z n(x,y,z)\Upsilon dz \quad . \tag{2.44}$$

The atomic density in the trap is reported in Eq. 2.37, the image is thus a column density of the form

$$Img(x,y) = \frac{N\Upsilon}{(2\pi)}\frac{1}{\sigma_x\sigma_y}e^{-\left(\frac{x^2}{2\sigma_x^2}+\frac{y^2}{2\sigma_y^2}\right)} \quad . \tag{2.45}$$

The atom number as well as the sample extension in each direction can then be obtained from each image. Because of the destructive nature of the imaging, from each cycle of the sequence a single image of the sample is acquired. It is then traduced by a Python script into a matrix in false colours. It appears as in Fig. 2.14. By integrating in one direction a 1D profile is obtained and fitted with a gaussian curve $Ae^{-\frac{y^2}{2\sigma_y^2}}$. As an example, sum over rows is performed and the profile of the vertical direction y is obtained.

$$Img(y) = \frac{N\Upsilon}{(2\pi)^{\frac{1}{2}}}\frac{1}{\sigma_y}e^{-\frac{y^2}{2\sigma_y^2}} \tag{2.46}$$

$$N_y = \sqrt{2\pi}A\sigma_y/\Upsilon \tag{2.47}$$

where the second equation is obtained integrating the first one. Note that a conversion to physical unit is necessary. To convert into μm the factor is given by *pixel size*/M where pixel size depends on the camera and M is the magnification used. The typical range of N is $(1-5)\times 10^4$.

If the image is taken after a TOF, the sample falls because of gravity and expands. When the image is taken the velocity has a Maxwell-Boltzmann distribution. Therefore, the width of the gaussian in Eq. 2.46 is related to the temperature T of the sample by the relation

$$(\sigma^2(t) - \sigma^2(0)) = \frac{k_B T}{m}t_{\mathrm{TOF}}^2 \tag{2.48}$$

where m is the atom mass, t_{TOF} the time of flight and $\sigma(0)$ is the extension of the sample in the trap ($t_{TOF} = 0$). The temperature of the sample can thus be inferred from a gaussian fit of a TOF image

$$T = (\sigma^2(t) - \sigma^2(0))\frac{m}{k_B t_{\mathrm{TOF}}^2} \quad . \tag{2.49}$$

Note that the same expression is recovered using Eq. 1.20, written in momentum space, and substituting $p = mv$. The resolution of the absorption imaging system can be estimate according to the Rayleigh criterion:

$$res = \frac{1.22\lambda f}{l} \tag{2.50}$$

where l is the dimension of the lens, f the focal length and λ the wavelength of the employed light. In our case $l = 2$ in ~ 50.8 mm, $f = 100$ mm and $\lambda = 421$ nm. It results a resolution of $res \sim 0.35$ μm.

2.4 Observation of Bose-Einstein condensation

The condensed fraction in the Thomas Fermi limit is characterized by an inverted parabola in the momentum distribution. On the contrary a thermal sample has a very broad mean square momentum. The appearance of a component with a narrow peak in the momentum distribution is then a clear signature of the first order phase transition toward Bose-Einstein condensation. The evidence of such transition is shown in Fig. 2.16 where the images are obtained as described in the previous section using a TOF of 60 ms. Different stages of condensation are attained by changing the final part of the ramp in Fig. 2.11 , i.e. the forced evaporative cooling.

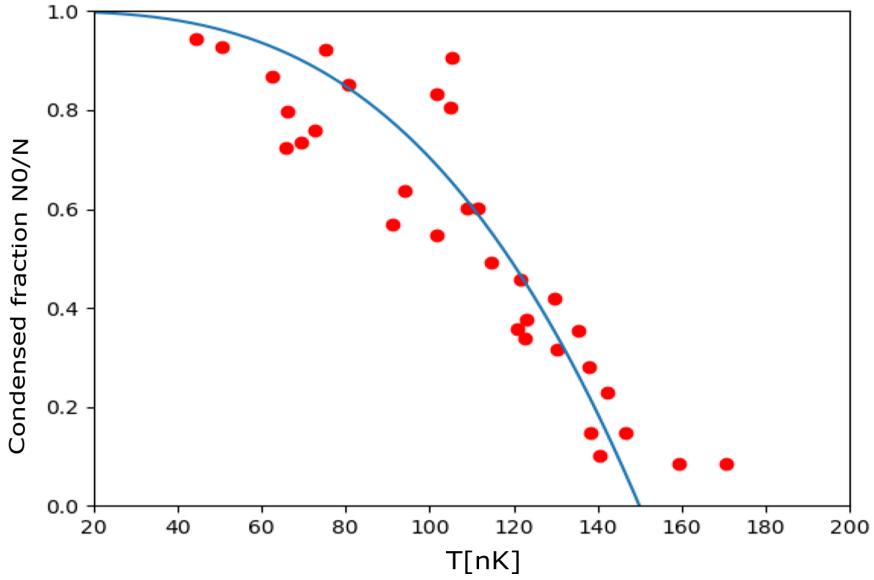

Figure 2.15: Condensed fraction as a function of the temperature. The fitted curve is obtained using Eq.1.13. Data with a critical fraction $\gtrsim 0.4$ are not included in the fit. The critical temperature is around 150 nK.

Instead of a gaussian curve for the thermal cloud and an inverted parabola for the condensed fraction, following the literature [5, 76], the fit is performed using the sum of two gaussian components. When the temperature is lowered the different extension of the two components becomes evident. Condensed fraction is measured as the ratio between the number of atoms obtained integrating the 'condensed gaussian' and the total number of atoms. Temperature is determined using Eq. 2.49 neglecting $\sigma^2(0)$, i.e. the size of the sample in the trap. The condensed fraction as a function of temperature is shown in Fig 2.15. The fitting function is that of Eq. 1.13, no finite size effects were taking into account because the used data set have number of atoms of the order of 4×10^4 so finite size effects are negligible, as discussed in Sec. 1.2. Critical temperature is around 150 nK. Note that for condensed fractions > 0.4 the thermal fraction is very small, so the fit of the image is not always meaningful, that's why for the T_c estimation only data with $N_0/N < 0.45$ have been used.

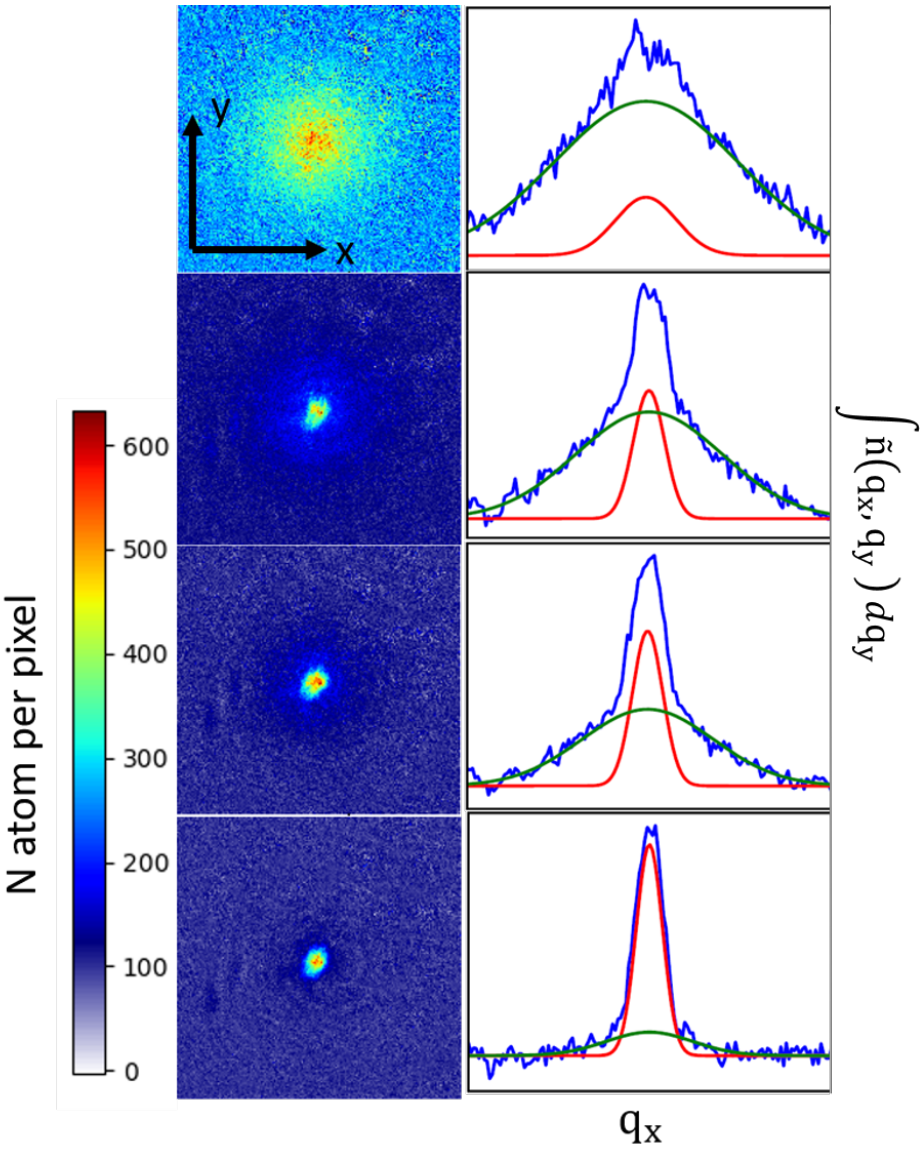

Figure 2.16: Column density distribution in the momentum space $\int \tilde{n}(q_\mathrm{x}, q_\mathrm{y}) dq_\mathrm{y}$ along the x axis for different temperatures of the sample. Both the condensed and the thermal component are fitted with a gaussian, the green curve represents the thermal component while the red curve the condensed component. It shows the transition from a thermal cloud, upper figure, to a condensate, lower figure.

Chapter 3

Characterization of the system

The experimental apparatus was briefly described in the previous chapter, now the characterization of the system is presented. Our experiment produces a dipolar BEC of ^{162}Dy atoms with atom number up to $N = 5 \times 10^4$ in an asymmetric trap with frequency $\nu_{\mathrm{x,y,z}} = (18, 53, 81)$ Hz ± 2 Hz. The system is polarized by an external magnetic field along the z axis. The condensate is initially created with a scattering length a_{s} close to its background value $a_{\mathrm{bg}} = 157(4)a_0$ [77], the dipolar scattering length of the ground state is $a_{\mathrm{dd}} \sim 130a_0$, the relative strength is then initially $\epsilon_{\mathrm{dd}} \sim 0.8$, the system is dominated by contact interaction and is thus stable. The contact interaction is subsequently tuned using a system of three Feshbach resonances located at around 5.1 G, the strongest one with a width of 35(10) mG [77]. A three body recombination constant $K_3 = 1.5(2) \times 10^{-27}$ cm^6/s has been measured for $B = 5.305$ G, larger than the value measured for the ^{164}Dy, which is of the order of 10^{-29} cm^6/s [28].

The following section reports on the determination of such characteristics of the system, starting from the measurement of trap frequencies and following with the calibration of the magnetic field with Radio Frequency (RF) spectroscopy and characterization of relevant Feshbach resonances. In the end the measurement of the three-body recombination constant K_3 is discussed. Furthermore a final section on the characterization of an high resolution imaging system is presented.

3.1 Trap frequencies

The dipolar condensate of ^{162}Dy atoms is created in an asymmetric trap represented in Fig. 3.1. The condensate is strongly confined along the z polarization axis and has a moderate confinement in the y direction. The trap is therefore different from the pancake like trap used for droplet experiments [29], but also from a cigar-shaped trap. Our confinement along y, in fact, is quite weak compared to the one used, for example, in the experiment where a roton mode was observed with Er atoms using a cigar-shaped trap [26].

Trap frequencies depend on asymptotic power values of evaporative ramps shown in Fig. 2.11. It is then important to report powers corresponding to the single frequency measurement. Power values are read on a voltmeter connected to a photodetector, the conversion has been done with a power vs electrical potential measurement. An example is shown in Fig. 3.2 for the ODT1. The conversion obtained is : $P_{\mathrm{ODT1}} = V_{\mathrm{ODT1}} \times 1.12$ mW/mV and $P_{\mathrm{ODT3}} = V_{\mathrm{ODT1}} \times 0.44$ mW/mV. In the following power values are directly reported.

The method to measure trap frequencies as well as the corresponding results are now presented. The basic idea consists in assuming that the centre of mass of the atomic system is at rest at the centre of the trap and that when a 'kick' is given to the atoms, they start an oscillation towards the centre, with the same frequency of the trap. In the vertical direction z, such a kick is given by switching off the ODTs for a short time (~ 0.6 ms), i.e. leaving the sample to fall down because of gravity. An ODT is then switched on again. In the horizontal plane (x, y)

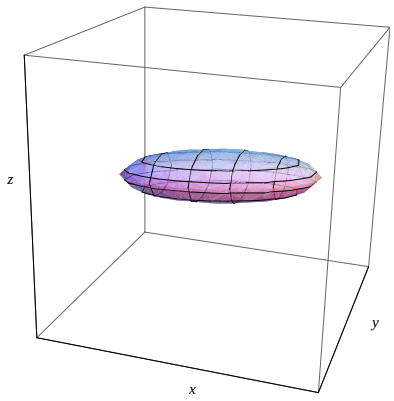

Figure 3.1: The 3D graph of equipotential surface. Powers of the optical dipole traps are $P_{\mathrm{ODT1}} = 0.045(0.001)$ W and $P_{\mathrm{ODT3}} = 0.64(0.02)$ W, corresponding trap frequencies are $\nu_{\mathrm{x,y,z}} = (18, 53, 81)$ Hz ± 2 Hz.

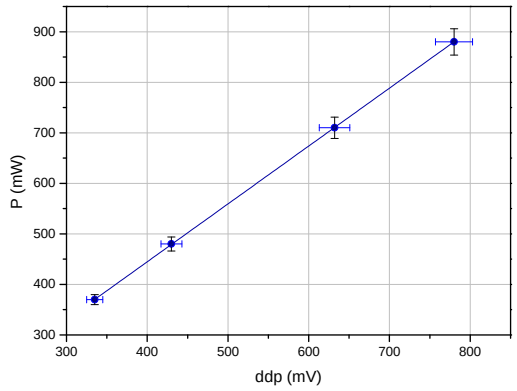

Figure 3.2: Power of the ODT1 as a function of the potential read on the voltmeter. The slope of the curve is 1.12(0.03) W/mV .

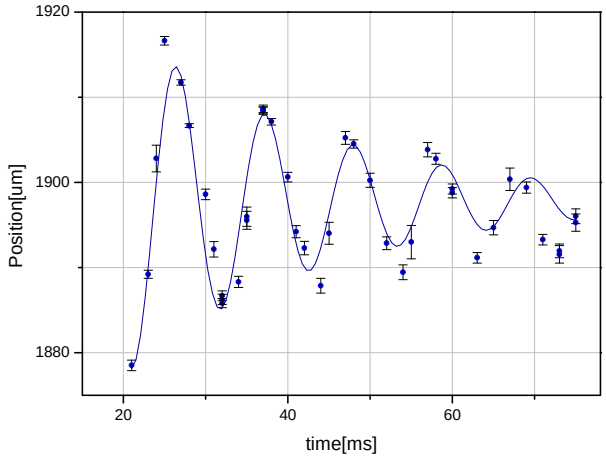

Figure 3.3: Time evolution of the vertical position of a condensate subject to the elastic recall strength of the ODT3, $P_{\mathrm{ODT3}} = 580(20)$ mW. The data are fitted with a damped sine function, according to Eq. 3.1.

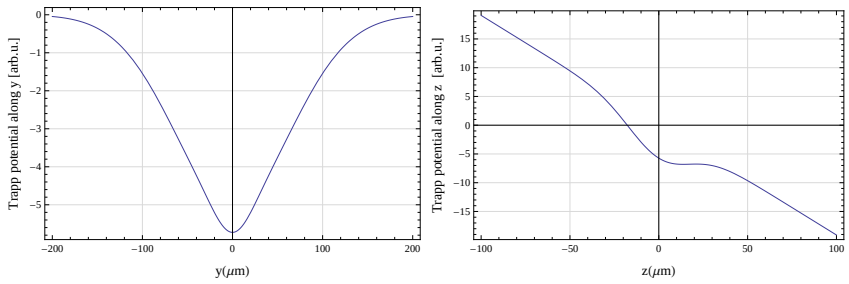

(a) (b)

Figure 3.4: Trapping potential in the y direction (**a**) and z direction (**b**)

two orthogonal compensation coils, fed by suitable currents, are employed (see Sec. 2.3). They generate a magnetic gradient in the (x, y) plane and can give an horizontal kick to the condensate. Images of the condensate are taken then, for different holding times, i.e. different duration of the oscillation phase.

The vertical frequency measurement is now presented for the ODT3 at a power of 580(20) mW. As we want to investigate the z oscillation we used the horizontal camera. The recorded data, corresponding to a line profile of the obtained image, are shown in Fig. 3.3. The fitting function is

$$z_0 + Ae^{-z/\tau}(sin(\pi(t - t_c)/B)) \tag{3.1}$$

where A is the amplitude, $\nu = 1/(2B)$ the frequency, t_c accounts for a non zero phase and τ is the decay time of the oscillation. A clear damping is visible in Fig. 3.3. Such a damping can be attributed to the presence of gravity. It modifies the trapping potential introducing an anharmonic component (see Fig. 3.4a, Fig. 3.4b). This is why a damping term is necessary for a reasonable fit function. The resulting frequency value in this case is $\nu^z_{580} = 93(2)$ Hz. The effective confining frequency is obtained combining ν^z_{ODT3} with the ODT1 frequency.

Frequency measurements in the x, y plane are done in the crossed trap with powers (ODT1, ODT3) = (41, 580) mW $\pm$ (1, 20) mW, as none of the two traps alone can provide confinement

in both x, y directions. A vertical camera was employed. Resulting data set are reported in Figs 3.5a, 3.5b. The fitting functions are:

$$f(t)^y = A\sin(\pi(t-t_c)/B) + A_1\sin(\pi(t-t_{1c})/B_1) + yo \quad (3.2)$$

$$f(t)^x = A\sin(\pi(t-t_c)/B) + xo \quad (3.3)$$

where the parameters have the same meaning as in Eq. 3.1. In Fig. 3.5a, beats between two frequencies are clearly present. Actually, a slow frequency is present also in the second picture. The sample motion is however mainly determined by the fast frequency, the slow one is thus neglected. The presence of beats is due to the angle between the beams of ODTs (see Fig. 2.13), that implies that trap axes are rotated relative to camera axes). Resultant frequencies are $\nu^y_{41;580} = (21; 60)(2)$ Hz and $\nu^x_{580} = 60(2)$ Hz.

Sometimes the trap power is not high enough to allow such methods, it is then necessary an interpolation. Trap frequencies and trap powers are related trough the relation:

$$\nu = \frac{1}{\pi w^2}\sqrt{A(P[W] - P_0)} \quad (3.4)$$

where w is the beam waist, $A = \alpha/(m\pi\epsilon_0 c)$ (α = polarizability, m = Dy mass, c = sound speed, ϵ_0 = vacuum permeability) and P_0 is the minimum power necessary to keep the atoms trapped against gravity. In the fitting procedure $\alpha = 180$ Cm^2/V is fixed, so $A = 1.35 \times 10^{-12}$ m^{2}s/kg is a constant. Since the power is set manually and the frequency measured, Eq. 3.4 becomes a formula for the determination of beam waists. Once beam waists have been determined, the same function can be used to find trap frequencies for any couple of power values ($P_{\rm ODT1}, P_{\rm ODT3}$).

An example of waists measurement is here reported for the ODT1 along z. We use five values of the power (measures here in units of voltage): $P_1 = 370$ mV, $P_2 = 470$ mV, $P_3 = 570$ mV, $P_4 = 770$ mV, $P_5 = 1$ V. Fig. 3.6 shown fitted data with Eq. 3.4. The resulting beam waist is: $w^z_{\rm ODT1} = 40(2)$ μm. Since the ODT1 is circularly polarized also $w^y_{\rm ODT1} = 40(2)$ μm.

Analogous measurements have been done for the ODT3. Resulting waists are : $w^z_{\rm ODT3} = 34(3)$ μm, $w^x_{\rm ODT3} = 97(3)$ μm. From waist knowledge we obtain the trap depth and frequencies for arbitrary powers. Powers used in the experiment, at the end of the evaporative cooling phase, are $P_{\rm ODT1} = 0.045(0.001)$ W, $P_{\rm ODT3} = 0.64(0.02)$ W. Trap frequencies are then $\nu_{\rm x,y,z} = (18, 53, 81)$ Hz ± 2 Hz.

3.2 Magnetic field calibration and Feshbach resonances

The magnetic field is calibrated through radio frequency (RF) spectroscopy between two hyperfine states at $B = 5.305$ G. The technique exploits a radio frequency to induce a transition between two Zeeman levels. We then scan frequencies in the range (2-3) MHz, with ~ 10 ms long pulses. Data recorded are shown in Fig. 3.7. The fit function is

$$f(\nu) = N_0 + \frac{A}{\Delta_{\rm RF}\sqrt{\pi/2}} e^{-2\left(\frac{(\nu-\nu_{\rm RF})}{\Delta_{\rm RF}}\right)^2} \quad (3.5)$$

where N_0 is the initial number of atoms, $\Delta_{\rm RF}$ the width of the inverted gaussian, A is the gaussian amplitude and $\nu_{\rm RF}$ the resonant frequency. When the resonant frequency is reached atoms jump from the ground state to an excited level. After a while, they spontaneously decay in the ground state $J = -8$, but they have an additional kinetic energy and thus escape from the trap. The resonant frequency is then revealed by a loss feature. The width of the curve is related to the stability of the magnetic field. In our measurement $\Delta_{\rm RF} = 3$ kHz, corresponding to a systematic uncertainty on the magnetic field of 1 mG.

The magnetic field corresponds to a current in the coils controlled by a PID (Proportional-Derivative-Integral) circuit. The current value is then converted into a voltage value B[V] read by

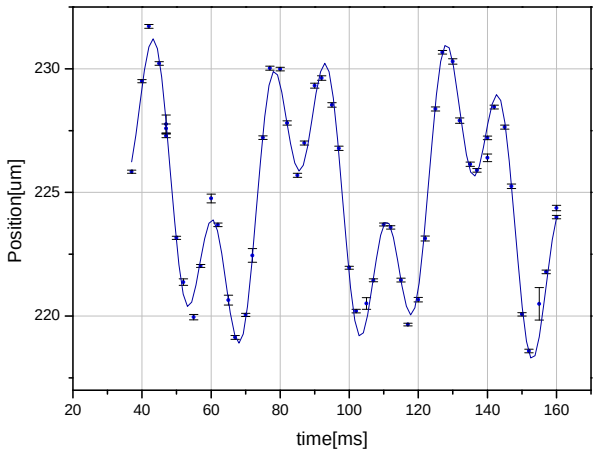

(a) y

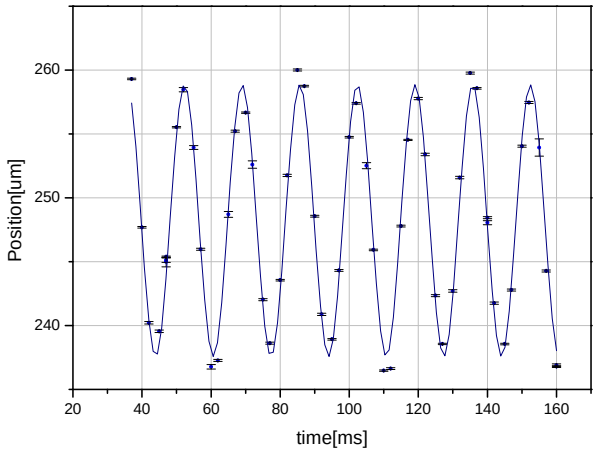

(b) x

Figure 3.5: Measurements of trap frequencies in the x, y plane. ODTs powers are $P_{\mathrm{ODT1}} = 41(1)$ mW, $P_{\mathrm{ODT3}} = 580(20)$ mW. **a**. Time evolution of the condensate position along the y axis. Data are fitted using Eq. 3.2. Resulting frequencies are $\nu^{y}_{41;580} = (21, 60)$ Hz ± 2 Hz.**b**. Time evolution of the condensate position along the x axis. The fitting function is Eq. 3.3. The frequency is $\nu^{x}_{581} = 60(2)$ Hz

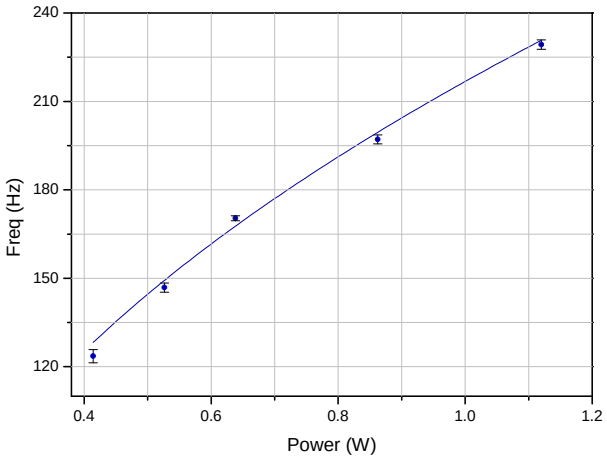

Figure 3.6: Trap frequencies as a function of the ODT1 power. The data are fitted with Eq. 3.4 with $A = 1.35 \times 10^{-12}$ m^{2}s/kg fixed constant. Optimal parameters result $P_0 = 100(30)$ mW and $w^z_{\mathrm{ODT1}} = 40(2)$ μm.

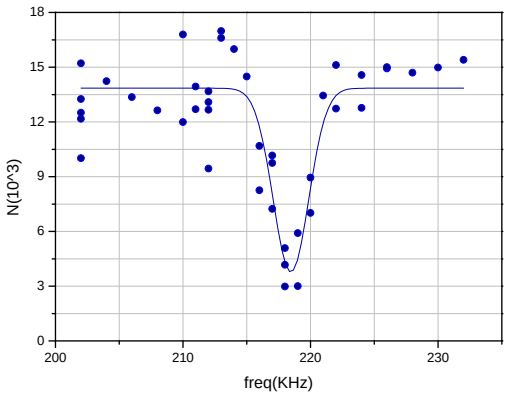

Figure 3.7: Number of atoms as a function of the RF sent on the sample. RF resonance induces a Zeeman transition $J = -8 \rightarrow J = -7$. The RF is related to the energy difference between levels that is given by Zeeman splitting, i.e. the magnetic field. The measurement of the resonant ν_{RF} and Δ_{RF} is then proportional to B and its accuracy. The fitting function is Eq. 3.5. The obtained value 3 kHz corresponds to 1 mG accuracy.

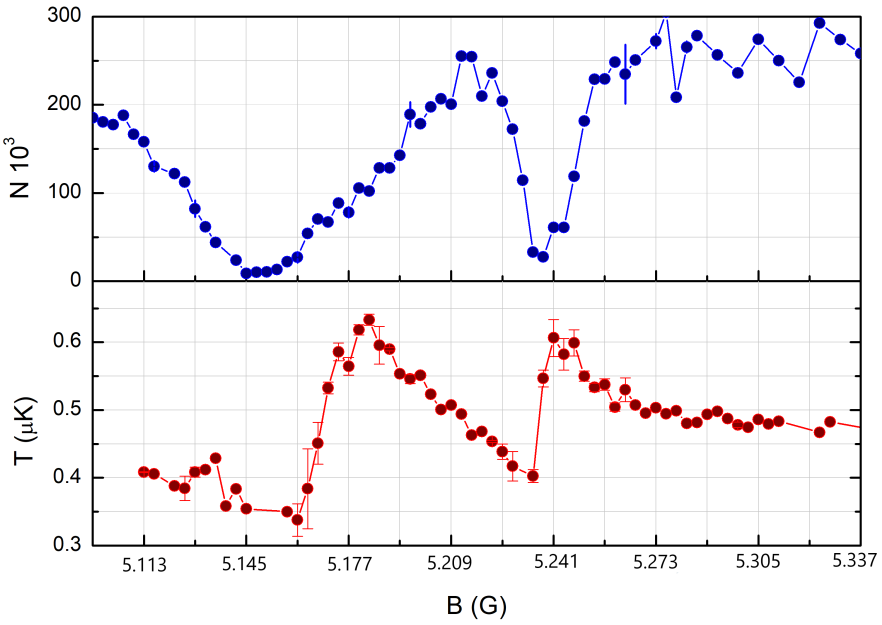

Figure 3.8: Atom number and temperature as a function of the magnetic field. The centres of the two resonances are $B_1 = 5.148(3)$ G, $B_2 = 5.234(3)$ G, while the widths are $\Delta B_1 = 37(2)$ mG, $\Delta B_2 = 8(2)$ mG

the acquisition program. B[V] is limited by one bit of writing, i.e. 1 mV, translated in a 3 mG resolution on our magnetic system. The conversion B[V]→B[G] is:

$$B[\mathrm{G}] = -0.244 + 3.1887 B[\mathrm{V}] \tag{3.6}$$

From now on the value of the magnetic field is expressed in G.

We now present the characterization of Feshbach resonances employed in our experiment. Feshbach resonances of Dy atoms have been widely studied. A new and relatively broad resonance was found at around 22 G [78], while resonances at 5.1G were already observed [77]. We finally use the three Feshbach resonances located close to 5.1 G. The estimation of positions and widths for each Feshbach resonance is done using both loss spectroscopy and thermalization measurements, employing a thermal gas of 400 nK. We wait 50 ms before imaging the sample at $B = 5.145$ G, corresponding to the wider resonance, while 1s at $B = 5.23$ G. Spectroscopy measurements and thermalization measurements are reported in Fig. 3.8. From the loss spectroscopy approximate centres and widths of the resonances are obtained. The thermalization measure allowed a more precise determination of the centres. A zoom on the narrower resonance highlights the presence of an even narrower resonance around 5.244(3) G, see Fig. 3.9. We're not able to determine its width so we assume that it is very narrow, below our measurement accuracy. The Feshbach resonances are thus $B_1 = 5.145(3)$ G with $\Delta B_1 = 32(7)$ mG, $B_2 = 5.231(3)$ G with $\Delta B_2 = 8(2)$ mG and $B_3 = 5.244(3)$ G with $\Delta \simeq 1$ mG. The last resonance then does not affect the contact scattering properties in the range of interest of magnetic field.

The conversion from the magnetic field to scattering length is done using the equation

$$a_{\mathrm{s}}(B) = a_{\mathrm{bg}}\Big(1 - \frac{\Delta B_1}{B - B_1}\Big)\Big(1 - \frac{\Delta B_2}{B - B_2}\Big) \tag{3.7}$$

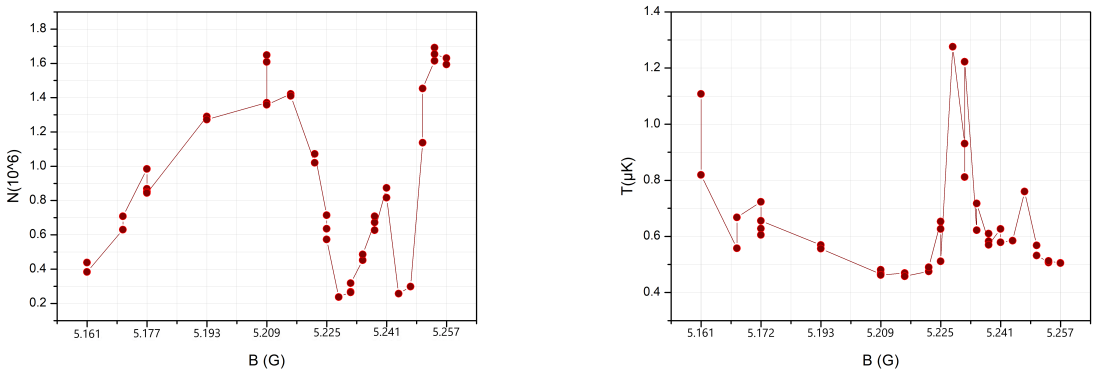

Figure 3.9: **a**. Loss spectroscopy, and **b**. thermalization of the resonance around 5.234 G. These measurements reveal the presence of a third resonance. One is centred at $B_2 = 5.228(3)$ G, while the other $B_3 = 5.244(3)$ G. We cannot determine the width of the third resonance thus we assume it is very narrow, with ΔB_3 of the order of 3 mG.

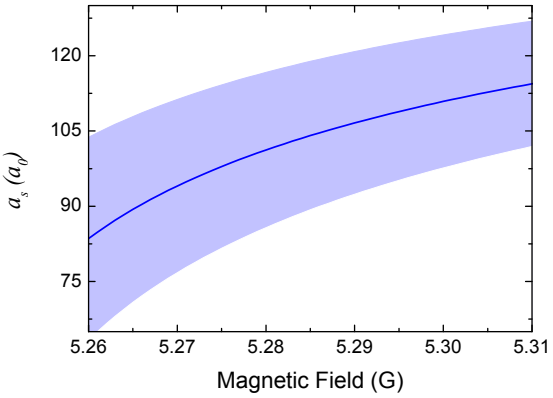

Figure 3.10: Contact scattering length versus magnetic field. The blue-solid line represents our best estimate for $a_s(B)$. The blue region sets the limits of confidence for $a_s(B)$, given the experimental uncertainty on the resonances parameters.

with our resonance values and assuming a background scattering length $157a_0$ it becomes

$$a_{\rm s}(B) = 157a_0\Big(1 - \frac{0.032[\rm G]}{B - 5.145[\rm G]}\Big)\Big(1 - \frac{0.008[\rm G]}{B - 5.231[\rm G]}\Big) \tag{3.8}$$

The dependence of the scattering length on the magnetic field is reported in Fig. 3.10 . The precision of the control on the scattering length is thus limited by the width of the resonances.

3.3 K_3 measurement

The measurement of the 3-body decay constant is performed both on a thermal sample and a BEC sample. The trap is compressed to avoid loss mechanisms different from three-body losses. Otherwise evaporation losses due to the heating of the system are possible and constitute a noise source for the K_3 determination.

We first discuss the evaluation of K_3 for a thermal sample. Time evolution of the thermal sample in the deep trap is observed [79]. The two characteristic features are a reduction of the atom number and an increase of the temperature, both due to three body losses. Such losses in fact are enhanced in the higher density regions, i.e. the centre of the cloud. Colder atoms are those with a higher probability to undergo the three-body loss process and thus escape from the trap. The sample then thermalizes at higher temperature. It is like an anti-evaporative process. A coupled equation system is then necessary for the fit of obtained data (N, T)

$$N(t) = N_0 \frac{1}{\Big(1 + \frac{3\beta^2}{\sqrt{27}}\frac{N_0^2}{T_0^3}K_3 t\Big)^{1/3}} \tag{3.9}$$

$$T(t) = T_0\Big(1 + \frac{3\beta^2}{\sqrt{27}}\frac{N_0^2}{T_0^3}K_3 t\Big)^{1/9} \tag{3.10}$$

where T_0 and N_0 are the initial temperature and number of atoms, $\beta = (m\omega_{\rm mean}^2/2\pi k_{\rm B})^{3/2}$ with $\omega_{\rm mean}$ the geometric mean frequency of the trap [80]. Instead of a combined fit it is convenient a fit of the quantity $T(t)^3N(t)^{-2}$ because it is linear in t

$$T(t)^3N(t)^{-2} = T_0^3N_0^{-2} + \frac{3\beta^2}{\sqrt{27}}K_3 t \tag{3.11}$$

We then performed the measurement on a thermal sample with a trap of $\omega_{\rm mean} = 2\pi \times 88(5)$ Hz. A recombination constant $K_3^{therm} = 1.3(2) \times 10^{-27}$ cm^6/s is obtained.

The evaluation of K_3 of a condensate in a deep trap is now discussed. For a condensate the recombination factor K_3 of a thermal cloud is reduced by a factor 3! [38]. The fitting function is obtained integrating Eq. 1.51, substituting $K_3 \to K_3/6$ and evaluating the mean density in a Thomas-Fermi approximation

$$N(t) = 5^{\frac{5}{4}}\Big(\frac{5 + 4N_0^{\frac{4}{5}}(1.15 \times 10^{18})^2(K_3/6)t}{N_0^{\frac{4}{5}}}\Big)^{-\frac{5}{4}} \tag{3.12}$$

with N_0 initial atom number. The measurement is done at $B = 5.305(1)$ G and is shown in Fig. 3.11. The resulting value for K_3 is: $K_3^{\rm BEC} = 1.5(2) \times 10^{-27}$ cm^6/s, in accordance with $K_3^{\rm therm}$. This value is larger than the values measured for ^{164}Dy, which are of the order of 10^{-29} cm^6/s [28].

The next section is devoted to describe briefly a test for an high-resolution imaging system. Such a system hasn't been implemented in our laboratory yet and therefore only preliminary results are presented.

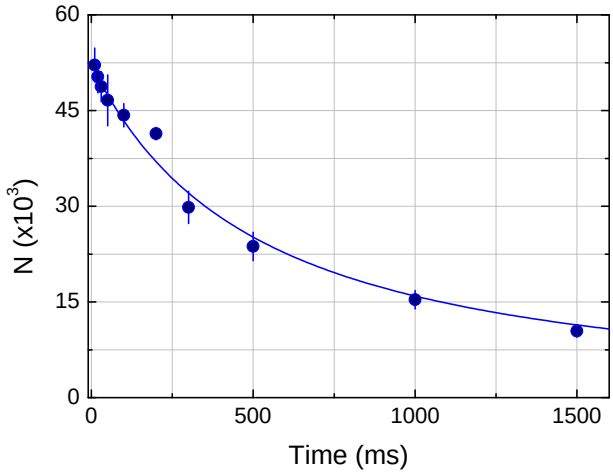

Figure 3.11: Time evolution for the atom number for a BEC confined in an optical dipole trap with frequencies $\omega = 2\pi(18, 51, 83)$ Hz, at $B = 5.305$ G. The blue-solid line is a fit to the data points, using the numerical solution valid for our specific trap geometry in Eq. 3.12.

3.4 Test of an imaging system

The aim of the tests presented here is to achieve a resolution of at least 2 μm with an imaging made by a combination of simple commercial lenses, without employing high priced custom objectives. The scope is to improve the imaging resolution of our imaging system in order to have the possibility to observed the sample in situ. Our apparatus include an absorption imaging, thus we have an image of the the momentum distribution of the system. With the implementation of our setup with an high resolution imaging system also the observation of the sample in coordinate space will be possible. We're about to test the resolution using five test targets and different optical systems.

3.4.1 Apparatus

The light source used is a He-Ne laser with wavelength λ =633 nm. It propagates directly through air from the optical desk where the laser is, to a nearby one where the optical system is set. The experimental scheme is shown in Fig. 3.12 and consists of:

1. A mirror which directs the light parallel to the desk.
2. An iris which, reducing the spot dimension, is very useful during the alignment.
3. The target on a translational stage.
4. The lens system. In the figure it is shown in a tube. It consists of two lenses: one with a short focus and the other with a long one.
5. A mirror that directs the light on the Camera.
6. A CCD camera.

Targets that have been used are:

- Two disks with a circular spot in the centre, respectively 50 and 10 μm of diameter, shown in Fig. 3.13.

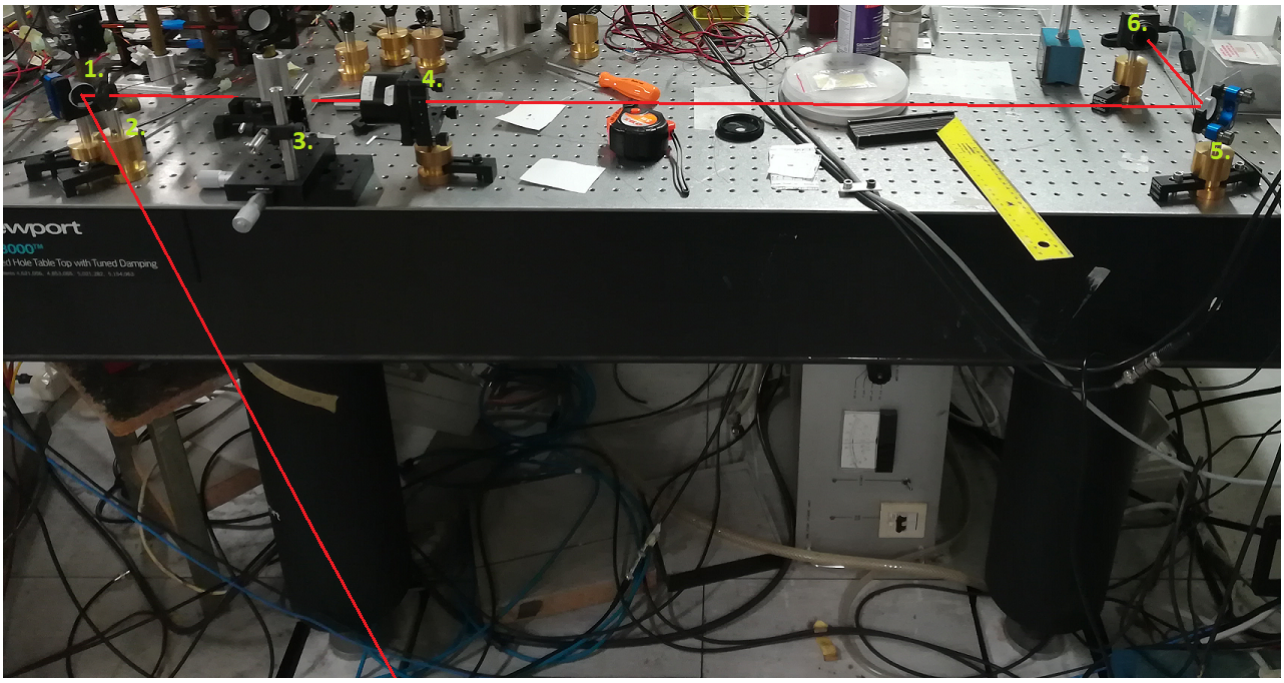

Figure 3.12: Experimental setup.

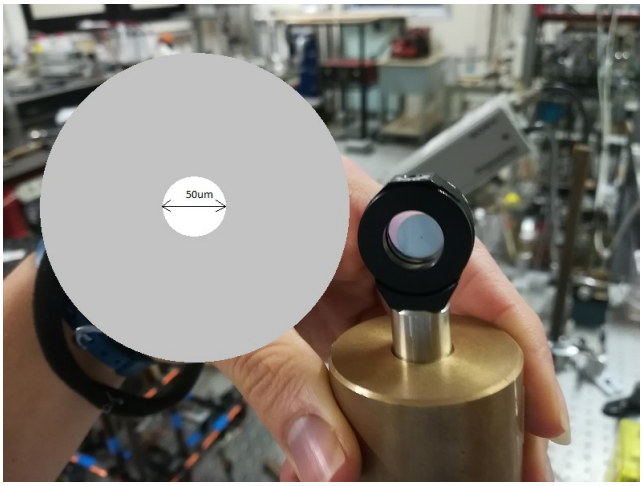

Figure 3.13: Spot target example.

- A multi-frequency grid distortion target. It is a Thorlabs distortion target featuring four arrays of horizontal and vertical lines spaced 10 μm, 50 μm, 100 μm, and 500 μm apart. This pattern is fabricated from the deposition of vacuum-sputtered, low-reflectivity chrome with an optical density (OD) of $\geq$3 at 430 nm on a 3 $\times$ 1 $\times$ 0.06 inches (76.2 mm $\times$ 25.4 mm $\times$ 1.5 mm) soda lime glass substrate. The dimensions of the glass substrate are the same as a standard microscope slide. Grid arrays are used to determine the distortion of an imaging system. Ideally, the horizontal and vertical lines of the grid should be perpendicular to each other. A distorted image will show the lines as bowed; this image can then be used to correct for distortion. It is shown in Fig. 3.14.

- An ultra fine square 2000 mesh grid from Ted Pella, Inc.They are made with precision

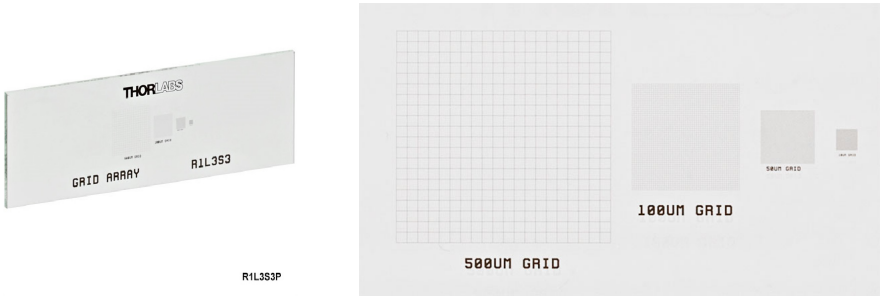

Figure 3.14: Thorlabs distortion target. Image taken from www.thorlabs.com.

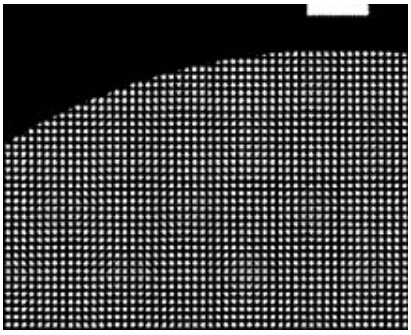

Figure 3.15: Gilder TEM grid, from Ted Pella, Inc. Image taken from www.tedpella.com

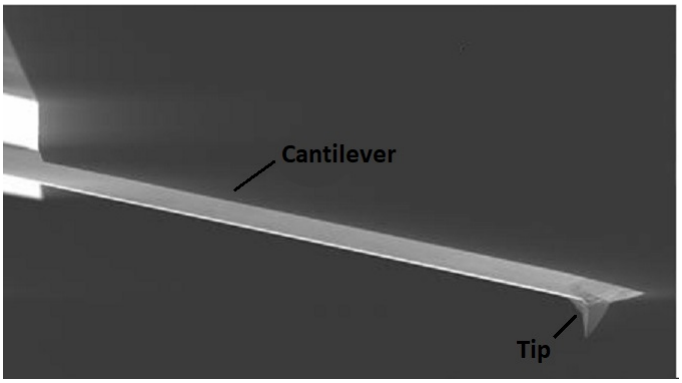

Figure 3.16: Tip of a Cantilever. Image taken from http://acoustics.org/pressroom/httpdocs/151st/Hurley.html.

electroplating technologies and support virtually every application with standard diameter of 3.05 mm. A nickel grid has been used with a thickness of typically 35(5) μm, pitch 12.5 μm, Hole Width 7.5 μm, Bar Width 5 μm. It is shown in Fig. 3.15.

- A tip of a Cantilever, usually used in AFM, shown in Fig. 3.16. Characteristics are fully reported in Fig. 3.17.

3.4.2 Theory of the optical system

An optical system is said to be 'diffraction limited' when it contains all its aberration inside the Airy disk. Therefore the Airy disk is the system resolution. It means that if we consider a geometrical point it will be focused into an Airy disk. The resolution res is defined according to the Rayleigh criterion, which states that two point sources are considered 'just resolved' if the

Figure 3.17: Cantilever Characteristics

principal diffraction maximum of one image coincides with the first minimum of the other. It is equivalent to define a minimum distance at which the points can be distinguished:

$$r = res = \frac{1.22\lambda}{2nsin\Theta} = \frac{0.61\lambda}{NA} \tag{3.13}$$

where λ is the wavelength, n is the refractive index of the media between the object and lens, Θ is half the angle of the light that enters the lens, NA the numerical aperture and the number 1.22 is related to the position of the first dark circular ring of the diffraction pattern and is obtained diving by π the first zero of the first order Bessel function of the first kind $J_1(x)$.

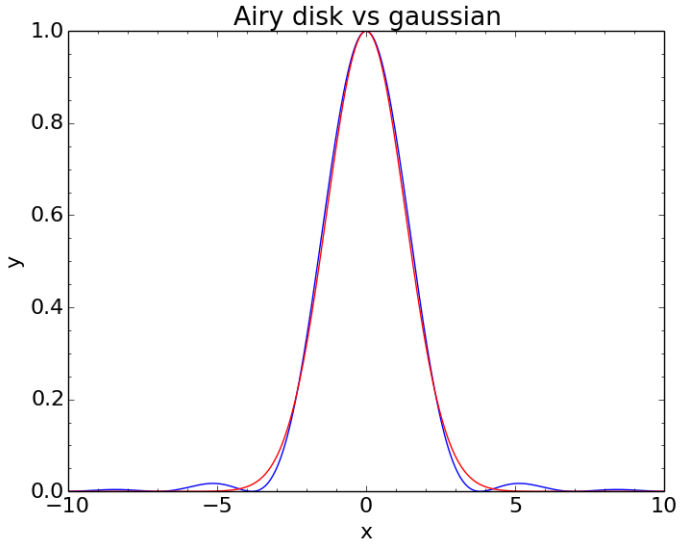

Figure 3.18: Gaussian curve approximating the Airy function

The Airy function of a resolved source is approximated with a gaussian curve, Fig. 3.18 and the resolution r is related to the gaussian σ by the relation:

$$\sigma = 0.35res \tag{3.14}$$

Where the gaussian function is defined as:

$$Ae^{-\frac{(x-m)^2}{2\sigma^2}} \tag{3.15}$$

A is the amplitude, m the centre and σ the width. The function describing the response of an imaging system to a point source is called Point Spread Function (PSF) and in our case we assume it to be the Gaussian function of Eq. 3.15.

If the object has a finite dimension the image is determined by the convolution between the PSF and the object function. This means that if the convolution is dominated by the object function then the system is resolved, otherwise is not.

The resolution of a system is however not only determined by lens characteristics, Eq. 3.13, but also by the aberration of the system. Aberrations are of two different types: chromatic and monochromatic aberrations. First ones are caused by the dependence on ω of the refractive index of lens. They can be divided into transverse (TCA) and longitudinal (LCA) ones depending on the axis where there is a different focal distance of the object. The LCA is usually corrected with the use of an Achromatic Doublet. It is a two lenses system with $n_1 \neq n_2$ that corrects the effect for at least two different wavelengths. Second ones are labelled with a wave front index due to how the aberration changes the ideal wave front. There is just a list of principal ones: Spherical aberration, Coma, Astigmatism, Curvature of field, Distortion.

3.4.3 Experimental procedure

Our setup consists in two lenses, one is a (variable) short focal length, placed at the focal distance from the object to be imaged, while the other is a plano-convex lens with long focal length (fixed, 1000 mm). This configuration has two advantages related to two different quantities:

- Magnification. It is the ratio between the size of the image and the size of the real object. In a two lenses configuration it is equal to the ratio of focuses: $f_{\text{tel}}/f_{\text{obj}}$ where f_{obj} is the focal length of the lens in front of the object and f_{tel} the focal length of the lens refocusing the image on the camera. It is thus obvious that in order to have a great magnification $f_{\text{tel}} \gg f_{\text{obj}}$ is necessary.
- Depth of field (DOF). The 'field' is defined as the area we want to image (thus we would like to be in focus). DOF is the depth of the effective focused area. It is related to the divergence of the imaging beam and thus to the Rayleigh length. We state intuitively that a longer(shorter) focal length corresponds to a longer(shorter) DOF. The short focal lens in front of the object implies then an accurate positioning of the lens (in our test system we fixed the lens and moved the target). On the other hand the long focal length allows a large uncertainty on the position of the camera.

We set the lenses into a tube so they were parallel to each other. We proceed as follows: first we align the laser on the camera closing the iris. Then we align the tube ensuring that the laser remains in the same point on the camera. In the end we put the target on a translation stage. The control of the retro reflection of each component is done in all the three steps. Having in mind the theory we took the image of different targets with different lenses and then analysed them.The different short focal lenses we tried are:

1. Achromatic Doublet (75 mm focal length)
2. Aspheric lens (60 mm focal length)
3. Plane lens(7 5mm focal length.)

A qualitative idea of the resolution of the different configurations is give in Fig. 3.19, where a few example of acquired images are reported. Both telescopes built with the aspheric and the plane

lens do not resolve the grid. Fitting the periodic pattern with an erf, error function, with fixed extreme (convolution between a gaussian and the subtraction of two Heaviside functions), we find a resolution of almost 6 μm. For the telescope built with the achromatic doublet, on the other hand, we measure a resolution of $\lesssim 2$ μm. The imperfection of the zoomed image can be attributed to the thickness of the target or a residual tilt. We thus identify this last telescope to be the best for our purpose, with a resolution close to our goal. Such an high resolution imaging system will be soon implemented on our experimental setup.

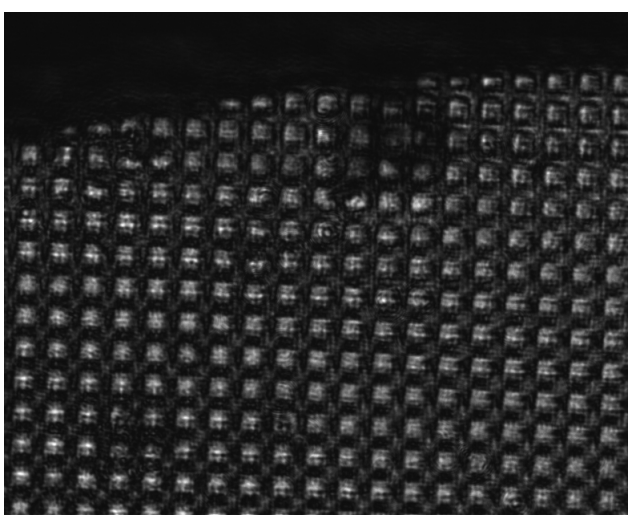

(a) Aspheric lens

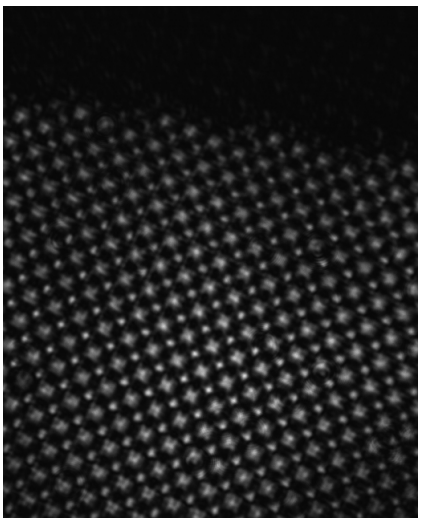

(b) Plano-convex lens

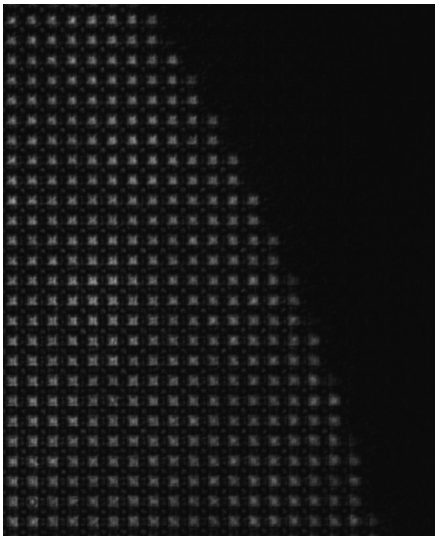

(c) Achromatic doublet

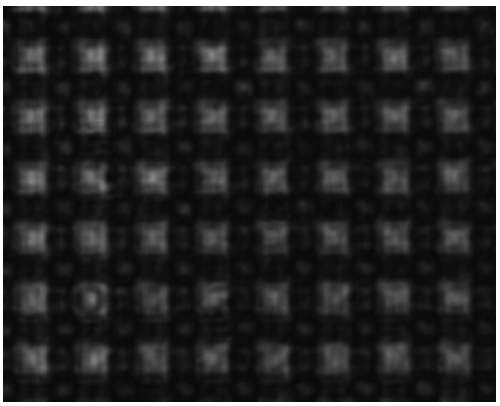

(d) Achromatic doublet zoom

Figure 3.19: Images of a grid (Hole Width 7.5 μm, Bar Width 5 μm) with different lens systems. **a**. Aspheric lens **b**. Plano-convex lens **c**. Achromatic doublet. **d**. Zoom of a picture taken with an achromatic doublet.

Chapter 4

Observation of a rotonic 'stripe phase'

The central result of this thesis is the observation of a peculiar regime of Dy dipolar gas (see Fig. 4.2). It is attained, through a phase transition, starting from a standard BEC and going into its unstable regime by progressively reducing the value of the scattering length a_s. We will show that the system evolves towards a so called rotonic 'stripe phase' and eventually to a so called 'droplet phase'. The characterization of the former phase is the key result of this thesis.

Since a dipolar condensate is employed in our experiment, its excitations are characterized by a roton spectrum, see Sec. 1.4.2. A lot of theoretical work has been done on roton modes and on roton instabilities [25, 26]. Of particular interest is the study of the ground state of the system when the roton gap tends to zero. A recent work, using numerical simulations, found that the ground state of such a system is a self-ordered coherent phase, a 'stripe-phase' [30]. Such a phase is very interesting as it is associated with a new state of matter: supersolidity [31, 81]. It was supposed to be formed by an array of droplets [30]. However experimental investigations reveal that the droplets do not have any relative coherence, probably because of the finite temperature [30].

The first section of the present chapter describes the appearance of a periodic structure in the momentum space in the instability region of a dipolar condensate. We interpret our observation as a 'stripe phase' due to a roton-instability. To validate this hypothesis different analysis are performed. Methods are extensively described in the second section while results are discussed in the third section. Here we will not discuss whether if this stripe phase is the ground state of the system or not.

The stripe phase exists for a specific range of magnetic field value. Going to lower values we observed features recognized as droplets. The link between stripe phase and droplets is thus considered. In the end also the observation of an hysteresis is discussed.

4.1 Instability observations

Our purpose is to study the instability region of a condensate of Dy atoms; in particular we decided to reproduce the roton-mode experiment with Er atoms [26] with our system. Two main features distinguish our experiment from the previous one: the element and the trap. Because of the dipolar nature of Dy, the instability is reached lowering a_s close to a Feshbach resonance. Thanks to the high value of Dy magnetic moment, however, when the system gets to the unstable regime, it is still not heavily affected by three-body losses. A long lived sample is then expected in contrast with the Er case, allowing the study of an instability dynamics. Traps employed in Ref. [26] are cigar-shaped, i.e. tightly bound in two directions. On the contrary, we use a trap that is tightly confined only along the polarization axis. In the x, y plane one direction is more confined than the other, but still the confinement is relatively weak allowing a dynamics of the instability in both directions.

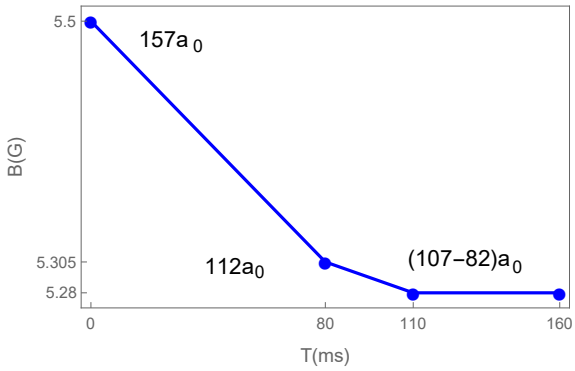

Figure 4.1: Sketch of the linear ramps used in our experiment. The BEC is achieved at $B = 5.5$ G. Then B is linearly ramped to the value $B = 5.305$ G in 80 ms. A second linear ramp brings the system in the instability region $B = (5.29 - 5.26)$ G in 30 ms. At the end of the ramp the system is held in the unstable regime for a variable interval of time (e.g. 50 ms), to let it evolve. The trap is then released and an image taken.

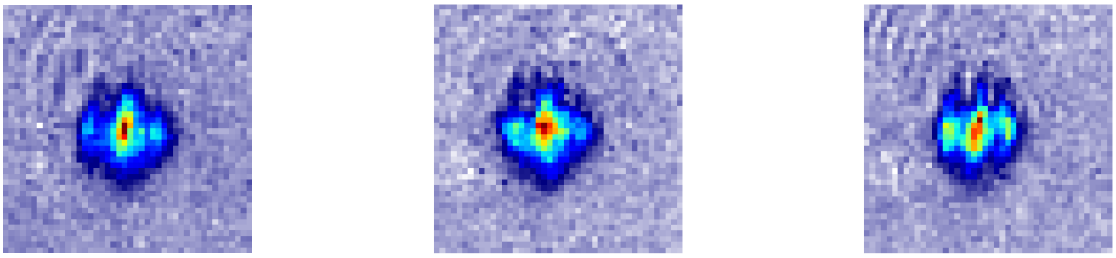

(a) N $\sim$ 34000 (b) N $\sim$ 41000 (c) N $\sim$ 39000

Figure 4.2: Three different realizations of a stripe phase, i.e. a modulated state in a roton instability region, in the momentum space. Images are taken at $B = 5.279$ G after an evolution time of 8 ms and a 62 ms time of flight (TOF). The interference pattern is reproducible shot-to-shot.

We tune the scattering length by using two Feshbach resonances at around 5.1 G, see Sec. 3.2. The magnetic field $B_{\rm Fesh}$ is changed with two consecutive linear ramps shown in Fig. 4.1. The condensate is initially created at $B = 5.5$ G, where $a_{\rm s}$ is close to the background value $a_{\rm bg} = 157(4)a_0$. The magnetic field is subsequently changed to $B = 5.305$ G ($a_{\rm s} = 112a_0$, according to our estimate of $a_{\rm s}$) with a linear ramp in 80 ms. We use a second 30 ms linear ramp to enter the unstable regimes, reaching a final value of the magnetic field ranging in the interval $B = (5.26 - 5.29)$ G. After a variable waiting time at the final magnetic field, we switch off all dipole traps and we take an absorption image of the atoms after 62 ms of free fall.

For $a_{\rm s} \leq 110a_0$ after 8 ms we see the appearance of lateral peaks along the weak trap axis, see Fig 4.2. This is a signature of a density modulation of the atoms along this weak trap axis. Such a profile is very similar to the one shown in Fig. 1.16 and is quite reproducible from shot to shot.

Going deeper into the unstable regime the appearance of a different pattern is observed. It is randomly changing from shot to shot as it is shown in Fig. 4.3. Typical manifestation of the instability and its subsequent dynamics is shown in Fig. 4.4 for systems with initial atom number $N \simeq 4 \times 10^4$. For a limited magnetic field range below the stable region we observe the appearance of small side peaks. Such feature persists up to about 100 ms and then a BEC is recovered. For smaller magnetic field values two side peaks appear also along the tighter trap axis

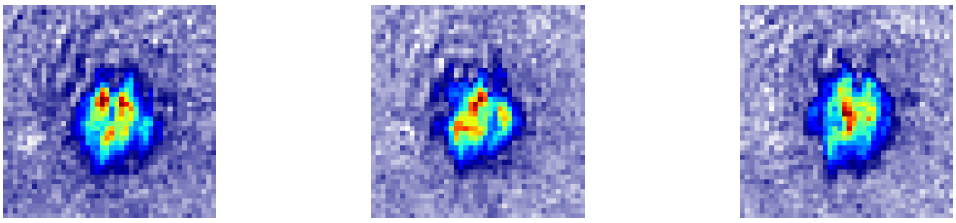

(a) N ∼ 34000 (b) N ∼ 35000 (c) N ∼ 35000

Figure 4.3: Three different realizations of quantum droplets in the momentum space. Images are taken at $B = 5.272$ G after 8 ms evolution time and 62 ms time of flight (TOF). Atom number for each sample is reported. The interference pattern variates remarkably from shot-to-shot.

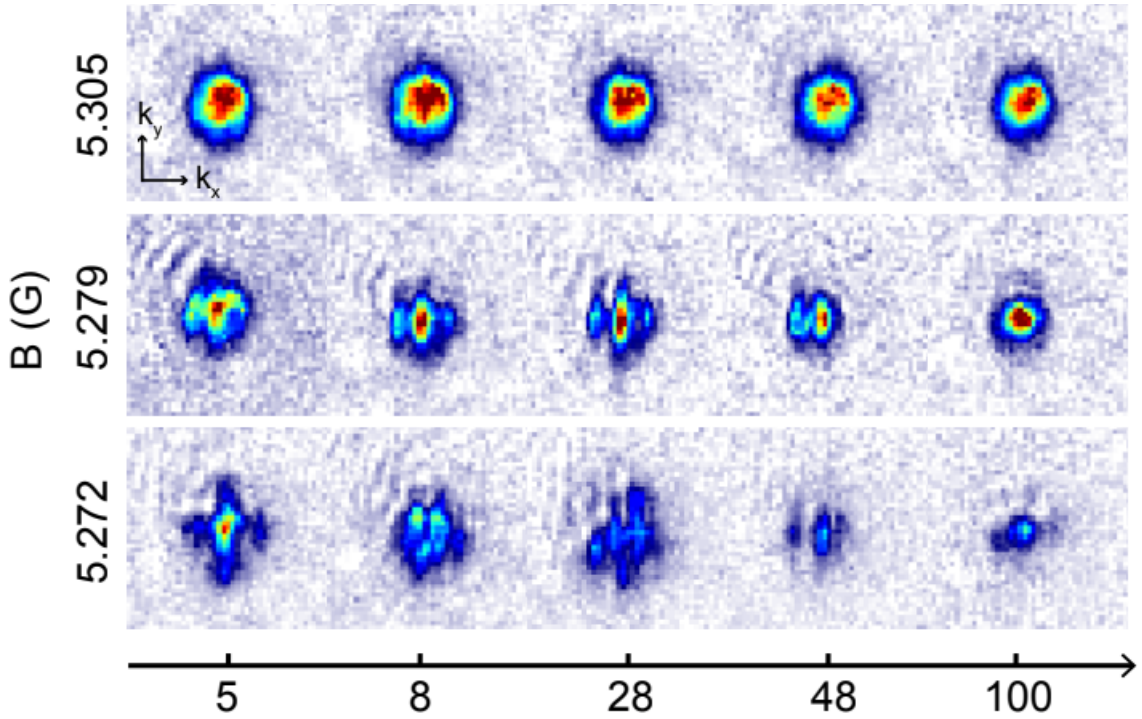

Figure 4.4: Typical Time-of-Flight images of the momentum distribution $\tilde{n}(q_x, q_y)$ for different evolution times in three regimes: (top) $B = 5.305$ G, stable BEC; (middle) $B = 5.279$ G, stripes along the weak axis x; (bottom) $B = 5.272$ G, droplets in the (x,y) plane. Since the imaging process is destructive, each image represents a different experimental realization.

y. After few ms, however, a more complex interference patterns is observed, with maxima and minima distributed irregularly in the (q_x, q_y) plane. At longer times we observe small condensates with relatively large thermal fractions.

While the third regime, shown in Fig. 4.4, is recognized as the well studied quantum-droplets regime, the second one deserves some comments. It is not a roton mode, as the 'roton' is the mean-field stable quasi-particle with a real value of the gap $\Delta_{\rm rot}$. But it is also different from the subsequent droplet regime. We called this different state a rotonic stripe phase. In next sections experimental procedures performed in order to analyse this peculiar feature are discussed as well as experimental results.

4.2 Analysis procedures

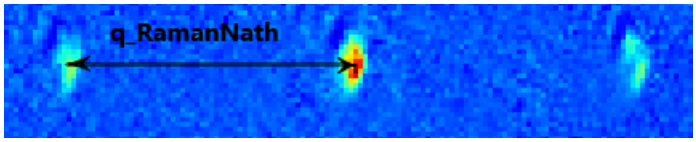

Figure 4.5: Momentum distribution of the resonator lattice populated by a $\lambda = 1064$ nm laser pulse. $q_{\rm RN}$ represents the distance between two consecutive peaks.

For each magnetic field and evolution time we recorded between 30 and 70 time-of-light images, obtained by absorption imaging. Each image is cropped 50×50 pixel around the sample and rotated by a fixed angle (18°), such that the modulation axis corresponds with the horizontal x axis. From this rotated image we extract two 1D profiles, $\tilde{n}(q_x)$ and $\tilde{n}(q_y)$ by integrating over the vertical and horizontal directions, respectively.

Momentum recorded are expressed in [pixel] unit. The conversion from [pixel] to $[\mu m^{-1}]$ is done by calibrating the system with a Raman-Nath pulse of the resonator standing wave with $\lambda = 1064$ nm [82]. The pulse transfers the population of the sample to a finite momentum $q_{\rm RN}^{th} = 4\pi/\lambda$. The absorption image after a 62 ms free expansion is shown in Fig. 4.5. The conversion from [pixel] to $[\mu m^{-1}]$ is then

$$[\mu m^{-1}] = \frac{[\text{pixel}]10^3 4\pi}{\lambda[nm] \times q_{\rm RN}[\text{pixel}]}[\mu m^{-1}] \tag{4.1}$$

where $q_{\rm RN}$ is obtained from a three-gaussian fit: $q_{\rm RN}[\text{pixel}] = 59.4(0.2)[\text{pixel}]$.

At small enough magnetic fields, the system can display a uniform or a modulated (stripe or droplet) density profile, depending on the atom number. Because of the 20% atom number fluctuation of our system a preliminary distinction between uniform sample, i.e. BEC and the non-uniform modulated sample is necessary. In order to distinguish between uniform BEC and stripe/droplet we perform a first gaussian fit on $\tilde{n}(q_x)$, extracting the gaussian size σ_{gauss}. The distinction is operated comparing σ_{gauss} with the average gaussian width $\bar{\sigma}$ (with dispersion Δ) for a dataset of stable BECs, realized at B = 5.305 G. For $\sigma_{gauss} \leq \bar{\sigma} + \Delta$ the sample is considered a uniform BEC, otherwise it is a modulated state. Methods for the analysis of such a modulated state is the subject of this section. It is divided as follows:

- First, we report the analysis for atom number. N is obtained by a pixel count and is very important for two aspects: the existence of a mean-field collapse point and the determination of the stabilization mechanism preventing such collapse.
- Second, we present a double slit model. It is used to obtain parameters such as stripe momentum and phase.
- Third, we introduce a three-gaussian fit. It is related to the contrast parameter, related to the population involved in the stripe phase.

4.2.1 Instability and number of atoms

The atom number is a very important quantity. As emphasized in Sec. 1.3.5 it is critical for the existence of a local minimum in the single particle energy function, thus for the existence of a metastable state for the system. Such a critical dependence of the instability on the atom number is qualitatively represented in the N-B plane (atom number vs external magnetic field) using a phenomenological observable.

N is strictly related not only to the existence of the instability but also to the stabilization mechanism. As for the droplet (see Sec. 1.5.2), there are two possibilities for such mechanism: quantum fluctuations (BMF effects) and three-body scattering, i.e. the real part of three-body interactions. Both are characterized by a density dependence: quantum fluctuations introduced an energy correction $\propto n^{5/2}$ [27], while three-body scattering $\propto n^3$ [50]. It follows that by adding to the Gross-Pitaevskii equation, within the Thomas-Fermi approximation, an interacting term representing one or the other correction, different density distributions are obtained. Quantum droplets are stabilized by quantum fluctuations, thus a system stabilized thanks to this BMF effect, has a typical density of the order of $3(1.5) \times 10^{20}$ m^{-3} [28]. The density of the system can be estimated from the N decay rate using equation (see Sec. 1.3.3)

$$\frac{1}{N}\frac{\mathrm{d}N}{\mathrm{d}t} = \frac{1}{6}K_3\langle n^2\rangle \tag{4.2}$$

Since the decay rate is related to the density distribution involved in the stabilization mechanism, the study of N vs t is of fundamental importance for the understanding of the stripe phase phenomenon.

The atom number is determined quantitatively and independently of any fitting procedure, by evaluating the zeroth moment of the images: $N = M_{0,0} = \sum_{\mathrm{x,y}} n_{\mathrm{c}}(x,y)$, where $n_{\mathrm{c}}(x,y)$ is the (x,y) pixel column density. Actually a background value has to be removed from n_{c}. The final image is in fact obtained from the subtraction of two images in order to remove the background light due to the lasers. Such images are taken after an exposition time of respectively $t_1 = 35$ms and $t_2 = 39$ms in order to avoid the ratio to have negative value (this is necessary for a correct digital interpretation of the ratio by the acquisition program). This implies a non perfect compensation and the presence of a non perfectly zero background. Fitting the integrated profile $\tilde{n}(q_{\mathrm{y}})$ with a gaussian curve, such background is evaluated as the offset of the gaussian. In the end $N = \sum_{\mathrm{x,y}}(n_{\mathrm{c}}(x,y) - (\mathrm{offset} \times \mathrm{crop_x})$, where $\mathrm{crop_x}$ is the number of pixels in the integrated x direction and $\mathrm{crop_x} = \mathrm{crop_y} = 50$ since a square crop has been done.

A phenomenological observable in the (N, B) plane

A stable BEC has a momentum distribution that in the Thomas-Fermi approximation is an inverted parabola. For simplicity a gaussian fit of the integrated profile of the momentum distribution $\tilde{n}(q_{\mathrm{x}})$ is usually performed to characterize the system as it well approximates the experimental curve, see Fig 4.6. The 'stripe phase' on the other hand is characterized by a modulated profile. The difference between the two curves is a signature describing the state of the system and drawing a line between stable and unstable regime. A phenomenological observable has been introduced to qualitatively describe such differentiation. It is the Mean Squared Deviation (MSD) of the momentum distribution from a gaussian, normalized to the gaussian area. To optimize the procedure the MSD is calculated both for the vertical (y) and the horizontal (x) distribution, $MSD = \sqrt{\mathrm{MSD}_{\mathrm{x}}^2 + \mathrm{MSD}_{\mathrm{y}}^2}$. The expression for the $\mathrm{MSD}_{\mathrm{x(y)}}$ is

$$MSD_{\mathrm{x(y)}} = \frac{\int[\tilde{n}(q_{\mathrm{x(y)}}) - g(q_{\mathrm{x(y)}})]^2 dq_{\mathrm{x(y)}}}{\int g(q_{\mathrm{x(y)}}) dq_{\mathrm{x(y)}}} \tag{4.3}$$

where $\tilde{n}(q_{\mathrm{x(y)}})$ is the 1D integrated profile $\int \tilde{n}(q_{\mathrm{x}}, q_{\mathrm{y}}) dq_{\mathrm{y(x)}}$ and g represents the gaussian distribution.

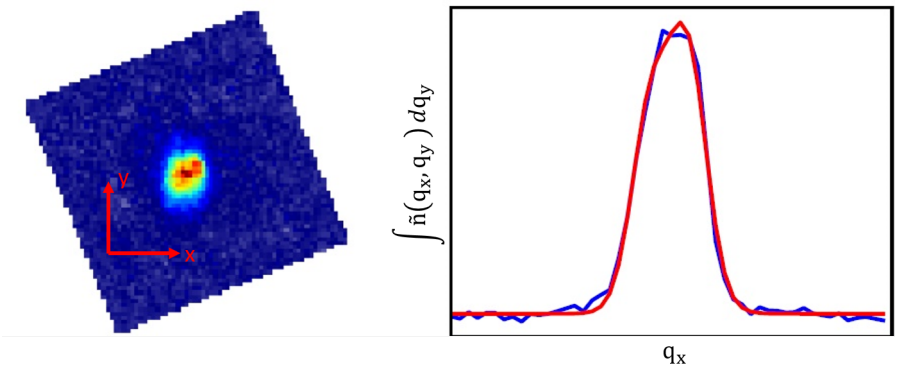

Figure 4.6: On the left image of a condensate is reported at $B = 5.295$ G with $N \sim 44000$ after 8 ms evolution time. On the right the integrated profile $\tilde{n}(q_x)$ is shown. It is qualitatively well approximated by a gaussian curve.

In order to produce an instability diagram, measurements are performed after a fixed evolution time of 8 ms. They are carried out taking advantage of the natural atom number fluctuation of the system. When necessary also the red laser capture ability has been decreased, reducing the frequency modulation during the loading of the MOT, in order to decrease the atom number. For each magnetic field B_{Fesh} the widest possible range has been explored, but the measurements are however limited by the small control on atom number. A gaussian fit is then performed on the 1D profile, $\tilde{n}(q_{x(y)})$. To avoid that narrower peaks are identified as gaussian shape, leaving out the lateral peaks, it is imposed the condition that for $N \geq N_{\mathrm{inf}}$ it should be $\sigma_x \geq \sigma_{\mathrm{gauss}}$. The parameter N_{inf} is chosen arbitrarily at around 15000 atoms, σ_{gauss} is the σ of a uniform BEC with $N \sim N_{\mathrm{inf}}$. The phase marker $\mathrm{MSD}_{x(y)}$ is then obtained as the mean square deviation between the experimental curve and the gaussian fitted curve. To avoid the noise due to the difference between image background and tail of the distribution, the mean square deviation has been calculated considering just a portion of width $\pm M \times \sigma_x$ of the experimental profile and fitted gaussian. It is equivalent to assume

$$\int_{-\infty}^{-M\sigma_x} \tilde{n}(q_x) - g(q_x) \quad = \quad \int_{M\sigma_x}^{\infty} \tilde{n}(q_x) - g(q_x) = 0 \tag{4.4}$$

$$\mathrm{MSD}_x = \int \frac{[\tilde{n}(q_x) - g(q_x)]^2 dq_x}{g(q_x) dq_x} \quad = \quad \int_{-M\sigma_x}^{M\sigma_x} \frac{[\tilde{n}(q_x) - g(q_x)]^2 dq_x}{\int g(q_x) dq_x} \tag{4.5}$$

$M = 2$ has been chosen to maximize the curve difference so

$$MSD_x = \sqrt{\frac{\sum(\tilde{n}(q_x) - g(q_x))^2}{2\sigma_x A_x^2}} \tag{4.6}$$

where A_x is the gaussian amplitude. The same holds for MSD_y. We do not associate any error to this qualitative parameter, since there are too many sources of uncertainties in the complete procedure. The reliability of the parameter is tested with the realization of an histogram of the MSD distinguishing between uniform BEC data set and non-uniform modulated data (see Sec. 4.3.1).

4.2.2 A double-slit model

As discussed in Sec. 1.4.2 the roton mode corresponds in coordinate space to a density modulation of the condensate. The roton instability can be thought as a digging of such modulation [83]. The free expansion of such a system corresponds then to a multiple slits experiment. Estimating

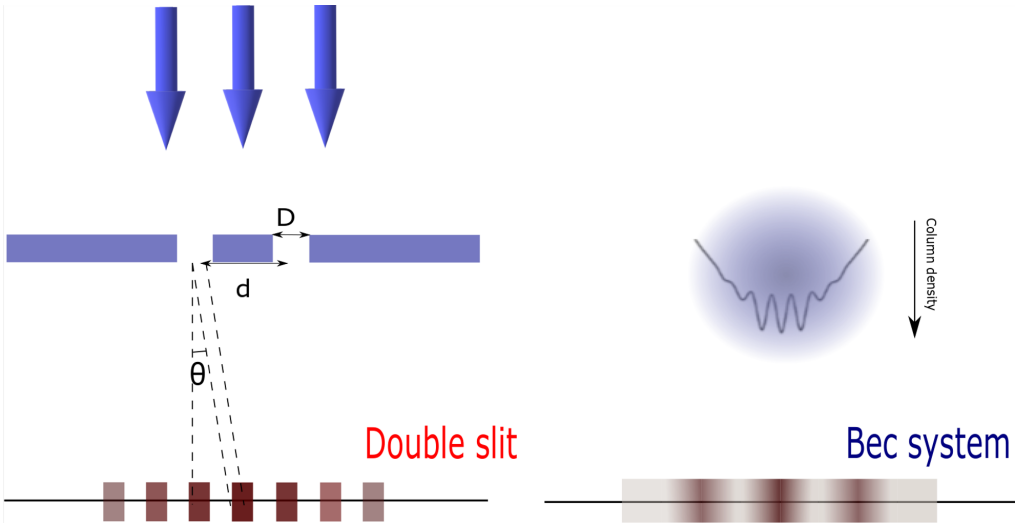

Figure 4.7: Left image represents a double slit system scheme. d is the distance between the two slits and is related to the interference pattern. D is the width of the slit and is related to the diffraction pattern. The number of slits n is related to the number of orders visualized combining the two patterns. θ is the relative angle between the propagation direction of the incoming beam and the diffracted light. Right image represents our system. Absorption image of the sample gave a pattern similar to that of a double slit.

q_{rot} and the extension of our atomic system with a variational method we expect between two and four peaks since the modulation tends to be confined at the centre of the sample where the density is maximum. Our current resolution prevents us from estimating if more than two stripes are present (see Sec. 4.3.4) so a double slit model is used.

Our observable $\tilde{n}$ is given by the product of the column density of the system times the cross section (see Eq. 2.45). The density modulation together with the coherence of the condensate, produces in momentum space a pattern similar to the diffraction pattern geometry in two (or more) slits irradiated by a plane wave [82]. This pattern is obtained by the superposition of an interference pattern and a diffraction pattern $I_{\mathrm{f}} = I_{\mathrm{diffr}} I_{\mathrm{interf}}$. A two-point-sources interference pattern fixes the position of the fringes

$$\frac{I_{\mathrm{interf}}}{I_0} = \cos^2\left(\frac{\pi d \sin(\theta)}{\lambda}\right) \tag{4.7}$$

while the single slit diffraction pattern modulates the peak amplitude

$$\frac{I_{\mathrm{diffr}}}{I_0} = \frac{\sin^2\left(\frac{\pi D \sin(\theta)}{\lambda}\right)}{\left(\frac{\pi D \sin(\theta)}{\lambda}\right)^2} \tag{4.8}$$

where d is the relative distance between the slits, D is the single slit width and θ the propagation angle of the scattered light with respect to the incident beam. A scheme of our system and of an analogous double slit model is sketched in Fig. 4.7. The resulting pattern is shown in Fig. 4.8. Nevertheless our system shows some differences with a perfect double slit:

- Instead of rectangular slits with defined edges we have atoms with an approximately gaussian modulation. Diffraction function is then approximated with a gaussian.
- The modulation can start not exactly in the centre, but slightly displaced from the centre. It implies a modulation with a non zero velocity. This possibility is taken into account by a

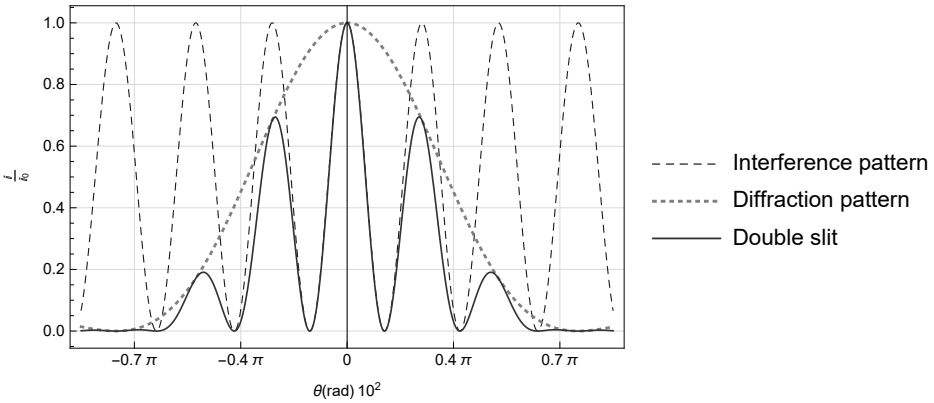

Figure 4.8: The interference pattern of a $\lambda = 421$ nm radiation incident on a double slit is shown. Double slit characteristics are: $d = 3$ μm (relative distance between slits) and $D = 1$ μm (single slit width). Dashed line represents the interference pattern of a two point sources at relative distance d. Dotted line represents the diffraction pattern of a single slit of width D. Continuous line represents the product of the first two and is the double slit pattern.

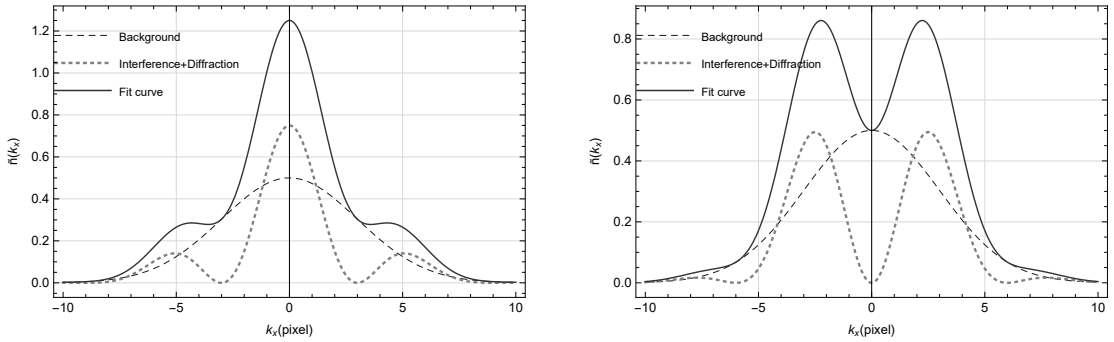

(a) Background, double slit and fit function for $\phi = 0$

(b) Background, double slit and fit function for $\phi = \pi/2$

Figure 4.9: The fitting function is represented for the value of $q_{\text{rot}} \sim 6$ [pixel] and two different phases. **a**. $\phi = 0$. **b**. $\phi = \pi/2$. The fitting function is obtained as the sum of a background gaussian, represented as a dashed curve, and a double-slit function represented in dotted line.

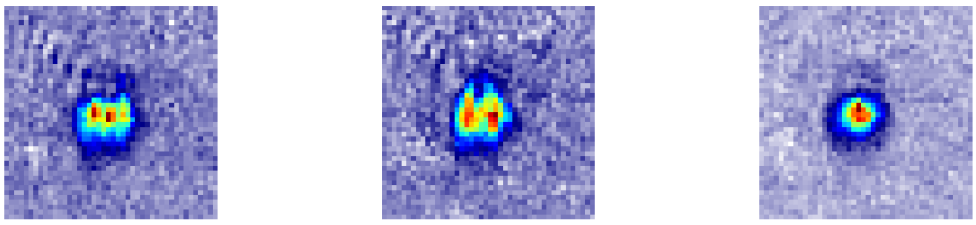

(a) 48 ms. (b) 58 ms. (c) 100 ms.

Figure 4.10: Images of the momentum distribution of a system at $B = 5.28$ G after different evolution times. **a**. Three peaks are visible. **b**. Stripe phase pattern with a phase $\phi = \pi/2$. **c**. A small condensate.

phase in the interference pattern. It is analogous to think about the two slits with a relative phase due to different refractive index.

- Since the modulation does not affect all the system, an approximately gaussian background is present. This is taken into account with a gaussian term summed to the interference pattern. We note that it implies that the fringes never go to zero, the fit function has no zeros, and the contrast is limited.

The fitting curve is then given by the sum of two gaussians with equal σ, but different amplitudes. One gaussian is modulated with an interference pattern

$$\tilde{n}(k_\mathrm{i}) = Ae^{-\frac{(k_\mathrm{i}-q_0)^2}{2\sigma^2}}\left[1 + A_1\cos^2\left(\frac{\pi}{k_\mathrm{krot}}(k_\mathrm{i} - q_0) + \phi\right)\right] \tag{4.9}$$

where q_0 is the centre of the gaussians and q_rot is the roton momentum, related to d relative distance between density modulation peaks in real space, see Fig. 4.9.

The modulated state is analysed using Eq. 4.9 with $i = x, y$. Three time scales have been recognized in the stripe regime. *Short times*, corresponding to the phase stabilization, *Intermediate times*, corresponding to the stationary phase and *Long times*, corresponding to the decay phase.

Short time analysis includes the interval (0 ms, 6 ms), where 0 ms indicates the end of the second magnetic field linear ramp, see Fig. 4.1. The structure is not completely formed and the appearance of small peaks is observed. The fit tendency is thus to arrange with small q_rot and a non zero phase. Such a fit is artificial as it works also on a gaussian curve adjusting the parameters. Bounds are then introduced on q_rot to have a reasonable fit: $q_\mathrm{rot} \in (1 - 1.4)\ \mu\mathrm{m}^{-1}$ where the conversion in Eq. 4.1 has been used. The limits are centred around the mean value of q_rot in the intermediate stage.

Intermediate times analysis applies in the range 6 ms to $\sim$ 35 ms. The stripe phase is completely formed in the sense that maximum contrast is reached and kept constant as we shall see following section. Parameters are left unbound, but unreasonable values are discarded: $0.8\ \mu\mathrm{m}^{-1} < q_\mathrm{rot} < 2\ \mu\mathrm{m}^{-1}$ are acceptable. Long times analysis is about all the data set with time evolution >35 ms. Different structures from the previous ones are observed. Examples are shown in the images of Figs. 4.10a, 4.10b. The parameters are left unbound and a general tendency to smaller q_rot is observed. For very long times small condensates with relatively large thermal fractions are recovered as shown in Fig. 4.10c, thus fitted with gaussian curves.

A similar time scale distinction is operated for the droplets regime. Short times correspond to the formation phase of droplets. We observe a very peculiar feature. Lateral peaks appear also in the y direction (see Fig.4.4). We speculate of a two-dimensional instability leading to multiple

droplets formation. The observed pattern is analysed with the double slit model using the fitting function in Eq. 4.9 along both axes.

Intermediate times correspond to the droplet phase. The appearance of interference patterns along y suggests that droplets self-arrange in the (x, y) plane, as previously observed in cylindrically-symmetric traps [29]; however due to the lack of mutual phase coherence [30], the interference pattern we observe is much more complex than distributions observed previously. The analysis on such patterns is only qualitative since the quantum droplets have been already widely studied [28, 29, 46, 48, 49].

The decay of quantum droplets in then observed at long times. Roton features, i.e. lateral peaks along the x axis, are eventually recovered as well as a small condensate with a large thermal fraction background.

4.2.3 A three gaussian fit

How do we define a formation and persistence time scale of the stripe phase quantitatively? Following Ref. [26] a contrast parameter C is defined. The momentum profile is fitted with three gaussians, a central one of amplitude C and two side ones of equal amplitude C_1, spaced by k_{x} roton momentum. The contrast is defined as the ratio C_1/C. It describes the population participating at the process, being related to the population transferred to the state with a non-zero momentum. Therefore it allows an estimation of the formation time of the stripe phase and how much it lasts.

Such a quantity is calculated both for BECs, to define a contrast background, and for the stripe phase. In the case of BECs a direct three-gaussian fit is performed on experimental data with the function

$$\tilde{n_{\mathrm{x}}} = Be^{-\frac{(q_{\mathrm{x}}-q_0)^2}{2\sigma_{3\mathrm{g}}^2}} + B_1 e^{-\frac{(q_{\mathrm{x}}-q_0\pm q_{\mathrm{rot}})^2}{2\sigma_{3\mathrm{g}}^2}} \quad . \tag{4.10}$$

With the lateral peaks fixed at $q_{\mathrm{rot}} = 1.2\ \mu\mathrm{m}^{-1}$ contrast values compatible with zero are found. For the stripe phase, instead, a two step fit is used. First the double slit model is exploited to extract the parameters as described above. Secondly the double slit fitting function is reconstructed with the corresponding fitted parameters, but with a $\phi = 0$ phase whether or not the original one. A curve like the one in Fig. 4.9a is recovered and fitted with Eq. 4.10. The contrast is then defined as the ratio B_1/B. It would have no sense for the droplets regime since nor the double slit model nor a three gaussian function fit its momentum distribution.

4.3 Results

We have previously mentioned the observation of a stripe phase. A qualitative study of the instability can be done in the (N, B) plane with the MSD. Formation and persistence of the phase is instead demonstrated using a contrast parameter. Since it exists in a mean-field unstable regime a stabilization beyond mean field effect has to be found. Such a mechanism can be understood studying the atom number rate of decay. In the end characteristic properties such the typical length scale, related to the roton momentum, and the phase coherence can be investigated employing a double slit model.

4.3.1 Phase diagram in the (N, B) plane

In the end of the Sec. 4.2.1 we have mentioned the need of an histogram, in order to verify the reliability of the MSD parameter. If the distinction made between uniform BEC data set and non-uniform modulated data is clear enough, then the MSD is a good parameter. Fig. 4.11 shows an almost complete separation between the two. A discriminator between the two phases is recognized from the histogram to be at around 0.17. Graph B vs N is then shown in Fig. 4.12

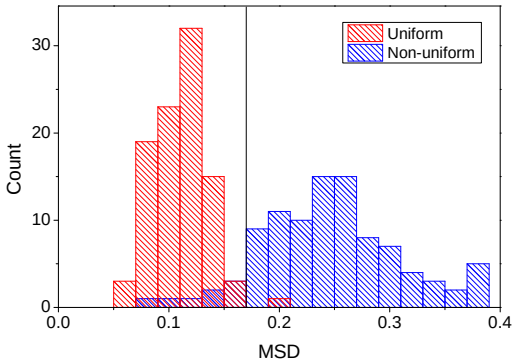

Figure 4.11: Histogram of the mean square deviation (MSD) for BEC samples (uniform) and stripe/droplet ones (non-uniform). A discriminator around 0.17 is recognized.

with a colour map (normalized) to highlight the separation between uniform BEC and modulated states.

The black solid line in the graph is obtained by a variational model using a Thomas-Fermi density function that will be treated in Sec. 4.3.4. Note that all the previous treatment attributes observations to a roton instability as they represent the transfer of a population to a state with well defined non zero moment. The implied assumption is that a roton instability happens before a phonon instability. This is why we employ such a roton model following Ref. [26]. The relation between the density peak n_0 and the atom number N is

$$n_0 = \frac{15}{8\pi}\frac{N}{R_\mathrm{x}R_\mathrm{y}R_\mathrm{z}} \tag{4.11}$$

where R_i are the Thomas-Fermi radii. From the roton gap expression $\Delta = \sqrt{E_0^2 - E_1^2}$, where the energies are explicitly written in Eqs 4.16 and 4.15, the instability implies $E_0^2 = E_1^2$. Substituting the peak density of Eq. 4.11 in the explicit expression for $E_0^2 = E_1^2$ an instability demarcation line is obtained

$$\frac{3}{10}\frac{a_\mathrm{dd}}{(a_\mathrm{dd} - a_\mathrm{s})^2}\frac{R_\mathrm{x}(R_\mathrm{y}^2 + R_\mathrm{z}^2)}{R_\mathrm{y}R_\mathrm{z}} \tag{4.12}$$

Such equation is clearly not self-consistent, given the original assumption of negligible confinement along x, so it cannot be used to derive exact predictions. Thomas-Fermi radii are determined for different N values with a variational method including beyond-mean field effects [46]. The line in the graph is then obtained provided the conversion between scattering length a_s and magnetic field B given in Fig. 3.10. Note that according to this stability diagram, we expect the progressive reduction of N at constant B to bring the system back into the BEC region. This aspect shall be further commented in the next section for the stripe phase. Apparently, also a system initially prepared in the droplet regime tends to lose atoms due to three-body losses, moving back to the BEC regime. Evidences of this behaviour are not only the appearance of a BEC at long times, but also the recovery of one-dimensional stripes at intermediate times (see Fig. 4.4).

4.3.2 Rate of decay

Mean-field theory predicts a collapse in the region where we observe the 'stripe phase'. Such as in the droplet case a beyond-mean field effect has to be taken into account to explain the absence of such collapse. We identify quantum fluctuations as the stabilization mechanism by comparing the decay rate of the 'stripe phase' with the one of quantum droplets.

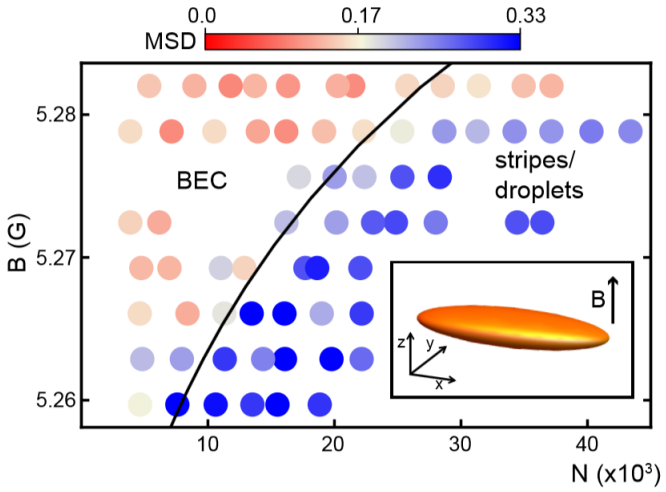

Figure 4.12: Evolution of the mean squared deviation (MSD) of $\tilde{n}(q_x, q_y)$ from a gaussian, distinguishing BEC, and stripe/droplet regions in the (N, B) plane. The black line represents the theoretical prediction for the roton instability. Inset: trap geometry.

In the previous sections all the necessary ingredients were provided. The link between the nature of the stabilization mechanism and the density was introduced in Secs 1.5.1, 1.3.3. The relation between density and the observable N is expressed in Eq. 1.51. Method for N measurement has been described in Sec. 4.2.1. N measurements are now reported. In Fig. 3.11 the condensate lifetimes is represented. Typical time scale is $\tau_{\mathrm{BEC}} = 500$ ms. Fig. 4.13 shows the evolution of $N(t)$ for stripes (blue) and droplets (red). Both scenarios feature an initial loss on time scale much faster that the one of a BEC. It follows a much slower decay.

We associate a high density component to the faster decay, while a low density one comparable to a BEC to the slow decay. The mean density is then obtained considering two component sample with the fit function

$$N(t) = \Delta N e^{-\frac{t}{\tau}} + N_0 \tag{4.13}$$

where N_0 is the initial low density component atom number, ΔN is the atom number participating at the high density component and decaying in a time τ. For the stripe phase $\tau_{Stripe} = 23(12)$ ms was found,while $\tau_{\mathrm{Droplet}} = 24(10)$ ms was extracted for quantum droplets. The comparable τ_{Droplet} and τ_{Stripe} demonstrate that the mean density is the same for both phenomena as well as the stabilization mechanism. Measurements of the recombination constant K_3 were presented in Sec. 3.3 $K_3 = 1.5(2) \times 10^{-27}\mathrm{cm}^6\mathrm{s}^{-1}$. Using the relation in Eq. 1.51 the mean density for both stripe and droplet is found: $n = 4 \times 10^{14}$ cm^{-3}. It is about a factor 10 larger than the calculated mean density of a BEC. The value found for droplets is in agreement with a previous experiment [28] and is the demonstration that stripe phase is quantum fluctuation stabilized as the droplet is. Different value of ΔN implies that a different portion of the system takes part to the high density phase.

The two phenomena of stripe phase and quantum droplets are thus stabilized by the same mechanism, i.e. the quantum fluctuations. But they are also seen as distinct phases of the system for different scattering length values. Furthermore the appearance of lateral peaks along the y direction at short times in droplet regime has been already mentioned. Based on this clues we speculate that the quantum droplet corresponds to a roton instability both along x and y directions.

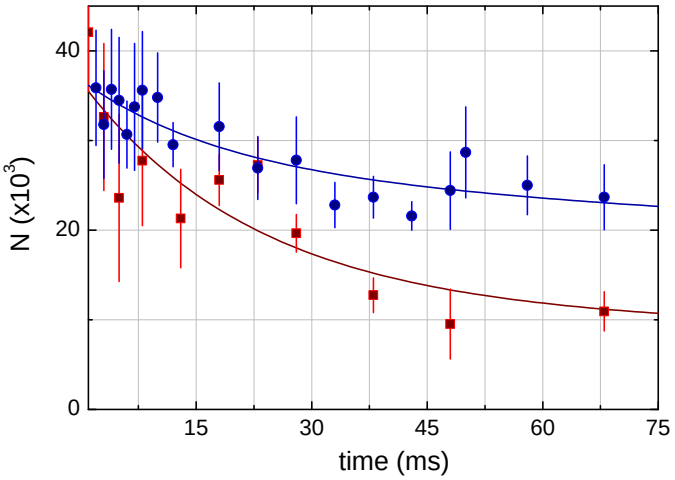

Figure 4.13: Time evolution of the atom number for stripes $B = 5.279$ G (blue circles) and droplets $B = 5.272$ G (red squares). Data are fitted by exponential function, Eq. 4.13.

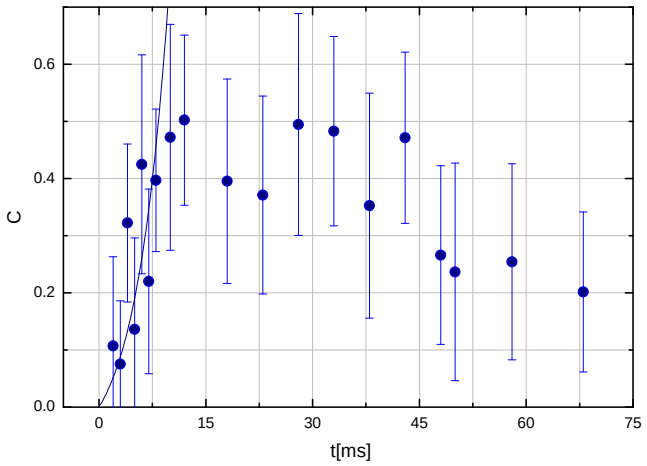

Figure 4.14: Time evolution of the contrast in the stripe regime $B = 5.279$ G. The initial data ($t < 10$ ms) are fitted with an exponential curve.

4.3.3 Stripe phase: Contrast

The time evolution of the stripe amplitude C gives information on the modulation depth and is shown in Fig. 4.14 The initial growth is consistent with the exponential behaviour predicted by theory and observed in previous experiments [26]. When an approximately ~ 0.4 maximum value is reached the curve remains constant for about 45 ms before it begins to decrease. As C takes ~ 7 ms to reach 0.4 but then it lasts for about 35 ms, the stripe phase is said to be relatively long lived. Longer times are characterized by still a non-zero contrast. Noting that the rapid decay of $N(t)$ in Fig. 4.13 is limited to the first 30-35 ms, we suggest that the high-density modulation does not persist at longer times. Observed long-time non zero C is then given by a less dense modulation, which has, perhaps, a different nature from stripe phase. From the

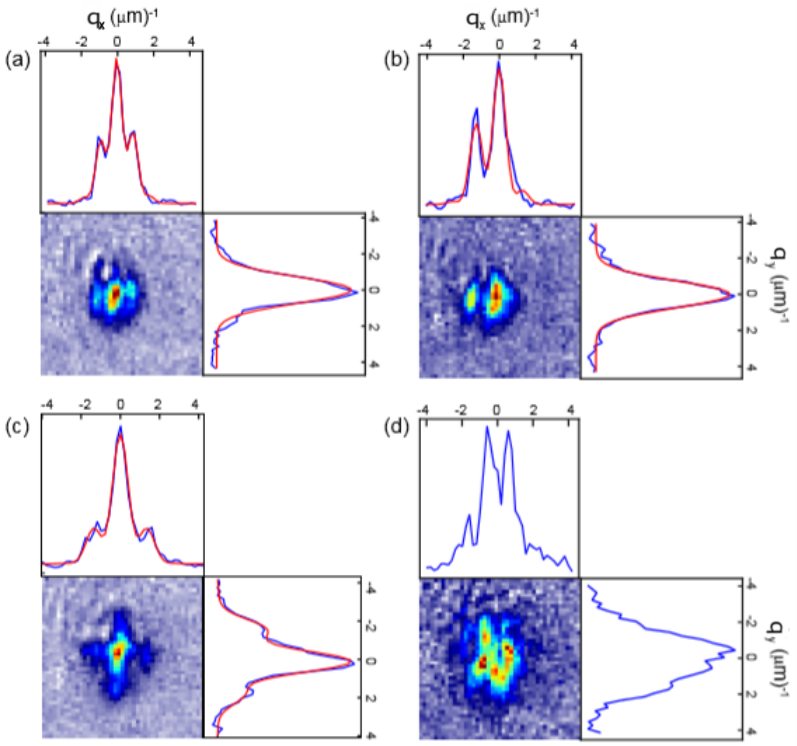

Figure 4.15: Examples of raw images and corresponding integrated profiles along x and y (blue lines). The red lines are fits to the integrated profiles with Eq. 4.9. The images correspond to the following parameters: **a** $B = 5.279$ G, $t = 18$ ms; **b** $B = 5.279$ G, $t = 43$ ms; **c** $B = 5.272$ G, $t = 5$ ms; **d** $B = 5.272$ G, $t = 18$ ms.

stability graph in Fig. 4.12 hypothesis of a possible return to a mean-field stable regime induced by the change in atom number has been already mentioned. A persistent modulation might be then attributed to a rotonic excitation on top of the condensate.

4.3.4 Stripe phase. Momentum and Phase

From the double slit analysis we get the following parameters: the characteristic periodicity $\bar{k}_\mathrm{i}$, the phase ϕ, the gaussian size σ, and unmodulated and modulated amplitudes A and A_1. Examples of integrated profiles fitted with Eq. 4.9, both in droplet and stripe regimes are shown in Fig. 4.15, while examples of the single data set parameters are shown in Fig. 4.16.

Results of momentum and phase of the stripe phase are now discussed. In Fig. 4.17 the time evolution of the stripe momentum $\bar{q_\mathrm{x}}$ is shown. Interestingly it remains constant close to 1.2 μm^{-1} for almost 45 ms, while it decreases to about 1 μm^{-1} in the time interval between 40 and 70 ms. The stripe phase is thus characterized by a momentum close to 1.2 μm^{-1} while the reduction of $\bar{q_\mathrm{x}}$ might indicate the presence of an excited roton mode in the BEC region [26].

The expression of the predicted momentum for the stripe phase has been derived in Sec. 1.4.2. The result is actually obtained in a mean field theory as it predicts the roton momentum. We employ the same formula because we interpret the stripe phase as a 'roton instability' stabilized by BMF effects. The formula presented were valid for an infinite pancake-like trap as an integration was performed in the (x, y) plane and a Thomas-Fermi expression was considered only for the z wave function. Considering the geometry of our trap we employ the expression of q_rot for a cigar-shape trap presented in Ref. [26]. The main difference from the previous derivation is that

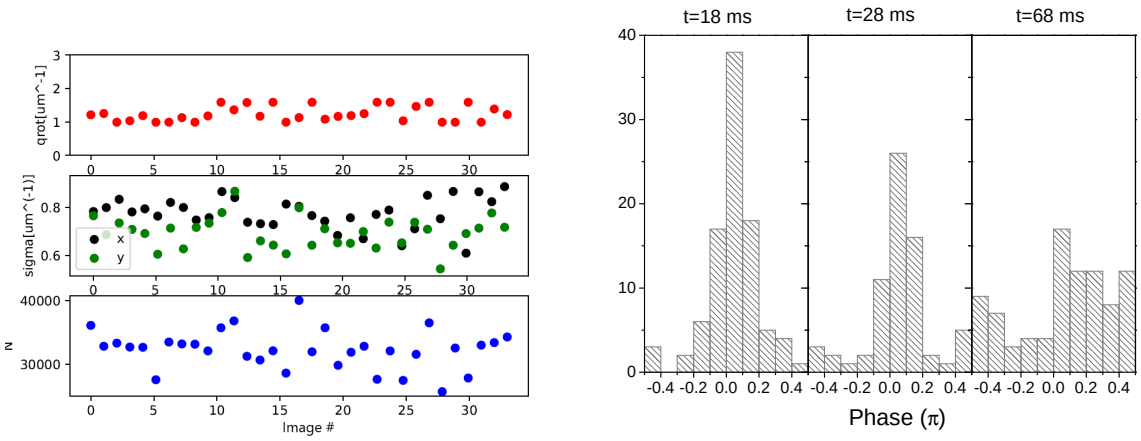

(a) $q_{\rm rot}, \sigma_x, N$ for each acquisition.

(b) phase histograms

Figure 4.16: Extracted parameters are shown for each data of a recorded data set, i.e. fixed magnetic field and evolution time. Data of the example are relative to $B = 5.279$ G and $t = 6$ ms. Only stripe phase data are drawn, the ones recognized as gaussian are here discarded. **a**. In abscissa the label of the single image is plotted. On the y axis $q_{\rm rot}, \sigma_x, N$ are plotted. **b**. Phase diagrams are reported for different time evolution at $B = 5.279$ G. First a non-random distribution is peaked around $\phi = 0$. The system evolves till the global phase is lost and the distribution becomes random.

a Thomas-Fermi density is considered not only in the z direction, but in both the tight trapped directions z and y[1]. By linearising the NLGPE, in Eq. 1.70, without taking into account any beyond mean field effects, it is found a general expression for the energy in the vicinity of the roton minimum for $\epsilon_{\rm dd} \sim 1$

$$\epsilon(q_{\rm x})^2 = \Delta^2 + \frac{2\hbar^2 q_{\rm rot}^2}{m}\frac{\hbar^2(q_{\rm x} - q_{\rm rot})^2}{2m} \tag{4.14}$$

with $\Delta = \sqrt{E_0^2 - E_{\rm I}^2}$ is the roton gap defined as the difference of the energy

$$E_0^2 = \frac{4\pi\hbar^2}{m} a_{\rm dd} \frac{\hbar^2}{2m} n_0 \left(\frac{1}{R_{\rm z}^2} + \frac{1}{R_{\rm y}^2}\right) \tag{4.15}$$

$$E_{\rm I} = \frac{8\pi\hbar^2(a_{\rm dd} - a_{\rm s})}{3m} n_0 \tag{4.16}$$

where $R_{\rm z}$ and $R_{\rm y}$ are the Thomas-Fermi radii of the condensate and n_0 its peak density. The energy $E_{\rm I}$ is related to the kinetic cost of creating the roton density modulation

$$\frac{\hbar^2 q_{\rm rot}^2}{2m} = E_{\rm I} \tag{4.17}$$

Eq. 4.16 can thus be read as a balance equation between the kinetic energy cost of the roton modulation and the interaction energy gain thanks to the dipole arrangement in a head-to-tail configuration. From such equation the theoretical value of $q_{\rm rot}$ can be calculated. To find the critical $a_{\rm s}$, we calculated the radii using a variational method [33], including beyond mean field terms. The resulting radii assuming a T-F density are $R_{\rm x} = 14$ μm, $R_{\rm y} = 3.3$ μm and

[1]Note that the x axis of our system corresponds to the y axis in the quoted article. In the following the axes shall be referred to in our notation: x axis → horizontal axis where the instability appears; y axis → vertical axis in the sense that the droplets arrange in the (x, y) plane; z → polarization axis.

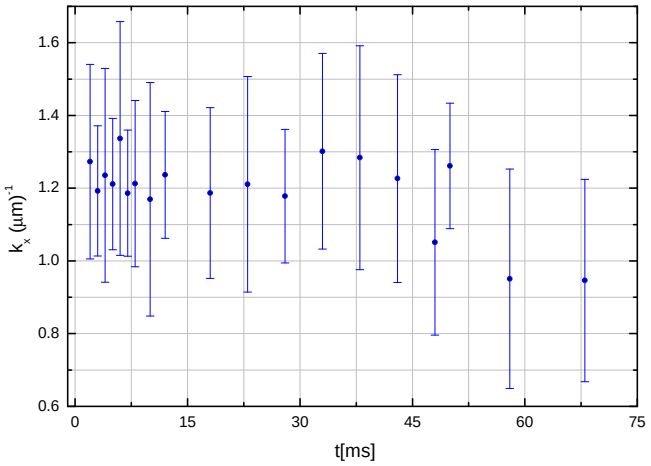

Figure 4.17: Time evolution of the stripe/roton momentum at $B = 5.279$G. The error bars represent the standard deviation of about 40 measurements. The roton momentum stays quite constant till 45 ms and then decreases.

$R_z = 4.6$ μm. For the nominal atom number, $N = 4\times10^4$, we find that the roton instability occurs at a scattering length $a_s = 107a_0$. At the instability, the roton momentum is $q_{rot} = 1.54$ μm^{-1}.

We compare our result of q_{rot} with theory. The observed roton momentum $\bar{q_x} = 1.2(2)$ μm^{-1} is distant by more than one standard deviation from the calculated value. In the theory, q_{rot} changes only mildly when changing N. For example, $q_{rot} = 1.65$ μm^{-1} for $N = 2.5 \times 10^4$ and $q_{rot} = 1.50$ μm^{-1} for $N = 5.5 \times 10^4$. Furthermore, the change of q_{rot} for variable trap frequencies in the range of the experimental uncertainties is in the interval $1.46 - 1.56$ μm^{-1}. This suggests that we can not attribute the observed deviation entirely to the experimental uncertainties, but perhaps also to the non perfect applicability of the theory to our case of non-negligible confinement along x.

The value of $\bar{q_x}$ gives also information on the characteristic distance d between two high density peaks $d = 2\pi/\bar{q_x} = 5.2(9)$ μm. The calculated BEC diameter along x is about 28 μm. Since the modulation tends to be confined in the centre of the harmonic trap [29], we expect between 2 and 4 stripes in our system. Our current resolution prevents us from estimating if more than two stripes are present and this is a retrospective justification of the double slit model development. The resolution in momentum space is 0.2 μm^{-1} (1/e Gaussian width) determined as width of the narrower spike in the droplet pattern. The example of a narrow spike is in Fig. 4.18. When an object of s dimension is too small to be resolved it induces a diffraction pattern on the camera. Since between the narrow spike and the rest of the interference pattern there's a zero order of the pattern, we speculate that is it due to the resolution limit. The width of the spike is then related to the resolution.

We now discuss the coherence properties of stripes and droplets. The coherence properties of the stripe regime are investigated by measuring the phase ϕ of the y integrated interference pattern $\tilde{n}(q_x)$. Fig. 4.16(b) shows three examples of the phase distribution, measured at different evolution times at $B = 5.279$ G. Fig. 4.19 shows the time evolution of the phase variance $\Delta\phi^2$ in the stripe regime, obtained from about 40 repetitions for each evolution time. Unlike previous observations [30], phase coherence is established during the stripe formation: $\Delta\phi^2$ decreases for $t < 10$ ms and stays approximately constant for about 20 ms, before increasing again at longer times, eventually reaching the expectation value for a uniformly distributed phase. Remarkably, we observe a coherence time significantly longer than the formation time of stripes. Currently,

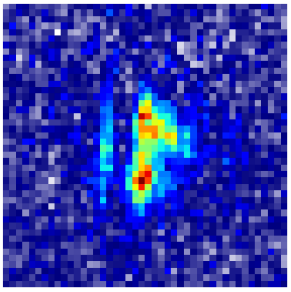

Figure 4.18: Droplet sample $B = 5.272$ G. On the left is clearly visible a narrow spike separated from the rest of the interference pattern by a zero order of the light. Its gaussian width is related to the resolution limit and is around 0.2 μm^{-1}.

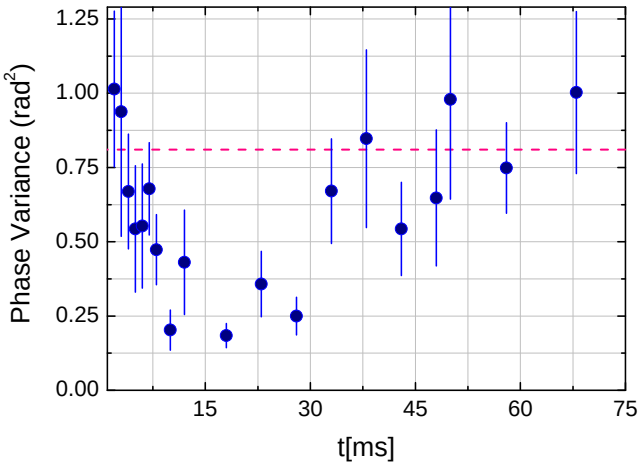

Figure 4.19: Time evolution of the phase variance $\Delta\phi^2$ in the stripe regime ($B = 5.279$ G). The error bars correspond to $\frac{2\Delta\phi^2}{2N-2}$, with $\simeq 40$ the number of measurements for each dataset. The red-dashed line is the expected variance for a uniformly distributed phase.

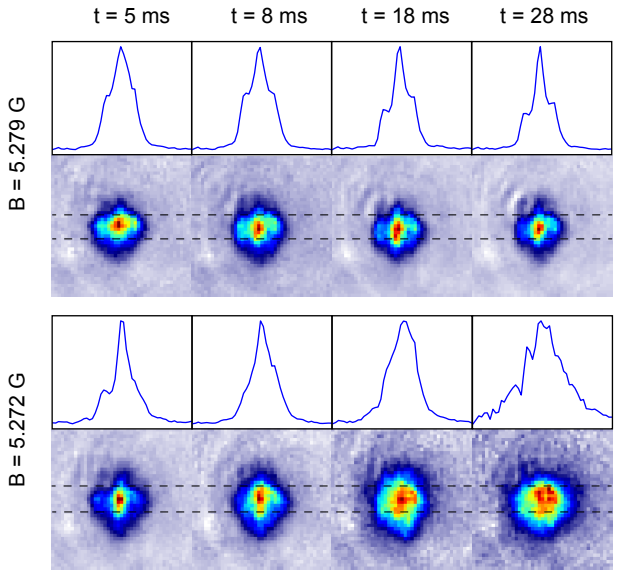

Figure 4.20: Averaged momentum distribution $\tilde{n}(q_x, q_y)$ over 40 absorption images in the stripe regime (top) and in the droplet regime (bottom) at different evolution times. The profiles are obtained by integrating $\tilde{n}(q_x, q_y)$ along q_y in the region between dashed lines.

we cannot distinguish if the observed dephasing is due to quantum or thermal fluctuations, or to technical noise. Stripes are clearly more coherent than droplets. Since droplets arrange in two-dimensional fluctuating patterns, it is difficult to extract quantitative information on their phase relation. In order to compare the coherence properties of stripes and droplets, we study their average momentum distribution over about 40 absorption images at different evolution times (see Fig. 4.20). In the stripe phase, we observe side peaks along x at q_x up to ~ 30 ms, indicating that the system is preserving its original phase, $\phi \sim 0$. Instead, in the droplet regime, phase coherence is already lost after 10 ms, in agreement with previous studies [30]: while at short time ($t = 5$ ms) the averaged distribution shows a structure in momentum space, at $t = 18$ ms no clear pattern is recognizable. These observations strongly suggest the presence of a mechanism preserving phase coherence in the stripe phase, which is absent in the droplet regime.

4.3.5 Thermalization measurement

The fluctuating interference pattern in the droplet regime does not allow us to determine their typical distance. A thermalization measure is then proposed to estimate such a quantity. In previous sections the recover of a BEC with a thermal component at long times in both droplet and stripe regime has been mentioned. We relate the thermal component to the kinetic energy of the high density component of the system present at shorter times. Let's call d the initial relative distance between the droplets (or the density peaks in the stripe). They rapidly lose coherence (or in the case of stripe after ~ 45 ms), acquiring a relative kinetic energy $\hbar^2/2md^2$. Such energy is strictly related to the temperature of the thermal component $T \sim k_B^{-1} \frac{\hbar^2}{2md^2}$.

A measurement of the thermal component of the condensate gives then information on the relative distance between droplet/high density peaks. Another important aspect is that for very long time the thermal component thermalizes with the BEC and disappears so the evolution time has to be not too long. In order to verify this last trend a qualitative temperature vs time measurement has been done with a trap depth of 60 nK, see Fig. 4.21. The measurement is done in the droplet regime ($B = 5.272$ G) as a hotter thermal component is expected with respect to

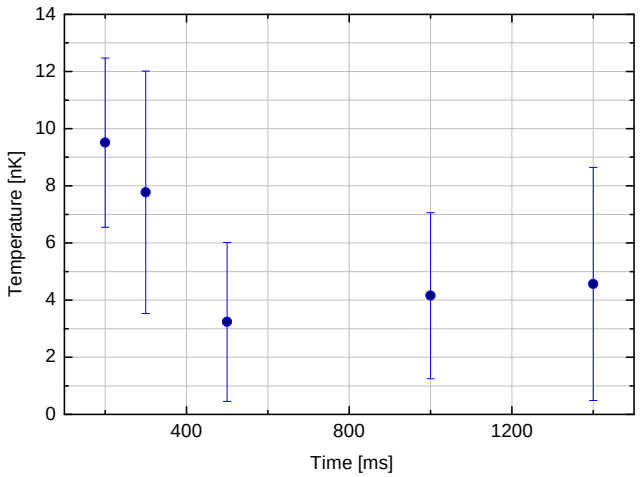

Figure 4.21: Time evolution of the temperature of the thermal component of the system. A minimum holding time of 200 ms in chosen in order to be sure that a BEC has been recovered.

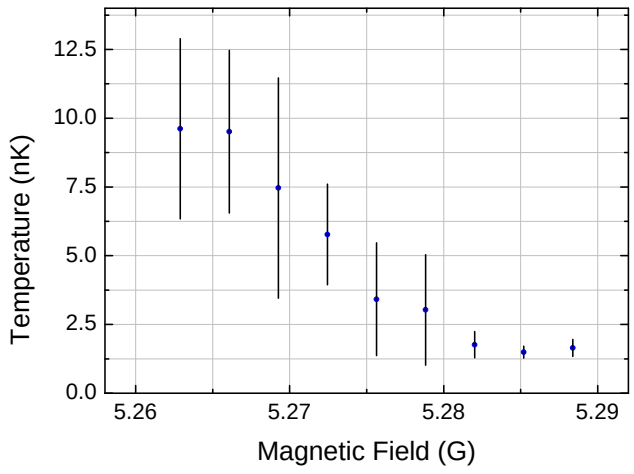

Figure 4.22: Temperature of the system after 200 ms evolution time at fixed magnetic field, as a function of the magnetic field.

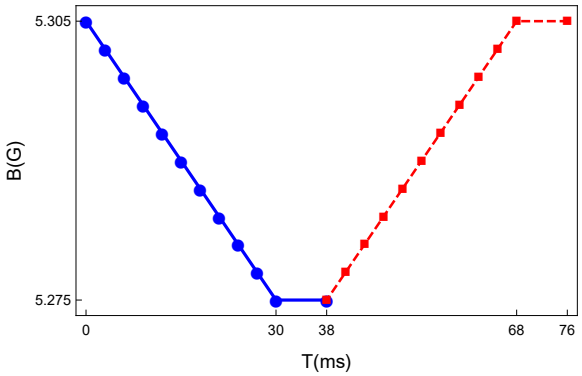

Figure 4.23: Ramp back and forth. A linear ramp (blue solid line) brings the system into the instability region in 30 ms. A measurement of the contrast is taken every 3 mG after an evolution time of 8 ms. 'Back measurements' are done with the first ramp, leaving the system at $B = 5.275$ G for 8 ms and then coming back with a linear ramp analogous to the first one (red dashed line).

the stripe regime. In order to be sure that a BEC has been recovered, we waited an evolution time of at least 200 ms. Data show that as the time passes the thermal component decreases. An evolution time of 200 ms is then chosen.

The thermal component of the sample is obtained by a two gaussian fit, as in Sec. 2.4. Temperature of such a component is estimated using Eq. 2.49. The results are reported in Fig. 4.22. In the BEC regime ($B > 5.28$ G) no detectable thermal component is found. In the stripe regime (5.275 G $< B < 5.28$ G) two different components are instead detected. A 3 nK temperature has been associated with the thermal component. It corresponds to a relative distance between high density peaks of the stripe regime $d \sim 4.5\mu$m. Such a distance is consistent with the one previously derived at short times $d = 5.2(9)$ μm in Sec. 4.3.4. In the droplet regime ($B < 5.275$ G) two components are again discerned. The thermal component temperature is estimated around 9 nK implying a mean distance between droplets of $d \sim 2.5$ μm. Such a distance is consistent with a previous experiment [29]. Droplets are then arranged closer to each other respect to the typical distance that high density stripe peaks have. This is quite intuitive as with the scattering length value has been lowered, increasing the attractive dipole term.

4.4 Back and forth: observation of an hysteresis.

Theory predicts that the phase transition from an homogeneous BEC to a roton-induced supersolid should be of first order, due to the breaking of the continuous translational symmetry [84,85]. First order transitions are characterized by an hysteresis feature. In order to verify if the BEC-stripe transition is a first order one, the reversibility of such transition is therefore studied. A back and forth ramp into the instability regime has been constructed. In analogy with the previous ramp a linear ramp of the duration of 30 ms is employed. The first round brings the system from $B = 5.305$ G (BEC) to $B = 5.275$ G(stripe phase). The ramp is divided into 10 step. For each magnetic field value, an observation of the correspondent phase is done after an evolution time of 8 ms. This waiting time has been chosen because it is of the order of the stripe formation. Second round consists in bringing the system to $B = 5.29$ G and waiting 8 ms for the stripe phase to form. The system is then ramping back to the stable region with the same procedure described above. A schematic representation of the ramp is shown in Fig. 4.23. Each observation is characterized by a contrast value. The evolution of the contrast as a function of the magnetic field is shown in Fig. 4.24. The evidence of a non zero contrast, at the end of the second ramp, is found indicating the persistence of a roton-like modulation in the system. The example of an

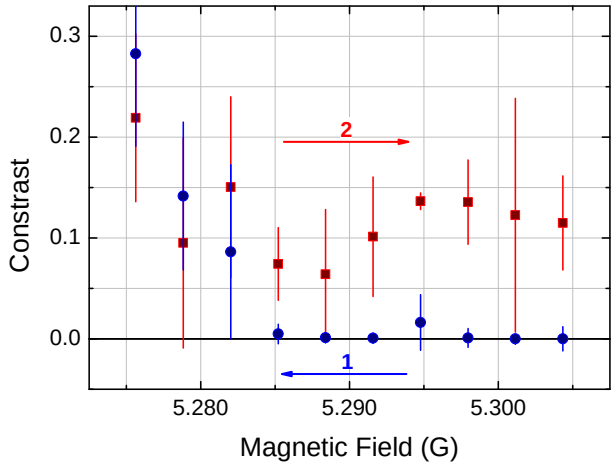

Figure 4.24: Bec-stripe transition hysteresis. Constrast as a function of the magnetic field is represented. First the system is brought into the instability (blue circles, direction of the blue arrow). Second the field is increased back taking the system into the stable regime again (red squares, red arrow direction). Each measurement is taken after an evolution time of 8 ms. The error bars represent the standard deviation of about 10 measurements.

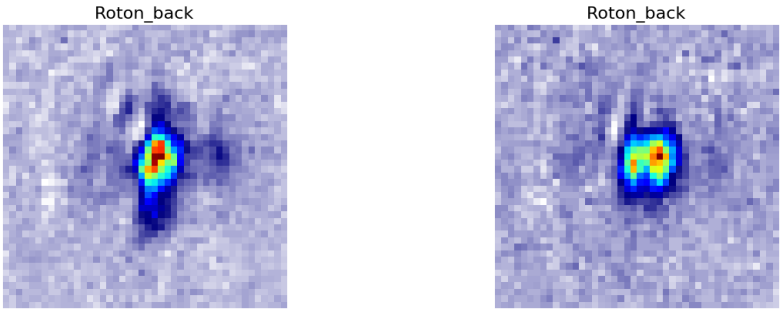

(a) $B_f = 5.285$ G (b) $B_f = 5.295$ G

Figure 4.25: Space momentum distribution of the system after it has been brought to the stripe regime ($B = 5.275$ G), held for 8 ms at this field, and ramped back to the stable regime. Images represent the phase of the system for different final fields B_f after a further holding time of 8 ms at fixed magnetic field B_f.

observation is also reported, Fig. 4.25.

This study reveals therefore hysteresis across the roton instability. So far, we have no information on whether stripes are the ground state or a metastable state of the system. Therefore we cannot associate our observation to a BEC to supersolid phase transition.

Conclusions

In this thesis I have presented the experimental study of the weakly attractive regime of a dipolar Dy Bose-Einstein condensate, emphasising, in particular, the onset of a new quantum regime appearing in a specific range of scattering length. We first characterized the main parameters of the system, such as Feshbach resonances and three-body recombination rate. We then choose the trap frequencies in order to confine the system in an anisotropic configuration. Taking advantage of the wide range of Feshbach resonances of Dy, we tuned the inter-particle contact interaction. This allowed us to see what happens when the system feels the third dimension, i.e. dipoles can arranged in a head-to-tail configuration. We see the insurgence of a peculiar structure in momentum space with a central peak and two side peaks, signalling the formation of a periodic modulation of the density in real space that we called 'stripe phase'. We studied its dependence on the atom number using a phenomenological parameter. A double slit model is instead used to analyse its characteristics, such as the momentum and the phase. The characteristic density of the system is also deduced by the decay rate of the atom number via three-body recombination. We also varied the inter-particle contact interaction in a different regime. The modulated phase regime is first encountered, but we then observed that further lowering of the scattering length leads to the formation of self-bound quantum droplets. In the end we performed a measure back and forth in the unstable regime in order to study the transition to such a stripe phase. We observed a hysteresis, suggesting that a first order phase transition from the BEC to a stripe phase might be present. But how do we interpret our observation?

By lowering the inter-particle contact interaction, we bring the system into a new finite-momentum minimum. According to the theory, this minimum is called roton and in a stable BEC is an excited state. Therefore it is not spontaneously populated, but needs an extra energy to be given to the sytem. Lowering the scattering length corresponds to lowering the additional energy required to populate the mode. Theoretically then when such an energy goes to zero the mode should spontaneously populate and the system should undergo a rotonic instability. This is exactly what we observe. We found that such a rotonic instability corresponds to a stable stripe phase. This result is quite amazing, since such a quantum phase has never seen before and is characterized by very interesting features. We found it is relatively long lived and characterized by a finite momentum, close to the one of the stable roton mode. Furthermore we observed a quite long coherence time, long with respect to the formation time of the stripe phase. This last property is of particular interest, since no coherent phase was observed so far in a dipolar BEC unstable regime. Previous studies on such instabilities have brought to the observation of another fascinating, but incoherent, phase: quantum droplets. We demonstrate that the stripe phase is different from quantum droplet, as they correspond to different values of the scattering length, i.e. to a different relative strength of the contact and dipolar interactions. However, we found that they share the same stabilization mechanism: quantum fluctuations. Quantum fluctuations in dipolar systems can be modelled as a short repulsive contact interaction. Both droplets and stripes exist in a weakly attractive regime. A weak repulsive force can thus prevent the system to collapse. We found that quantum fluctuations plays exactly this role.

I have contributed to various aspects of the reported work, with a special focus on the analysis of the experimental data on the stripe phase. In particular, I've written the code to extract all the reported informations from the momentum distribution, such as atom numbers, characteristic

momenta, phase coherence, interference contrast. I have then contributed to the analysis of the retrieved data in terms of the theoretical models presented in the thesis. I participated to interesting discussions around the possible interpretations of the data and finally, I've contributed to write the paper in which we have recently reported the observations [32].

Although we have already emphasized some key aspects, we're just at the beginning of the study of this very interesting stripe phase. First of all we're thinking on how to reduce atom number fluctuations, which are currently limiting a more stringent comparison of experiment and theory. Moreover the use of broad Feshbach resonances [78] would allow further study introducing the possibility of a finer tuning and more precise control of the scattering length. Finally, our study was limited by the current resolution of the imaging system, to observation in the momentum space, i.e. after atoms are released from the trap and expand ballistically for several tens milliseconds. An high resolution imaging system, which I have contributed to test, will be soon implemented in our experiment, in order to allow also observations in the coordinate space, i.e. in situ.

The stripe phase existence is completely due to the competition between an attractive and a repulsive force. In dipolar BEC such forces are naturally given by the inter-particle interactions (contact and dipolar), thus particularly interesting because no external elements are necessary. The discovery of a self-ordered phase with quite long coherence time in a dipolar BEC, is an important step toward a dipolar supersolid.

Bibliography

[1] Heike Kamerlingh Onnes. Investigations into the properties of substances at low temperatures, which have led, amongst other things, to the preparation of liquid helium. *Nobel lecture*, 4, 1913.

[2] Dirk Van Delft and Peter Kes. The discovery of superconductivity. *Physics Today*, 63(9):38–43, 2010.

[3] Claudia Eberlein, Stefano Giovanazzi, and Duncan HJ O'Dell. Exact solution of the thomas-fermi equation for a trapped Bose-Einstein condensate with dipole-dipole interactions. *Physical Review A*, 71(3):033618, 2005.

[4] Christopher J Pethick and Henrik Smith. *Bose-Einstein condensation in dilute gases*. Cambridge university press, 2002.

[5] Mike H Anderson, Jason R Ensher, Michael R Matthews, Carl E Wieman, and Eric A Cornell. Observation of Bose-Einstein condensation in a dilute atomic vapor. *Science*, 269(5221):198–201, 1995.

[6] Kendall B Davis, M-O Mewes, Michael R Andrews, NJ Van Druten, DS Durfee, DM Kurn, and Wolfgang Ketterle. Bose-Einstein condensation in a gas of sodium atoms. *Physical Review Letters*, 75(22):3969, 1995.

[7] Lev Pitaevskii and Sandro Stringari. *Bose-Einstein condensation and superfluidity*, volume 164. Oxford University Press, 2016.

[8] Cheng Chin, Rudolf Grimm, Paul Julienne, and Eite Tiesinga. Feshbach resonances in ultracold gases. *Reviews of Modern Physics*, 82(2):1225, 2010.

[9] Pyotr Kapitza. Viscosity of liquid helium below the λ-point. *Nature*, 141(3558):74, 1938.

[10] Michael Robin Matthews, Brian P Anderson, PC Haljan, DS Hall, CE Wieman, and Eric A Cornell. Vortices in a Bose-Einstein condensate. *Physical Review Letters*, 83(13):2498, 1999.

[11] Markus Greiner, Olaf Mandel, Tilman Esslinger, Theodor W Hänsch, and Immanuel Bloch. Quantum phase transition from a superfluid to a mott insulator in a gas of ultracold atoms. *nature*, 415(6867):39, 2002.

[12] Jun-Ru Li, Jeongwon Lee, Wujie Huang, Sean Burchesky, Boris Shteynas, Furkan Çağrı Top, Alan O Jamison, and Wolfgang Ketterle. A stripe phase with supersolid properties in spin–orbit-coupled Bose-Einstein-einstein condensates. *Nature*, 543(7643):91, 2017.

[13] Curtis Charles Bradley, CA Sackett, and RG Hulet. Bose-Einstein condensation of lithium: Observation of limited condensate number. *Physical Review Letters*, 78(6):985, 1997.

[14] Giovanni Modugno, Gabriele Ferrari, Giacomo Roati, Robert J Brecha, A Simoni, and Massimo Inguscio. Bose-Einstein condensation of potassium atoms by sympathetic cooling. *Science*, 294(5545):1320–1322, 2001.

[15] Dale G Fried, Thomas C Killian, Lorenz Willmann, David Landhuis, Stephen C Moss, Daniel Kleppner, and Thomas J Greytak. Bose-Einstein condensation of atomic hydrogen. *Physical Review Letters*, 81(18):3811, 1998.

[16] Axel Griesmaier, Jörg Werner, Sven Hensler, Jürgen Stuhler, and Tilman Pfau. Bose-Einstein condensation of chromium. *Physical Review Letters*, 94(16):160401, 2005.

[17] Yosuke Takasu, Kenichi Maki, Kaduki Komori, Tetsushi Takano, Kazuhito Honda, Mitsutaka Kumakura, Tsutomu Yabuzaki, and Yoshiro Takahashi. Spin-singlet Bose-Einstein condensation of two-electron atoms. *Physical Review Letters*, 91(4):040404, 2003.

[18] LF Livi, G Cappellini, M Diem, L Franchi, C Clivati, M Frittelli, F Levi, D Calonico, J Catani, M Inguscio, et al. Synthetic dimensions and spin-orbit coupling with an optical clock transition. *Physical Review Letters*, 117(22):220401, 2016.

[19] Krzysztof Goral, Kazimierz Rzazewski, and Tilman Pfau. Bose-Einstein condensation with magnetic dipole-dipole forces. *Physical Review A*, 61(5):051601, 2000.

[20] G Bismut, B Laburthe-Tolra, E Maréchal, P Pedri, O Gorceix, and L Vernac. Anisotropic excitation spectrum of a dipolar quantum bose gas. *Physical Review Letters*, 109(15):155302, 2012.

[21] Thierry Lahaye, Jonas Metz, Bernd Froehlich, Tobias Koch, Maximilian Meister, Axel Griesmaier, Tilman Pfau, Hiroki Saito, Yuki Kawaguchi, and Masahito Ueda. d-wave collapse and explosion of a dipolar Bose-Einstein condensate. *Physical Review Letters*, 101(8):080401, 2008.

[22] K Aikawa, A Frisch, M Mark, S Baier, A Rietzler, R Grimm, and F Ferlaino. Bose-Einstein condensation of erbium. *Physical Review Letters*, 108(21):210401, 2012.

[23] E Lucioni, G Masella, A Fregosi, C Gabbanini, S Gozzini, A Fioretti, L Del Bino, J Catani, G Modugno, and M Inguscio. A new setup for experiments with ultracold dysprosium atoms. *The European Physical Journal Special Topics*, 226(12):2775–2780, 2017.

[24] Axel Griesmaier, Jürgen Stuhler, Tobias Koch, Marco Fattori, Tilman Pfau, and Stefano Giovanazzi. Comparing contact and dipolar interactions in a Bose-Einstein condensate. *Physical Review Letters*, 97(25):250402, 2006.

[25] L Santos, GV Shlyapnikov, and M Lewenstein. Roton-maxon spectrum and stability of trapped dipolar Bose-Einstein condensates. *Physical Review Letters*, 90(25):250403, 2003.

[26] Lauriane Chomaz, RMW Bijnen, Daniel Petter, Giulia Faraoni, Simon Baier, J Hendrik Becher, Manfred J Mark, Falk Waechtler, Luis Santos, and Francesca Ferlaino. Observation of roton mode population in a dipolar quantum gas. *Nature Physics*, 14(5):442, 2018.

[27] Aristeu RP Lima and Axel Pelster. Beyond mean-field low-lying excitations of dipolar bose gases. *Physical Review A*, 86(6):063609, 2012.

[28] Igor Ferrier-Barbut, Holger Kadau, Matthias Schmitt, Matthias Wenzel, and Tilman Pfau. Observation of quantum droplets in a strongly dipolar bose gas. *Physical Review Letters*, 116(21):215301, 2016.

[29] Holger Kadau, Matthias Schmitt, Matthias Wenzel, Clarissa Wink, Thomas Maier, Igor Ferrier-Barbut, and Tilman Pfau. Observing the rosensweig instability of a quantum ferrofluid. *Nature*, 530(7589):194, 2016.

[30] Matthias Wenzel, Fabian Böttcher, Tim Langen, Igor Ferrier-Barbut, and Tilman Pfau. Striped states in a many-body system of tilted dipoles. *Physical Review A*, 96(5):053630, 2017.

[31] Massimo Boninsegni and Nikolay V Prokof'ev. Colloquium: Supersolids: What and where are they? *Reviews of Modern Physics*, 84(2):759, 2012.

[32] Luca Tanzi, Eleonora Lucioni, Francesca Famà, Jacopo Catani, Andrea Fioretti, Carlo Gabbanini, and Giovanni Modugno. Observation of stable stripes in a dipolar quantum gas. *arXiv preprint arXiv:1811.02613*, 2018.

[33] S Giovanazzi, P Pedri, LMNBF Santos, A Griesmaier, M Fattori, T Koch, J Stuhler, and T Pfau. Expansion dynamics of a dipolar Bose-Einstein condensate. *Physical Review A*, 74(1):013621, 2006.

[34] Edward Charles Titchmarsh Titchmarsh, Edward Charles Titchmarsh, DR Heath-Brown, et al. *The theory of the Riemann zeta-function*. Oxford University Press, 1986.

[35] Enore Guadagnini. Lezioni di fisica statistica.

[36] LD Landau and EM Lifshitz. Quantum mechanics, vol. 3. *Course of theoretical physics*.

[37] Matteo Zaccanti, Benjamin Deissler, Chiara D'Errico, Marco Fattori, Mattia Jona-Lasinio, Stefan Müller, Giacomo Roati, Massimo Inguscio, and Giovanni Modugno. Observation of an efimov spectrum in an atomic system. *Nature Physics*, 5(8):586, 2009.

[38] EA Burt, RW Ghrist, CJ Myatt, MJ Holland, Eric A Cornell, and CE Wieman. Coherence, correlations, and collisions: What one learns about Bose-Einstein condensates from their decay. *Physical Review Letters*, 79(3):337, 1997.

[39] Tino Weber, Jens Herbig, Michael Mark, Hanns-Christoph Nägerl, and Rudolf Grimm. Three-body recombination at large scattering lengths in an ultracold atomic gas. *Physical Review Letters*, 91(12):123201, 2003.

[40] Michael Mehring. Nuclear spin interactions in solids. In *Principles of High Resolution NMR in Solids*, pages 8–62. Springer, 1983.

[41] Thierry Lahaye, C Menotti, L Santos, M Lewenstein, and T Pfau. The physics of dipolar bosonic quantum gases. *Reports on Progress in Physics*, 72(12):126401, 2009.

[42] S Yi and L You. Trapped condensates of atoms with dipole interactions. *Physical Review A*, 63(5):053607, 2001.

[43] Evgenii Mikhailovich Lev D. Landau, Evgenij M. Lifshitz and Lev Petrovich Pitaevskii. *Statistical physics: theory of the condensed state*, volume 9. Elsevier, 2013.

[44] DHJ O'dell, S Giovanazzi, and G Kurizki. Rotons in gaseous Bose-Einstein condensates irradiated by a laser. *Physical Review Letters*, 90(11):110402, 2003.

[45] Mikhail A Baranov, Marcello Dalmonte, Guido Pupillo, and Peter Zoller. Condensed matter theory of dipolar quantum gases. *Chemical Reviews*, 112(9):5012–5061, 2012.

[46] Holger Kadau. *Rosensweig Instability and Droplets in a Quantum Ferrofluid of Dysprosium Atoms*. PhD thesis, Verlag Dr. Hut, 2016.

[47] Tsin D Lee, Kerson Huang, and Chen N Yang. Eigenvalues and eigenfunctions of a bose system of hard spheres and its low-temperature properties. *Physical Review*, 106(6):1135, 1957.

[48] Igor Ferrier-Barbut, Matthias Schmitt, Matthias Wenzel, Holger Kadau, and Tilman Pfau. Liquid quantum droplets of ultracold magnetic atoms. *Journal of Physics B: Atomic, Molecular and Optical Physics*, 49(21):214004, 2016.

[49] Matthias Schmitt. *A Self-bound Dilute Quantum Liquid of Dysprosium Atoms*. PhD thesis, Verlag Dr. Hut, 2017.

[50] Kui-Tian Xi and Hiroki Saito. Droplet formation in a Bose-Einstein condensate with strong dipole-dipole interaction. *Physical Review A*, 93(1):011604, 2016.

[51] Julian Léonard, Andrea Morales, Philip Zupancic, Tilman Esslinger, and Tobias Donner. Supersolid formation in a quantum gas breaking a continuous translational symmetry. *Nature*, 543(7643):87, 2017.

[52] MD Cowley and Ronald E Rosensweig. The interfacial stability of a ferromagnetic fluid. *Journal of Fluid Mechanics*, 30(4):671–688, 1967.

[53] Stefan Bohlius. *The Rosensweig instability in isotropic magnetic gels*. PhD thesis, 2008.

[54] Jaakko VI Timonen, Mika Latikka, Ludwik Leibler, Robin HA Ras, and Olli Ikkala. Switchable static and dynamic self-assembly of magnetic droplets on superhydrophobic surfaces. *Science*, 341(6143):253–257, 2013.

[55] Thomas Maier. *Interactions in a Quantum Gas of Dysprosium Atoms*. PhD thesis, Verlag Dr. Hut, 2015.

[56] John R de Laeter, John Karl Böhlke, P De Bièvre, H Hidaka, HS Peiser, KJR Rosman, and PDP Taylor. Atomic weights of the elements. review 2000 (iupac technical report). *Pure and applied chemistry*, 75(6):683–800, 2003.

[57] PÉ Lecoq de Boisbaudran. L'holmine (ou terre x de m. soret) contient au moins deux radicaux métallique. *Compt Rendus*, 102:1003–1004, 1886.

[58] Frank H Spedding, Earl J Wheelwright, and Jack E Powell. Method of separating rare earths, July 9 1957. US Patent 2,798,789.

[59] Mingwu Lu, Nathaniel Q Burdick, and Benjamin L Lev. Quantum degenerate dipolar fermi gas. *Physical Review Letters*, 108(21):215301, 2012.

[60] William Clyde Martin, Romuald Zalubas, and Lucy Hagan. Atomic energy levels-the rare-earth elements. the spectra of lanthanum, cerium, praseodymium, neodymium, promethium, samarium, europium, gadolinium, terbium, dysprosium, holmium, erbium, thulium, ytterbium, and lutetium. Technical report, NATIONAL STANDARD REFERENCE DATA SYSTEM, 1978.

[61] P Grundevik, M Gustavsson, and Sune Svanberg. Isotope shifts in dysprosium measured by high resolution laser spectroscopy. *Physics Letters A*, 56(1):25–26, 1976.

[62] Leonardo del Bino. Development of an experimental apparatus for the realization of dipolar-quantum gases of dysprosium atoms. Master's thesis, Università di Firenze, 2015.

[63] Christopher J Foot et al. *Atomic physics*, volume 7. Oxford University Press, 2005.

[64] Nikolaj Leonidivič Manakov, Vitalij Dmitrievič Ovsiannikov, and Lev Pavlovič Rapoport. Atoms in a laser field. *Physics Reports*, 141(6):320–433, 1986.

[65] Hui Li, Jean-Francois Wyart, Olivier Dulieu, Sylvain Nascimbene, and Maxence Lepers. Optical trapping of ultracold dysprosium atoms: transition probabilities, dynamic dipole polarizabilities and van der waals c 6 coefficients. *Journal of Physics B: Atomic, Molecular and Optical Physics*, 50(1):014005, 2016.

[66] Fam Le Kien, Philipp Schneeweiss, and Arno Rauschenbeutel. Dynamical polarizability of atoms in arbitrary light fields: general theory and application to cesium. *The European Physical Journal D*, 67(5):92, 2013.

[67] C Ravensbergen, V Corre, E Soave, M Kreyer, S Tzanova, E Kirilov, and R Grimm. Accurate determination of the dynamical polarizability of dysprosium. *Physical Review Letters*, 120(22):223001, 2018.

[68] Thomas Chalopin, Vasiliy Makhalov, Chayma Bouazza, Alexandre Evrard, Adam Barker, Jean Dalibard, Raphael Lopes, and Sylvain Nascimbene. Anisotropic light-shift and magic-polarization of the intercombination line of dysprosium atoms in a far-detuned dipole trap. *arXiv preprint arXiv:1805.06878*, 2018.

[69] DJ McCarron, SA King, and SL Cornish. Modulation transfer spectroscopy in atomic rubidium. *Measurement Science and Technology*, 19(10):105601, 2008.

[70] Abraham J Olson, Robert J Niffenegger, and Yong P Chen. Optimizing the efficiency of evaporative cooling in optical dipole traps. *Physical Review A*, 87(5):053613, 2013.

[71] Wolfgang Ketterle, NJ Van Druten, et al. Evaporative cooling of trapped atoms. *Adv. At. Mol. Opt. Phys*, 37(0):181, 1996.

[72] Alessandro Fregosi. Intrappolamento ottico di atomi di disprosio per la realizzazione di un condensato di Bose-Einstein di atomi dipolari. Master's thesis, Università di Pisa, 2018.

[73] TW Hansch and B Couillaud. Laser frequency stabilization by polarization spectroscopy of a reflecting reference cavity. *Optics Communications*, 35(3):441–444, 1980.

[74] Eric D Black. An introduction to pound–drever–hall laser frequency stabilization. *American Journal of Physics*, 69(1):79–87, 2001.

[75] Davide Dreon, Leonid A Sidorenkov, Chayma Bouazza, Wilfried Maineult, Jean Dalibard, and Sylvain Nascimbene. Optical cooling and trapping of highly magnetic atoms: the benefits of a spontaneous spin polarization. *Journal of Physics B: Atomic, Molecular and Optical Physics*, 50(6):065005, 2017.

[76] DS Jin, JR Ensher, MR Matthews, CE Wieman, and Eric A Cornell. Quantitative studies of Bose-Einstein condensation in a dilute atomic vapor. *Czechoslovak Journal of Physics*, 46(6):3070–3076, 1996.

[77] Yijun Tang, Andrew G Sykes, Nathaniel Q Burdick, Jack M DiSciacca, Dmitry S Petrov, and Benjamin L Lev. Anisotropic expansion of a thermal dipolar bose gas. *Physical Review Letters*, 117(15):155301, 2016.

[78] E Lucioni, L Tanzi, A Fregosi, J Catani, S Gozzini, M Inguscio, A Fioretti, C Gabbanini, and G Modugno. Dysprosium dipolar Bose-Einstein condensate with broad feshbach resonances. *arXiv preprint arXiv:1803.10676*, 2018.

[79] Sanjukta Roy, Manuele Landini, Andreas Trenkwalder, Giulia Semeghini, Giacomo Spagnolli, Andrea Simoni, Marco Fattori, Massimo Inguscio, and Giovanni Modugno. Universality of the three-body efimov parameter at narrow feshbach resonances. *Physical Review Letters*, 111(5):053202, 2013.

[80] M Berninger, A Zenesini, B Huang, W Harm, H-C Nägerl, F Ferlaino, R Grimm, PS Julienne, and JM Hutson. Universality of the three-body parameter for efimov states in ultracold cesium. *Physical Review Letters*, 107(12):120401, 2011.

[81] R Bombin, J Boronat, and F Mazzanti. Dipolar bose supersolid stripes. *Physical Review Letters*, 119(25):250402, 2017.

[82] P Pedri, L Pitaevskii, S Stringari, C Fort, S Burger, FS Cataliotti, P Maddaloni, F Minardi, and M Inguscio. Expansion of a coherent array of Bose-Einstein condensates. *Physical Review Letters*, 87(22):220401, 2001.

[83] Giulia Faraoni. *Quantum systems of ultracold atoms with tunable interactions*. PhD thesis, Università degli studi Firenze, 2017.

[84] Zhen-Kai Lu, Yun Li, DS Petrov, and GV Shlyapnikov. Stable dilute supersolid of two-dimensional dipolar bosons. *Physical Review Letters*, 115(7):075303, 2015.

[85] Yun Li, Giovanni I Martone, Lev P Pitaevskii, and Sandro Stringari. Superstripes and the excitation spectrum of a spin-orbit-coupled Bose-Einstein condensate. *Physical Review Letters*, 110(23):235302, 2013.

Ringraziamenti

Tante sono le persone da ringraziare ed è difficile scegliere da dove cominciare. Seguirò quindi un ordine temporale. I miei più sinceri ringraziamenti vanno ai miei relatori. Al Dott. Andrea Fioretti, che qualche mese fa mi presentò l'affascinante esperimento su cui poi ho lavorato. Lo ringrazio del tempo che mi ha dedicato, delle correzioni e di tutte le spiegazioni. Al Prof. Giovanni Modugno, che con il suo entusiasmo per la fisica ha coinvolto anche me. Lo ringrazio per tutte le critiche ed i suggerimenti, per la pazienza e le delucidazioni. Al Prof. Francesco Fuso, il quale è sempre estremamente disponibile per una chiacchierata in laboratorio. Lo ringrazio per tutte le volte che mi ha spronato a scrivere, per la sua simpatia e per l'invito a fare sempre le cose in maniera precisa ed elaborata. Ringrazio le persone dell'istituto INO, per i pranzi in compagnia ed i coffee break delle 10. Dei ringraziamenti particolari vanno alle persone con cui ho lavorato, in particolare al Dott. Carlo Gabbanini e al Dott. Luca Tanzi, sempre disponibili per rispondere alle mie domande ed aiutarmi. Infine ringrazio Alessandro Fregosi per i suggerimenti stilistici e le chiacchierate.

L'area del CNR di Pisa è senza dubbio il luogo dove ho trascorso più tempo negli ultimi mesi, tuttavia un ringraziamento speciale va anche a chi mi ricorda che gli impegni importanti vanno anche smorzati con un pò di svago. Passo quindi a ringraziare i miei amici, fisici e non. Li ringrazio per tutti i pranzi al chioschino, le serate in giro e le risate. Batto il cinque con tutti quelli che hanno giocato con me a pallavolo e che tutt'ora continuano a farlo, che sia estate sulla spiaggia o d'inverno al chiuso. Ringrazio una persona speciale, che nelle giornate più stressanti mi ha anche portato la spesa, pur di non farmi staccare dalla tastiera.

Sono infine giunta al 'principio' dei miei ringraziamenti. Ringrazio la famiglia. Tutti gli zii ed i nonni, quelli presenti e quelli che ci sono stati. Mio padre, mia madre e naturalmente la mia sorellina. Vi ringrazio tantissimo per il supporto che mi date e vi abbraccio forte forte.